Development of Vertical Welding Technology for Heavy-Thick and Ni Steel Plate Using Hot-Wire Laser Welding Method

（ホットワイヤ・レーザ溶接法による厚鋼板およびニッケル鋼立向き溶接技術の開発）

November, 2019

Sittisak Charunetratsamee

Department of Mechanical Science and Engineering
Graduate School of Engineering
Hiroshima University

Table of Contents

iii

Chapter 1

Introduction

1.1 Research background

1.1.1 Background of the shipbuilding industry

In order to increase the efficiency of maritime transport, a container ship capacity has dramatically increased over the past decades to minimize the transportation cost. The transition of the maximum loading capacity of container ships is shown in Fig. 1.1. The container size is rising from around 800 TEU (Twenty-foot equivalent unit: a 20-foot-long (6.1m) container) in the 60S, and container ships up to 20000 TEU has been constructed [1-2].

Container ships that carry their entire load inside the hull have the hatch cover on the deck and a large opening in the upper deck as shown in Fig. 1.2, and while sailing on the sea, the ship is subjected to heavy rolling and pitching which cannot only disturb the cargo but also upset the stability of the ship. Therefore, it is necessary to ensure the longitudinal strength of the hull against a load of waves that bend the entire hull and the high strength deck structures including the hatch side coaming, strength deck, sheer strake, and longitudinal bulkhead are applied.

The heavy thickness of large container ships' structures is up to 100 mm and those are as high as a few meters on the ship side shell so it is very difficult to weld in the vertical position with multi-pass welds. For an increase in productivity, Electrogas Arc Welding (EGW), which is one-pass vertical welding, is an effective method for vertical welding process with a high deposit rate [3]. However, since EGW creates large heat input, the decrease in the toughness of coarse grain HAZ (CGHAZ) is a problem. On the other hand, the alloy design in a base metal and the TMCP process has been also optimized to obtain proper impact toughness in CGHAZ [4].

For instance, the occurrence and development of a brittle crack in a welded joint due to lack of fracture toughness might lead to the huge scale accident, and YP40 steel has been used for the hatch side coaming in particular. The hatch side coaming requires not only the fatigue resistance due to the pitching load but also the arrest performance to stop propagating the brittle crack. Moreover, as the hatch side coaming is located at the uppermost part of the hull cross section, it is an important member also in terms of strength and regarding a recent increase in the size of container ships, the thickness has risen so the further large heat input welding for thicker joints has been concerned. Therefore, YP47 steel was newly developed. It achieved more both strength and toughness which greatly provided to reduce the heavy thickness of components [5-9].

As described above, a novel vertical welding process is strongly demanded to achieve the higher efficiency and low heat input for obtaining welded joints with higher strength and higher toughness.
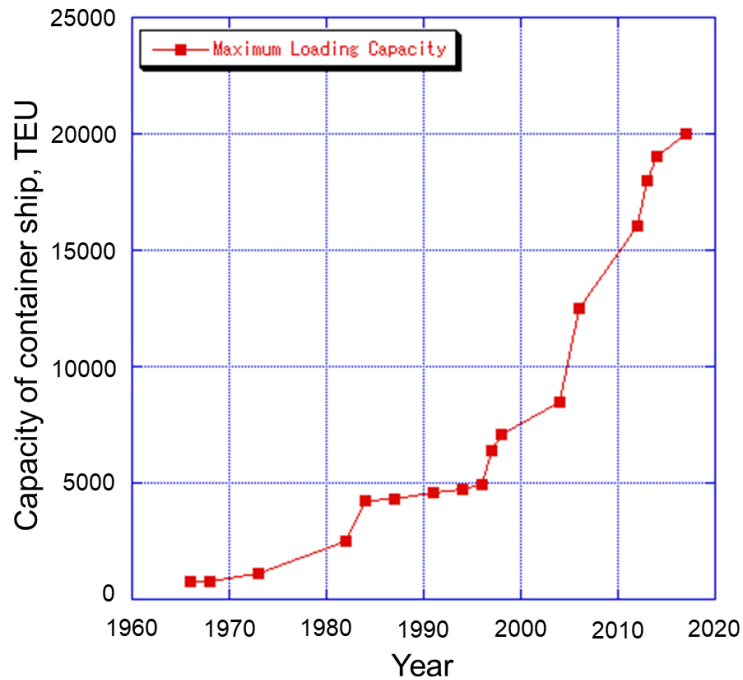
Fig. 1.1 Transition of maximum loading capacity.
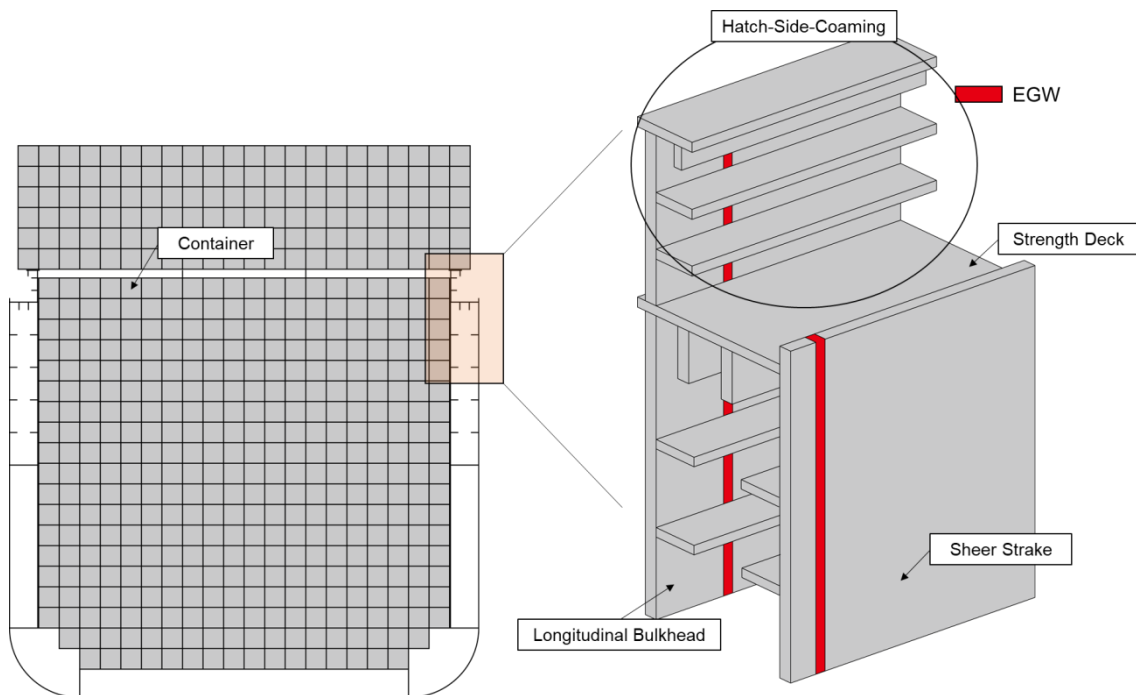
Fig. 1.2 Strength deck structure of a container ship.

1.1.2 Background of LNG-fueled ship

In recent years, the International Maritime Organization (IMO) has issued particular emission regulations. Figure 1.3 shows the schedule of SOx emission regulations. The SOx and particulate matter emission controls apply to all fuel oil, combustion equipment, and devices onboard. These fuel oil sulfur limits are expressed in term of %m/m. Emission control areas (ECAs) established in Baltic Sea, North Sea, North America, and United States Caribbean Sea have more limited the emissions than outside ECA. Therefore, in order to comply with the regulations, the ships which is operated inside these ECA need to use a low sulfur fuel oil (Marine Gasoil: MGO) with a sulfur content of less than 0.1%. However, that is significantly more expensive than heavy fuel oil and in early April 2016, the price of marine gasoil, for example, was more than double that of heavy fuel oil. In addition, low sulfur fuel oil of Marine gasoil has extremely low viscosity for fuel pumps of marine engines designed for a minimum viscosity which leads to inadequate hydrodynamic lubrication causing wear and scuffing. In order to prevent problems due to low viscosity, the installation of a fuel-oil cooler is newly required.

An exhaust gas cleaning system is an alternative method to remove sulfur oxides from ship's engine, but the problem is that the equipment itself is large which is necessary to require new space, and the initial investment cost is very high. In addition, regulations of NOx emissions have been limited in 2016, and the emission standards, for example, is shown in Fig. 1.4 which have been applied in emission control areas, and it is required to reduce NOx emissions by 80% compared to primary regulations. In order to respect and follow the regulations, it not only supports the engine, but also additional external equipment such as Selective Catalytic Reduction (SCR) and Exhaust Gas Recirculation (EGR) [10-13].

Year	Sulfur Limit in Fuel, % m/m	
	IMO ECA	IMO Global
2005	1.5	4.5
2010	1.0	
2012		3.5
2015	0.1	
2020		0.5
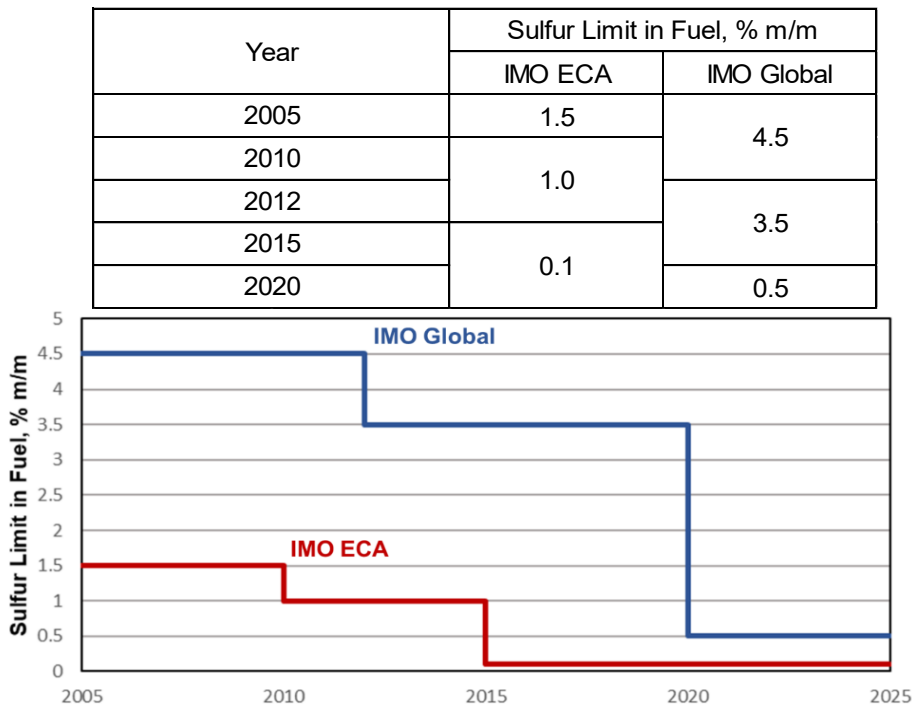
Fig.1.3 Schedule of SOx emission regulations.

Tier	Year	NOx Limit, g/kWh		
		n<130	130≤n<2000	n≥2000
Tier Ⅰ	2000	17	$45 \cdot n^{-0.2}$	9.8
Tier Ⅱ	2011	14.4	$44 \cdot n^{-0.23}$	7.7
Tier Ⅲ	2016 (ECA)	3.4	$9 \cdot n^{-0.2}$	1.96
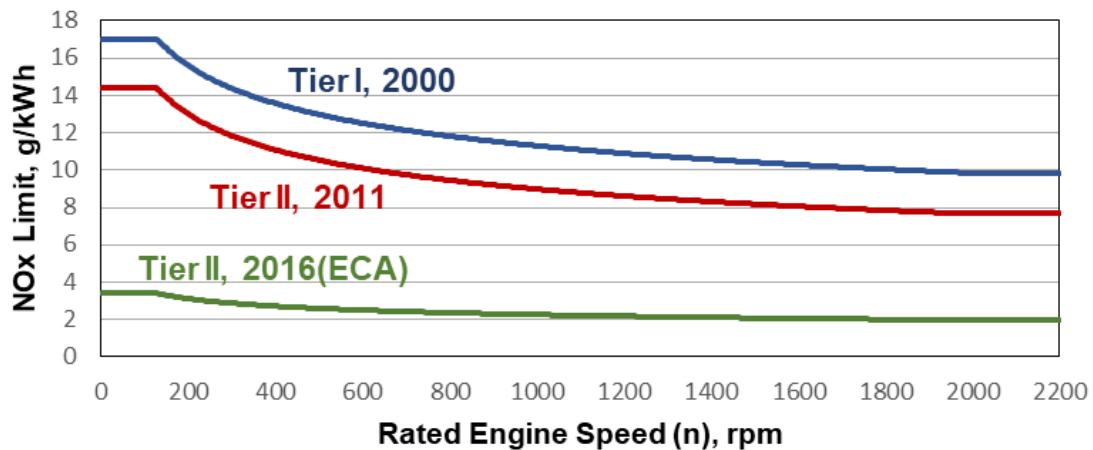
Fig.1.4 Schedule of NOx emission standards.

As per the emission regulations above, liquefied natural gas (LNG) is an alternative fuel to prove SOx and NOx emission standards. Using LNG as fuel almost eliminates SOx and particle (PM) emissions completely, and reduces NOx emission up to 85%. Therefore, the number of ships using LNG as fuel (excluding LNG carriers) is increasing fast and more. However, because LNG is stored at cryogenic temperatures under -163 °C, the steel for storage tanks needs to have high fracture resistance and strength under low-temperature conditions. Aluminum alloys, austenitic stainless steel (SUS 304), and 9%Ni steel are listed as a material that is resistant to low-temperature brittleness and applicable to LNG tanks. The 9%Ni steel is desirable due to its reasonable price compared with other materials. There are three-type tanks, a square tank, cylindrical tank and cylindrical tank for cryogenically storing and offloading LNG. The IHI-SPB LNG tank is one of the square tanks as shown in Fig. 1.5 [14-16] that has a high capacity and is usually made of aluminum alloys. On the other hand, the cylindrical tank is made of the low-cost material of 9%Ni steels. Thus, it is currently needed to develop the square tank using 9%Ni steels.

For the vertical welded joints at the inner wall of the LNG tank, automatic TIG (Tungsten Inert Gas) welding and SMAW (Shielded Metal Arc Welding) are generally used for 9%Ni steels since filler wires of Ni-base alloys are used to achieve the high toughness and brittle crack arrestability. However, the automatic TIG welding and SMAW employ multi-pass welds for a relatively large gap of the joint and long weld

length therefore that affect to a construction period and cost. Thus, in this research, the novel single-pass vertical welding process using a hot-wire laser method is studied to reduce the construction time and maintain joint properties. In addition, it is feasibly considered to reduce the deposited of a Ni-based filler wire on the welded joint by using a small groove area for the reduction of consumable cost.

Furthermore, although 9% Ni steels have been used for several decades as a structural material for the inner wall of LNG tanks, in recent years the steel manufacturer has developed a new material of a 7% Ni steel as an alternative to the 9%-Ni steel to reduce the cost of additional Ni alloy. In order to maintain properties of the base metal and welded joints of the 7%Ni steel, its alloy composition has been optimized and the latest TMCP (Thermal Mechanical Control Process) technology has been applied. As a result, the 7%Ni steel has the same excellent performance as 9%-Ni steel and it has been applied to the LNG tank. The Ni steel has been applied only the above-ground type LNG tanks so far, however, the number of LNG-fueled ships is growing up, in near future, therefore it is expected that the demand of Ni steel application to LNG tanks for ships would also increase [17-18].
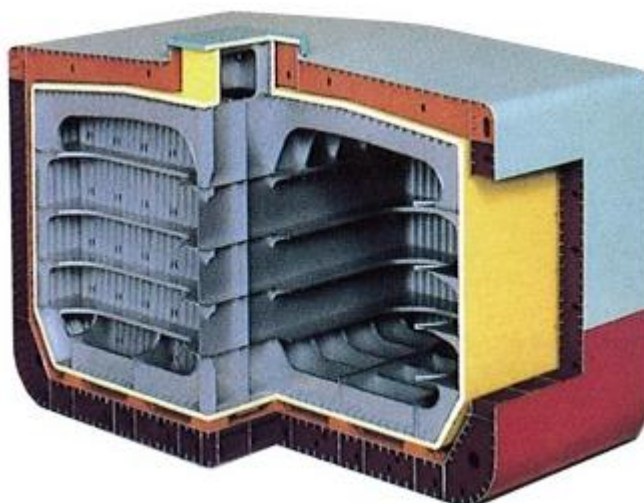
Fig. 1.5 IHI-SPB LNG tank

1.2 Objectives and construction of the thesis

A welding process plays an important role for ferrous or non-ferrous material fabrication in many industries such as shipbuilding, oil and gas plants, power plant and so on. Since the weld joint can be the weak point as a result of a heat input during welding, the advanced welding process, therefore, has been developed for making it more reliable and also optimizing construction cost.

For the shipbuilding industry, a novel single-pass vertical welding process for a thick steel plate using the combination of a diode laser as a heat source and a hot-wire system was proposed and developed in order to reduce a heat input and

maintain mechanical properties of the weld joint compared with a conventional single-pass vertical welding as known EGW.

For the LNG fuel tank construction, the novel single-pass vertical welding process was applied on Ni-steel plates to increase productivity and to reduce a groove area, which is a volume of a welding consumable of a Ni alloy. In addition, the flexibility of the hot-wire laser welding process to the thickness variation was investigated, and the weld joint properties are evaluated

This thesis emphasizes the basic ideas and investigations of the proposed process, and the optimization of welding conditions. Besides, the weld joint properties are analyzed in many kinds of method and compared with the standard requirement. Figure 1.6 shows a flow chart of the construction of the thesis.

Chapter 1 discusses the background of research in addition to the objectives and thesis statements.

Chapter 2 reviews kinds of research and theoretical information that are relevant to the high-performance structure of steel types, the vertical welding process for a heavy-thick joint, a fillet welded joint, etc. Furthermore, an innovative welding process of hot-wire laser method is discussed.

In Chapter 3, effects of a laser irradiating condition, laser energy distribution on welding phenomena and joint creation were investigated. In addition, the effect of the oxygen content in shielding gas on welding phenomena and joint creation were also studied.

In Chapter 4, based on the results of the above investigations, the optimal welding conditions were obtained in the chapter 3. In this chapter, the obtained optimal conditions were applied to large size specimens. The hot-wire laser welding system with a self-propelled base was developed in order to do the trial for the long weld joint in a practical use. Finally, the properties of the welded joint were investigated.

In Chapter 5, the principles and basic ideas to improve the laser beam control using twin diode lasers for a 50-mm heavy thick joint were introduced. The advanced laser beam control of twin diode lasers with a total power of 12 kW and a hot-wire system are used. The combination of double laser irradiating conditions was changed and its effect was investigated on base metal melting and molten pool formation. Finally, the properties of the welded joint were investigated.

In Chapter 6, the basic ideas and a method of the hot-wire laser welding process and the large size jig were applied to the 7%Ni steel plates with a long-weld length. The flexibility of the process to the thickness variation was also investigated. The welding conditions of a rectangular laser spot size, laser power, welding speed, etc. are optimized to achieve a sound welded joint. Then the welded joint appearances, cross-sections and mechanical properties are evaluated

Finally, the conclusions of this thesis are summarized in chapter 7.

Chapter 1: Introduction and research objectives

⇩

Chapter 2: Literature review

⇩

Chapter 3: A study of welding condition effects of single-pass vertical welding using hot-wire laser method

- Introduction of the novel welding process and its methodology

- Investigations of laser-irradiating conditions on the groove area using a rectangular spot beam, high-edged energy type and a weaving system

- Elucidation of oxygen-added Ar shielding gas effects on the weld joint

⇩

Chapter 4: Optimal parameters of the novel welding process in application of the large size specimen

- Introduction of the large size jig for the novel welding process

- To apply optimal parameters in large size specimen in 28.5-mm thickness

- Joint properties of 1-pass vertical welding using hot-wire laser method

⇩

Chapter 5: Development of vertical welding for heavy-thick steel plate using twin diode lasers and hot wire

- Optimization of advanced laser beam control of twin diode lasers for 50-mm thickness

- Effects of power distribution on a heavy-thick joint

- Cross-sections and joint properties of heavy-thick specimens

⇩

Chapter 6: The application of single-pass vertical welding for Ni steel plate using hot-wire laser welding

- Optimization of welding conditions for Ni steel plates with thickness of 10,15, 20mm

- Evaluation of macrograph and heat input of the welded joints

- The properties of 7%Ni steel welded joints using the proposed process

⇩

Chapter 7: Summary and future work

Fig. 1.6 Construction of the thesis.

Chapter 2

Literature review

2.1 Introduction

This chapter discusses theoretical backgrounds and literature review related to this research. It is composed mainly of single-pass vertical welding technology, development of steel plate and recent trends of vertical welding processes for shipbuilding and LNG tanks, hot-wire laser welding, and latest our research of a novel welding process.

2.2 Brief information of single-pass vertical welding process

Electroslag welding (ESW) and Eectrogas welding (EGW) are currently applied to thick-section welded joints in a vertical or near-vertical position between retaining water-cooled copper shoes. Figure 2.1 shows the schematic comparing of two vertical welding processes. ESW and EGW involve high energy input relative to other welding processes. Those of welding processes are similar to in situ casting with large volumes of molten pool and heat content.

ESW produces coalescence with molten slag with melts the filler wire and the surface of base metal. The weld pool is shielded with the molten slag that moves along with the groove vertically. An electric arc is used to create an initial molten pool and when a molten bath is achieved, the arc is extinguished and during welding, flux is added continuously to maintain an adequate slag coving over the pool. In case of low-carbon steel, the temperature of the weld pool is reported to be in the vicinity of $1925^{o}C$, while the temperature of the surface is about $1650^{o}C$. Figure 2.2 illustrates that the cooling rate of ESW is very low relative to other arc welding process [19-21].
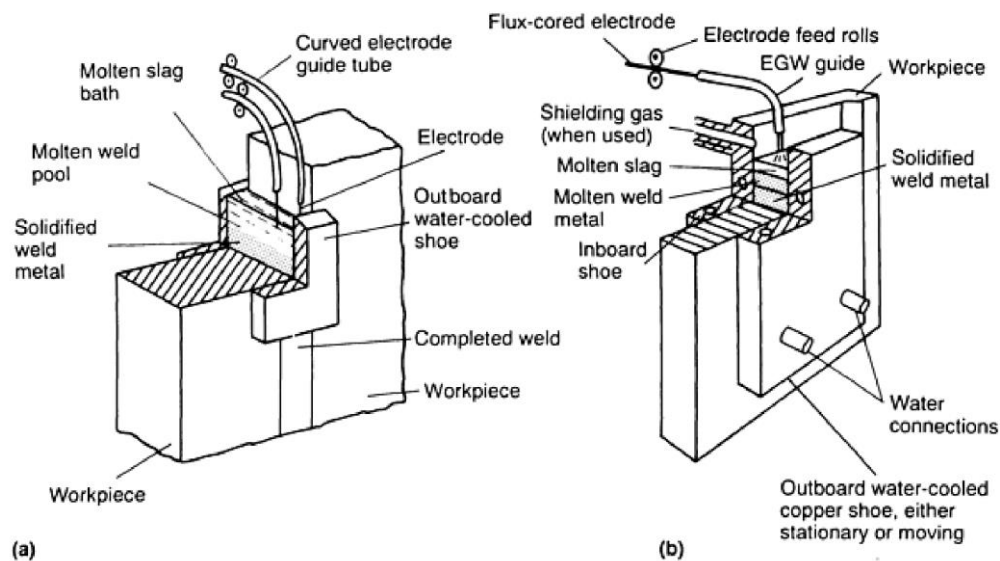
Fig. 2.1 Schematic comparing of two vertical welding processes (a) electroslag welding (b) eletrogas welding.

Figure 2.3 shows the macrograph of HAZ in an electroslag weldment. As a result of the extremely slow solidification, it results in a coarse primary solidification structure and also a very large HAZ [22].

EGW was introduced in the early 1960s [23] to perform single-pass vertical welding that can be classified as a gas-metal arc welding process. The process is very similar to ESW except the presence of an arc and the weld pool shielding mechanism. In most cases, a shielding gas is used together with either a bare or flux-cored electrode to provide a shielding gas covering the molten pool. However, self-shield flux-cored wires are often used without separate shielding gas. Moreover, EGW is generally superior to ESW having higher deposition rate that presents the lower heat input, more refined microstructure and improved HAZ properties [21].
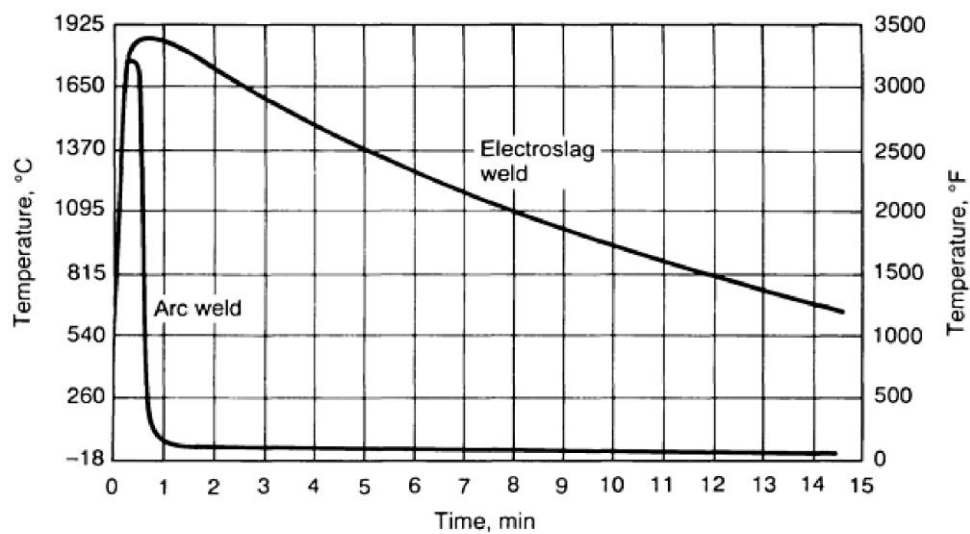
Fig. 2.2 Typical thermal cycle of an electroslag weld relative to that of an arc weld.
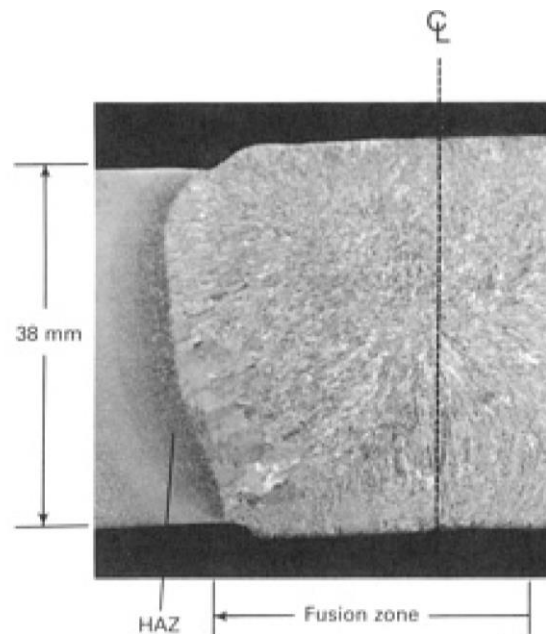
Fig. 2.3 Macrograph of weld metal and HAZ in an electroslag weldment.

2.3 Development of steel plate for shipbuilding and LNG fuel tanks

2.3.1 High strength and high HAZ toughness steel for large heat input

As a consequence of the rapid increase in the capacity of container ships, the larger container ship strongly demands the higher strength and thicker plate rather than the exists steels in order to carry as many containers as possible. An increase in the thickness, the toughness of welded joints tends to decrease due to larger heat input. According to this situation, Mitsubishi Heavy Industries, Ltd. (MHI) together with Nippon Steel Corporation developed steel plate with a yield strength of 47 kgf/mm^2 (460N/mm^2) known as YP47 steel, which enlarges approximately 20% in comparison with conventional steel plates for ship hull. This steel possesses both high strength and high toughness. In addition, the reduced plate thickness of high strength material can decrease the weight in the same size as the container ship. The first large container ship in the world using this grade was built to Nippon Kaiji Kyokai also known as ClassNK and delivered in June 2007 [24-27]. Figure 2.4 shows the cross-section and steel grades for hull structure of container ships. In case container ship size increase from 6000 TEU to 8000 TEU, the EH40 (yield strength ≥ 390 N/mm^2) and for larger than 13000 TEU container ship, EH47 is expected to be used [28-29].
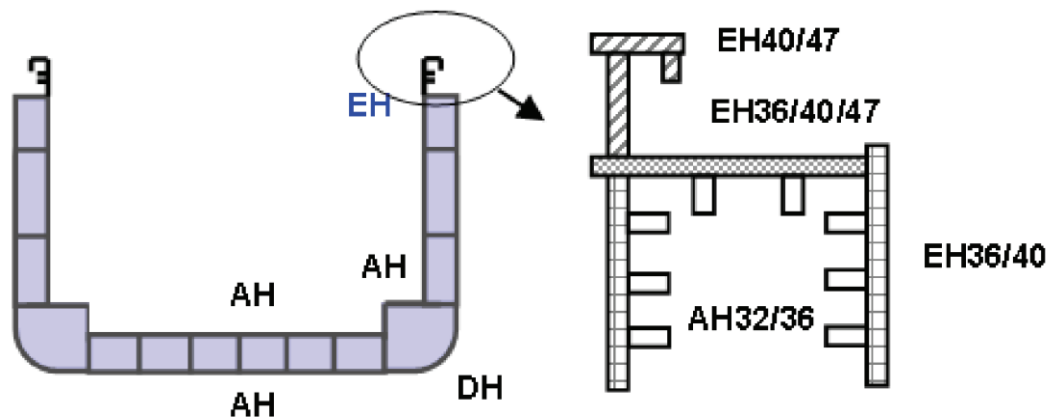
Fig. 2.4 Cross-section and steel grades for hull structure of container ships

In the meantime, the steels have been developed to be welded under the general condition of large heat input welding process of the single-pass vertical joint such as EGW. Steelmakers have improved the strength and toughness property by adding chemical elements and controlling rolling and cooling processes. The Thermal-Mechanical Control Process (TMCP) was applied to control rolling for the first time in the 1960s [30] and in 1980 NKK Corporation (now JFE steel) succeeded in applying an on-line accelerated cooling process for plates called OLAC [31-32]. At Nippon Steel, TMCP is called the Continuous Online Control (CLC) process [33]. TMCP is the most efficient method to improve mechanical properties through microstructure control. Figure 2.5 [34] shows the schematic illustration on TMCP and microstructural change in the process.
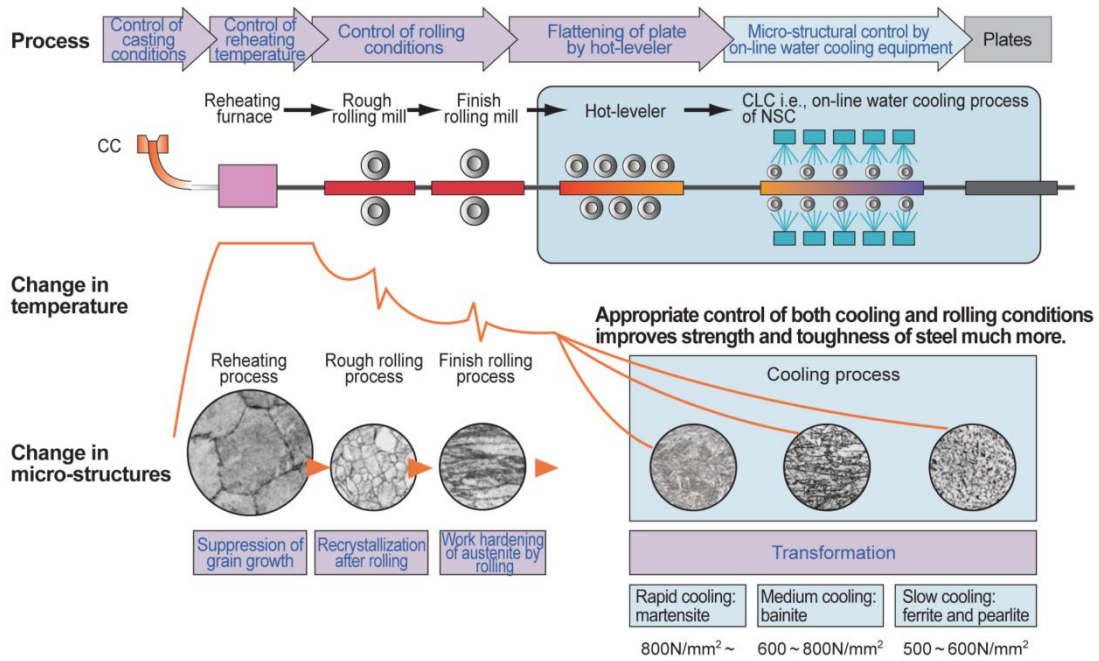
Fig. 2.5 Schematic illustration on TMCP and microstructural change in the process.

For HAZ toughness control technology, the most important point in HAZ toughness improvement is how to obtain as fine a metallographic structure of HAZ as possible. Figure 2.6 shows the progress of HAZ microstructure improvement. Nippon Steel Corporation has succeeded in developing a new technology for HAZ fine grain steel, which is called Super <u>H</u>igh HAZ <u>T</u>oughness Technology with <u>F</u>ine Microstructure Imparted by <u>F</u>ine Particles (HTUFF). As shown in Fig. 2.7, ɣ grains in HAZ of HTUFF steel are almost prevented from growing even under temperatures as high as 1,400 ^{0}C [35-36]. However, TiN steel has been also developed through controlling TiN particles, refining the microstructure of HAZ by using B, Ca and furthermore, dispersion of martensite-austenite (MA) is controlled as shown in Fig. 2.8 [37-39]. In addition, the developed YP40 and YP47 steels have been studied in the general high heat input condition to confirm the mechanical properties of welded joints [40-45].
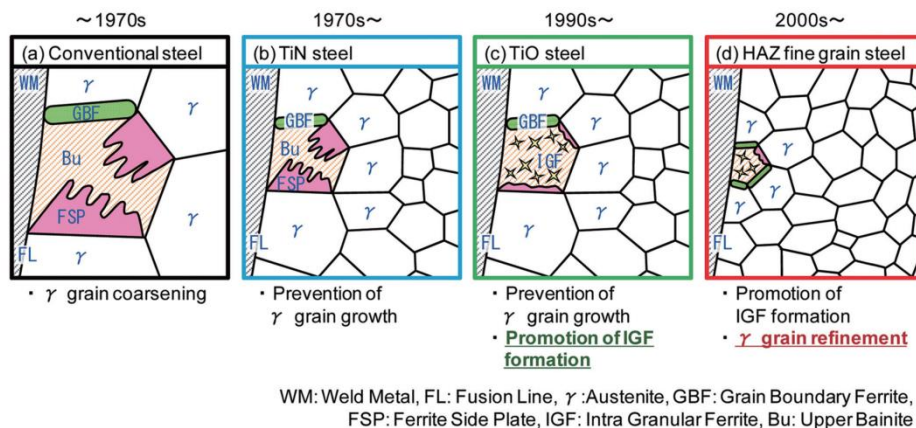
Fig. 2.6 Progress of HAZ microstructure improvement through HTUFF
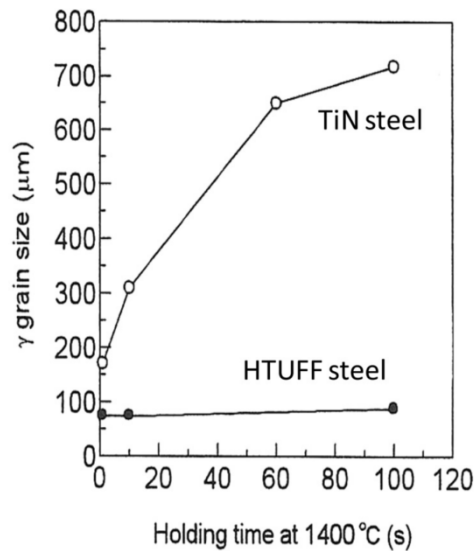
Fig. 2.7 Comparison of ɣ grain growth between conventional TiN steel and HTUFF

(a)   (b)
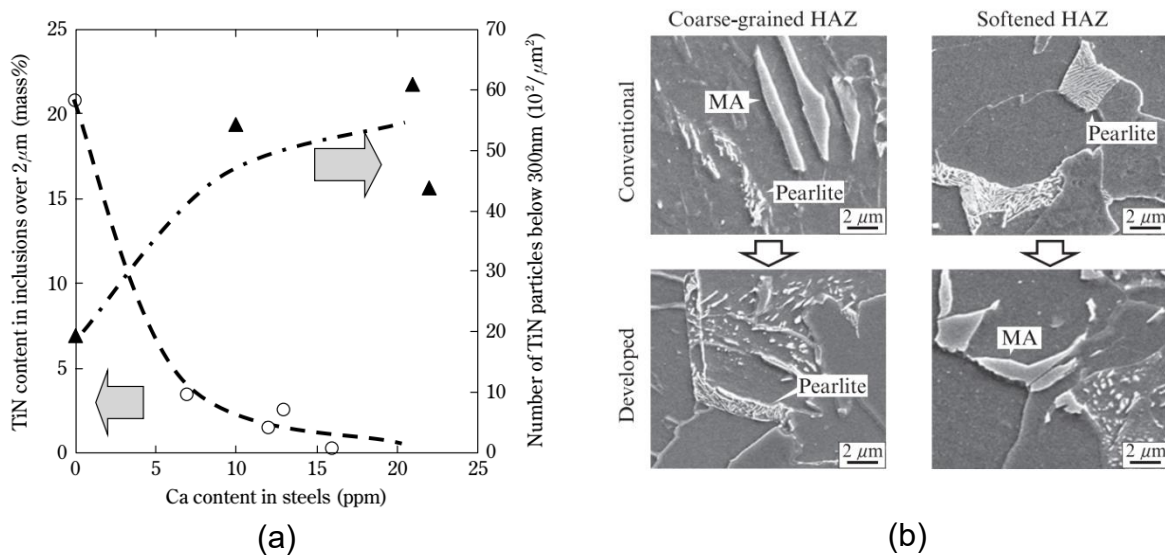
Fig. 2.8 Typical studies for development of TiN steel (a) Effects of Ca content in steels on coarse and fine TiN particles (b) Controlling MA in HAZ by reducing Si.

2.3.2 Evolution of Ni steel plate for LNG tanks

For a reasonable price, 9%Ni steel has been recognized by ASME Code for cryogenic use since 1954 and been widely used around the world as a material for the inner walls of liquefied natural gas (LNG) tanks in competition with stainless steel, other austenitic alloys and aluminum [46]. As shown in Fig.2.9, 9%Nickel steels are generally heat treated by quenching and tempering processes for high-strength steel [47-48]. Then, 9%Ni steel has been developed in heavy plates up to 50 mm thick plate [49-50]. Properties of both base metal and weld metal of 9%Ni steel weld joint are investigated in several heat treatment conditions [51-54].
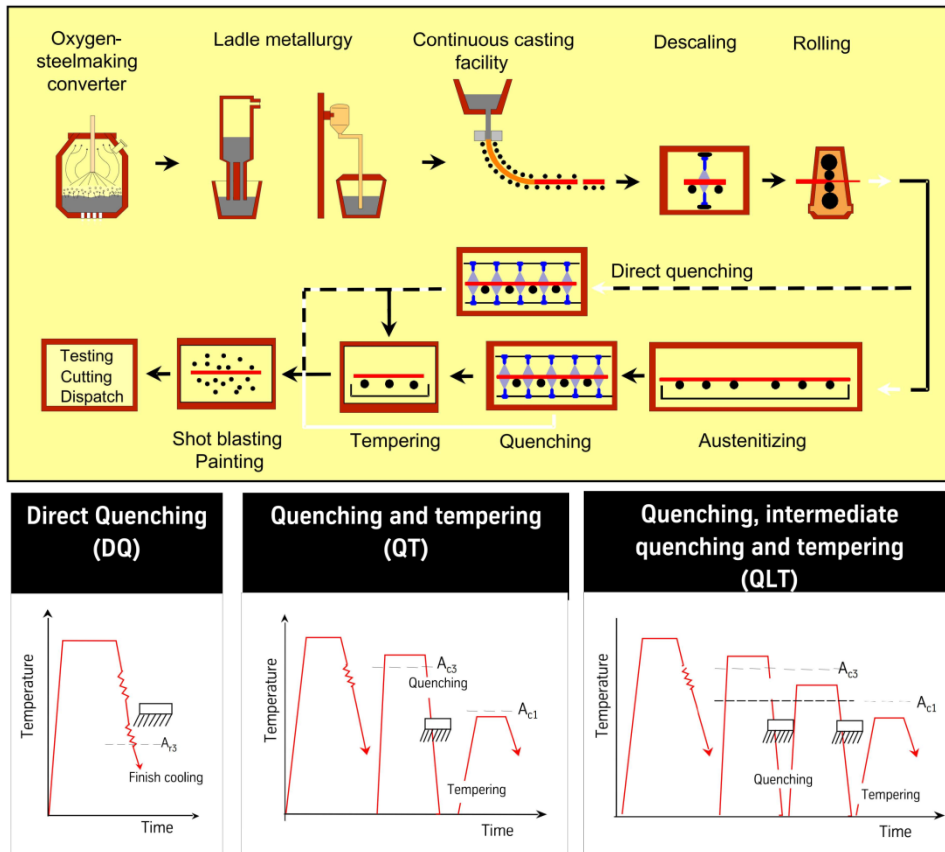
Fig. 2.9 Production process of quenched and tempered 9% Nickel steel.

The 7%Ni-TMCP steel plate for LNG tank has been newly developed by Nippon Steel & Sumitomo metal that applies a Thermal-Mechanical Control Process (TMCP) to obtain the retain austenite and refine microstructure to reinforce the inferiority of 2%Nickel as shown in Fig. 2.10. That means over 20% Nickel reduction in the nickel price and saving natural resources [55-56].
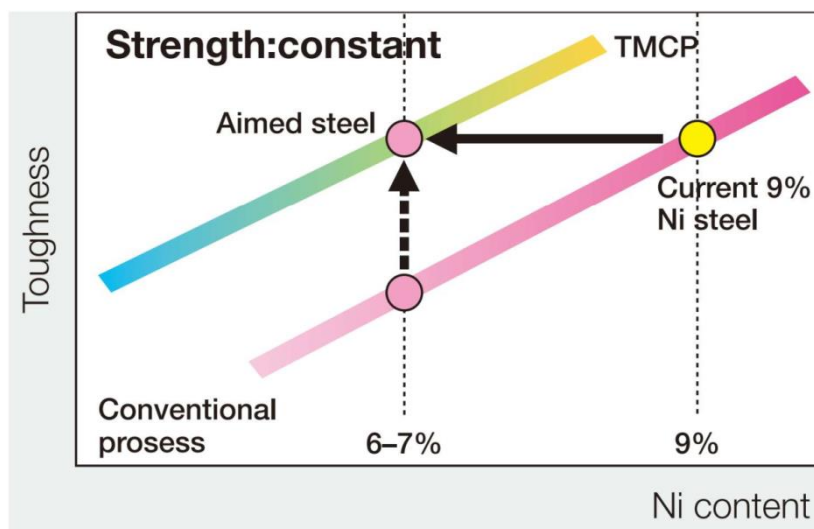
Fig. 2.10 Target for development.

In addition, Figure 2.11 shows the production process of 9%Ni steel and the new steel for an LNG tank and its microstructure. It is different from the main process of 9%Ni steel of Reheat-Quenching-Tempering (RQ-T), but the new steel of 7%Ni is produced by the production process of Thermal Mechanical Control Process-Lamellarizing-Tempering (TMCP-L-T). Fine martensitic microstructure of the 7%Ni steel is achieved when controlled rolling and direct-quenching in the accelerated cooling process are applied. 7%Ni-TMCP steel is excellent in brittle crack initiation suppressing and propagation arresting properties. And all properties are confirmed equivalent to 9%Ni steel. Furthermore, the 7%Ni-TMCP has been registered for the range of Ni composition 6.0-7.5% in JIS as SL7N590 in JIS G3127, in ASTM and ASME as Grade G of A841 since 2013 [57-60].
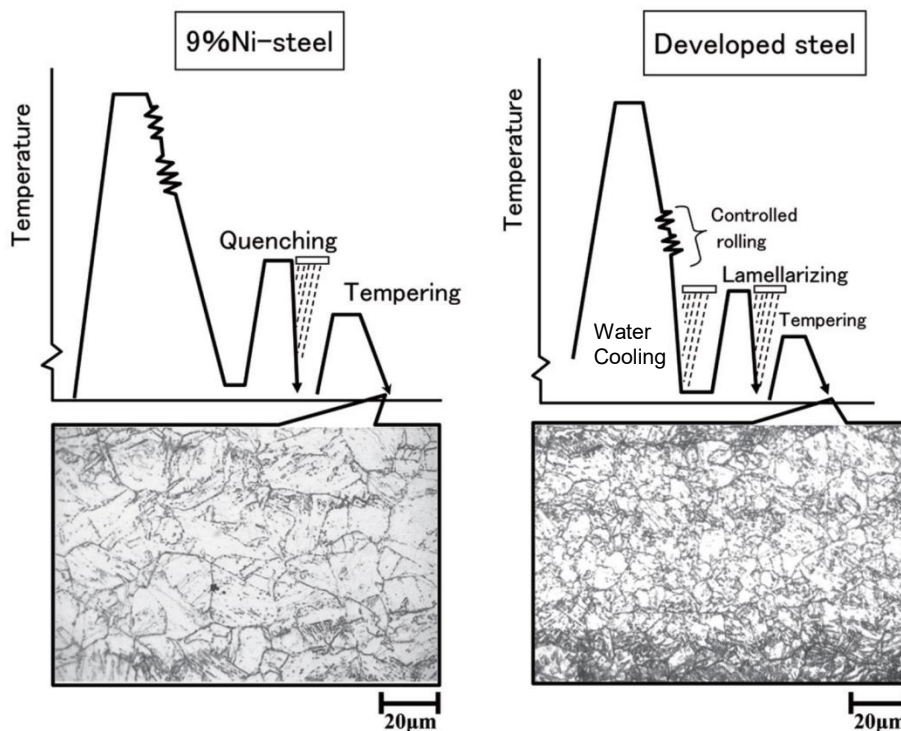
Fig. 2.11 Production process and microstructure.

2.4 Recent tends of vertical welding processes

2.4.1 Shipbuilding

In the 1970s, a single-electrode VEGA (Vibratory Electrode-gas Arc Welding) process was developed by Nippon steel welding production & engineering company limited to reduce heat input and to improve impact property of the welds. This process with an oscillating electrode is able to weld in a narrower groove, so the welding current is reduced due to a smaller diameter of filer wire used. As shown in Fig. 2.12, in the same thickness of 19 mm the weld of single-electrode VEGA shows narrow weld bead and heat affected zone. In addition, the much lower heat input can be achieved, and lack of fusion is not observed in a thickness up to 50 mm [61].

Welding processes	Plate thickness	Cross-sections of welds	Heat input
Conventional EGW	19mm		227 kJ/cm
			72 kJ/cm
Single-electrode VEGA	50mm		258 kJ/cm
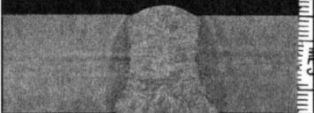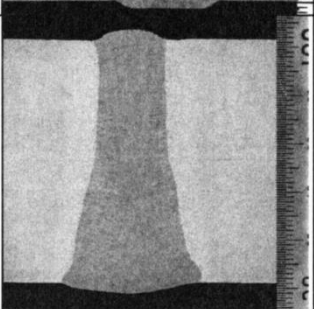
Fig. 2.12 Comparison of cross-sections of welds by conventional EGW and Single-electrode VEGA

(a) Two electrodes   (b) Four electrodes
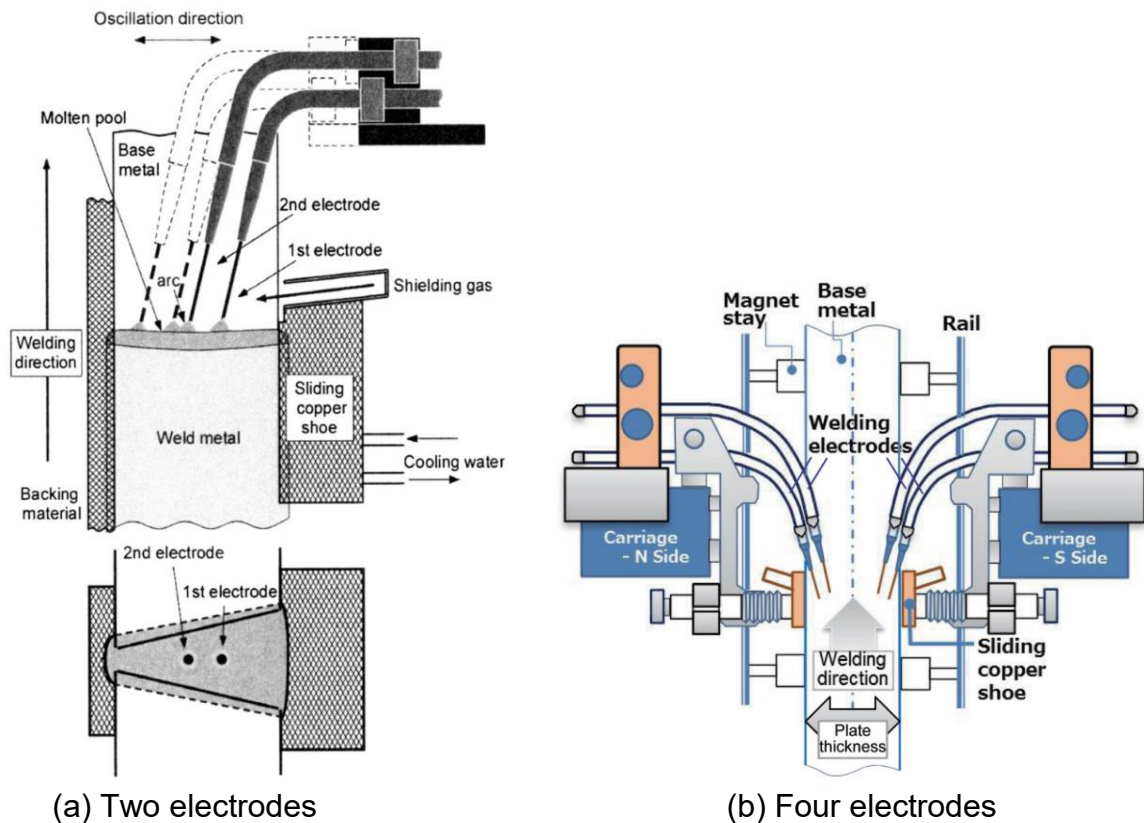
Fig. 2.13 Schematic layout of VEGA welding process (a) Two electrodes (b) Four-electrodes

However, a trend of shipbuilding is growing in size and thickness. Steel plates with a thickness of 50 mm or more have been used. Therefore, a two-electrode VEGA welding process is developed as shown in Fig. 2.13(a) and that is applied to thick plates for shipbuilding applicable to weld on the maximum thickness 80 – 90 mm. Figure 2.14(a) presents sample cross-sections of welds on the steel plates having 50, 60 and 70 mm. There are no imperfections near the front surface and the back surface of the plate often associated with it. Figure 2.13(b) shows the newly developed four-electrode VGEA welding process for thicker plates in the range 100 – 200 mm. As shown in Fig. 2.14 (b), the macrostructures of weld joints 100 mm and 200 mm even in one-pass welding of a 200-mm-thick plate obtain good trough-thickness penetration without any defects [61-62].

(a) Two-electrode VEGA   (b) Four-electrode VEGA
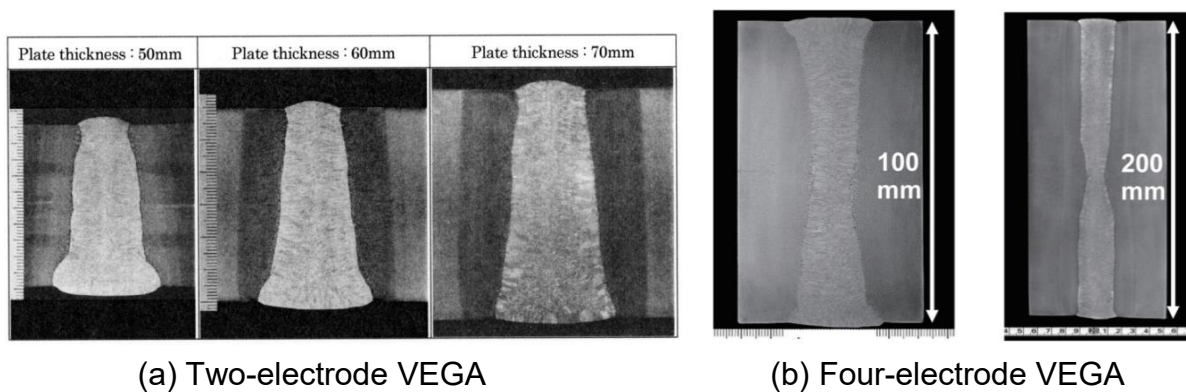
Fig. 2.14 Macrostructure of welds with (a) two-electrode and (b) four-electrode VEGA welding process.

2.4.2 LNG tanks

Regarding low-temperature material, it is used to store liquefied natural gas at under -163 ^{o}C. The toughness property of the weld joint should be considered to ensure the safety of LNG storage tanks. The various welding processes such as tungsten inert gas (TIG), flux cored arc welding (FCAW) and gas metal arc welding (GMAW) affect the fracture toughness in weldments differently [63]. For vertical welded joint, shielded metal arc welding (SMAW) has mainly been applied in LNG tanks made of 9%Ni steel overseas, but automatic TIG welding has been used increasingly in Japan since the 1980s and then remote controlled automatic TIG welding equipment and a high-efficiency automatic TIG welding method (SEDAR-TIG) have been developed by IHI engineering [64-65] to use in practice. However, in the oversea field, SMAW is still mainly used for vertical joint due to the limitation of equipment available to the subcontractor. In order to increase deposition rate, IHI developed vertical Submerged Arc Welding (vertical SAW) which has been limited to flat and horizontal positions so far. Figure 2.15 shows the schematic illustration of vertical SAW. The vertical SAW uses a smaller wire of 1.2 mm in diameter, so the arc current and heat input become lower than a conventional SAW. The cross-section is shown in Fig. 2.16 and no imperfections can be observed [66].
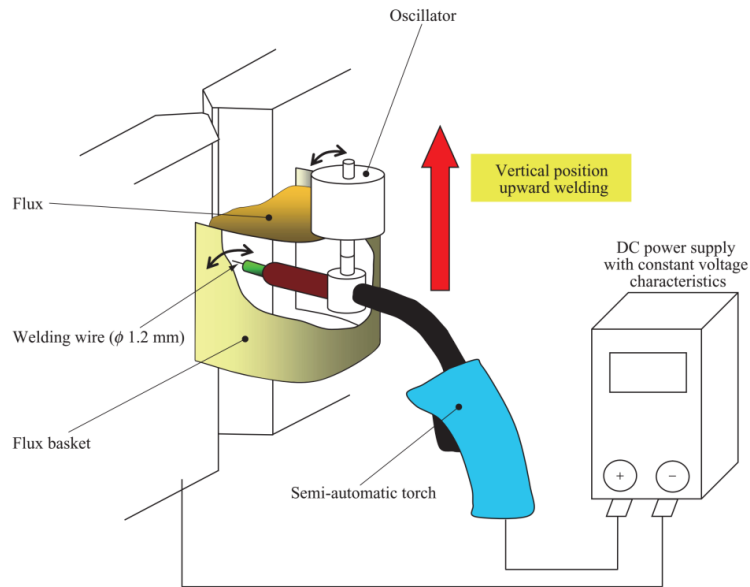
Fig. 2.15 Schematic illustration of vertical SAW.

(Note)   1 - 5 : Pass sequence
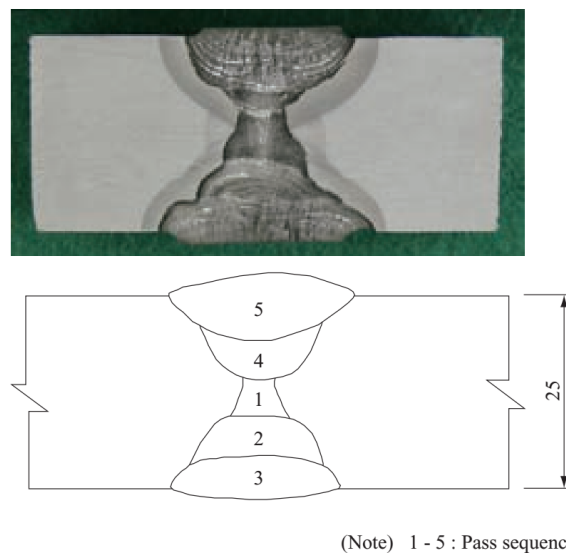
Fig. 2.16 Macrostructure and pass sequence.

2.5 Laser beam welding and hot wire method

Laser beam welding (LBW) is a welding process using a laser to joint pieces of metal or thermoplastic. The LBW allows extremely concentrating power density of laser spot which results in narrow and deep weld bead, small HAZ and high-speed welding that is a low heat input welding process. Moreover, laser keyhole welding having high laser power requires a very high power density to create deep penetration welds for welding thick plates in 1 pass [67-70]. However, LBW with the inclined welding positions of horizontal and vertical direction can lead to more defects of pores and undercuts which are difficult to achieve a sound weld joint because of action of gravity [71-73].

17

A Hot-wire system is an electrically heated filler wire up to its melting point as shown in Fig. 2.17 [74]. A hot-wire power source supplies electricity from the contact tip to the workpiece through wire feeding during welding by Joule heating. Figure 2.18 illustrates temperature distributions on filler wire. Wire current of 133A obtains a higher temperature than the current of 121A [75]. The hot wire is used as deposited weld metal which is able to increase the deposition rate. In order to increase welding and reduce heat input, it is therefore investigated welding phenomena and combined with conventional welding processes such as GTAW [75-77].
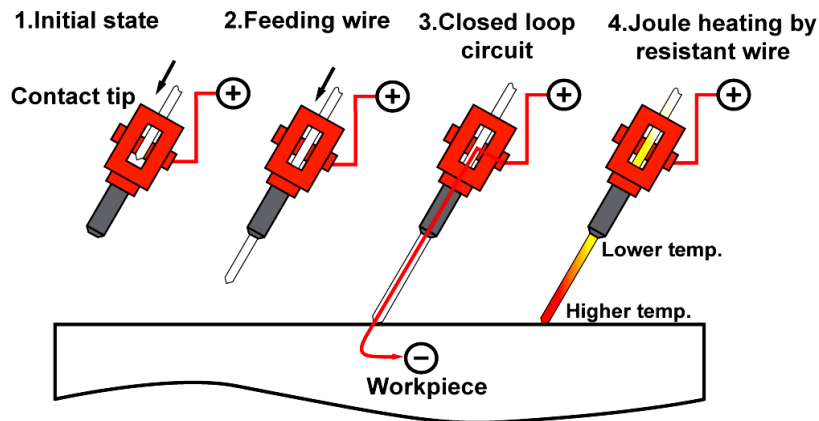
Fig. 2.17 Schematic layout of a hot-wire system
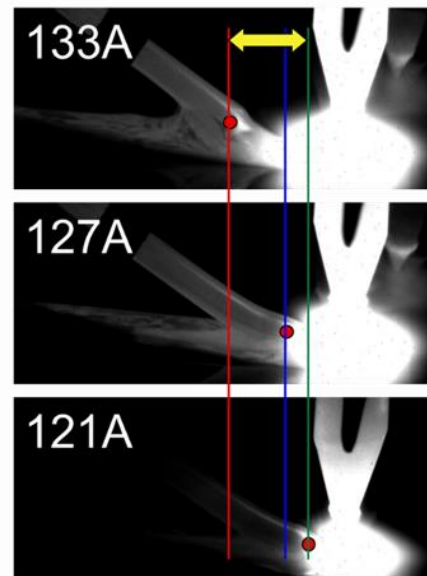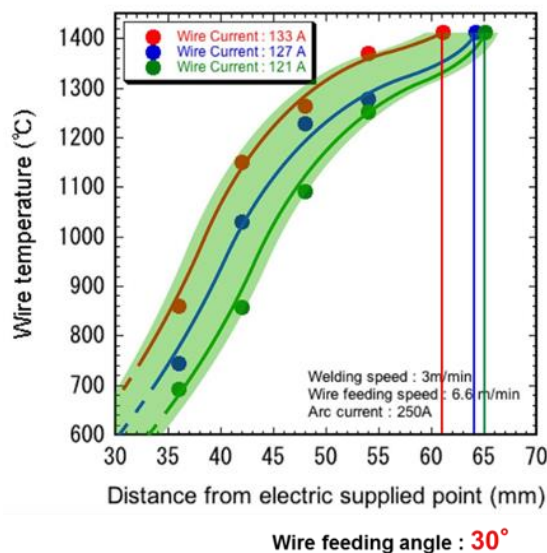
Fig. 2.18 Effect of wire current on temperature distributions of filler wire.

Hot-wire laser welding (HLW) is the novel welding process by combination a laser as a main heat source and the hot-wire system to preheat a filler wire during welding. This process can improve a deposition rate as well as reduce laser power and heat input. The application of this process has been investigated in many kinds of fields, for instance, the lap joint of the high tensile/ultra-high tensile strength steels with a wide gap for an automobile body [78], fillet welded joints of medium-thick plate for shipbuilding and bridge [79-80], and a narrow-gap joint to reduce large shrinkage and residual stress. The reflection of laser irradiation is also investigated that is a particular characteristic of laser beam welding. Figure 2.19 shows a high-speed image and a cross-section of the laser beam reflection effect [81-82].
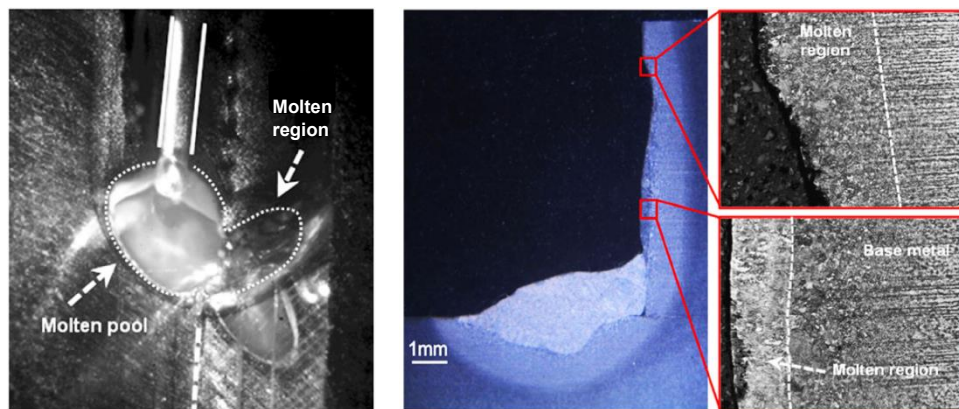
Fig. 2.19 Effect of laser beam reflection welded by a laser with a hot-wire feeding.

2.6 A novel single-pass vertical welding process using hot-wire laser

In previous studies, the conceptual idea of the new single-pass vertical welding method is proposed to reduce the heat input and laser power as shown in Fig. 2.20. Preliminary investigations in welding phenomena by combining a diode laser with a large rectangular beam spot and hot-wire feeding system were performed on steel plates. In addition, the effects of welding conditions such as laser power, the weaving of laser beam spot, gap width, laser irradiating angle, etc. were investigated [83-86].
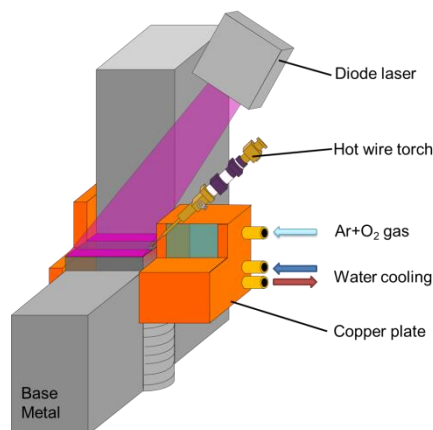
Fig. 2.20 Schematic illustration of single-pass vertical welding using hot-wire laser.

Chapter 3

A study of welding condition effects of single-pass vertical welding using hot-wire laser method

3.1 Introduction

Previous studies of single-pass vertical welding using a hot-wire laser method have presented the conceptual idea and preliminary investigations in welding phenomena of the combination of the diode laser as a heat source and the hot-wire system to a large tolerance gap. There are many conditions varied for making this system steady such as laser power, gap width, weaving system, laser beam angle, the number of hot-wire feedings and so on.

In this chapter, the methodology introduction of a joint configuration and equipment, and optimization on specific welding conditions of the proposed welding process are presented. A small size jig used for a small specimen is described a conception of a welding operating mechanism to combine laser irradiating and hot-wire feeding for a vertical welding process, and it is applied for the investigation of welding phenomena.

Effects of power density of beams, laser energy distribution and the rectangular laser spot with high-edged energy density are studied on welding phenomena and joint creation to optimize laser power and heat input. The laser spot size and its motion by a weaving system strongly affect the optimization of laser power distribution and melting phenomena. The effects of oxygen additions in Ar shielding gas are also investigated on welding phenomena and weld bead creation.

3.2 Methodology and welding conditions of single-pass vertical welding using hot-wire laser method

In this chapter, the effects of welding conditions on welding phenomena and joint creations were investigated in order to verify and optimize a novel welding process of single-pass vertical welding which is combined with a diode laser oscillator using a relatively large rectangular beam and single hot-wire system into the small size jig. The laser power density and laser energy distribution was considered first on a thick specimen with a relatively large gap of 10 mm to achieve the steady welding phenomena and the sound joint creation of the proposed process. Therefore, this section describes the basics and apparatuses of hot-wire laser single-pass vertical welding and emphasizes optimizing the particular welding parameters.

3.2.1 Introduction of a joint configuration and equipment of the novel welding process using in the small size jig and specimen

Firstly, the basics of the hot-wire laser single-pass vertical welding and the experimental set-up of the small size jig and specimen are presented schematically. Secondly, the materials used in this chapter are shown and then the basic idea as well as the investigation methodology of melting phenomena in the proposed process is introduced.
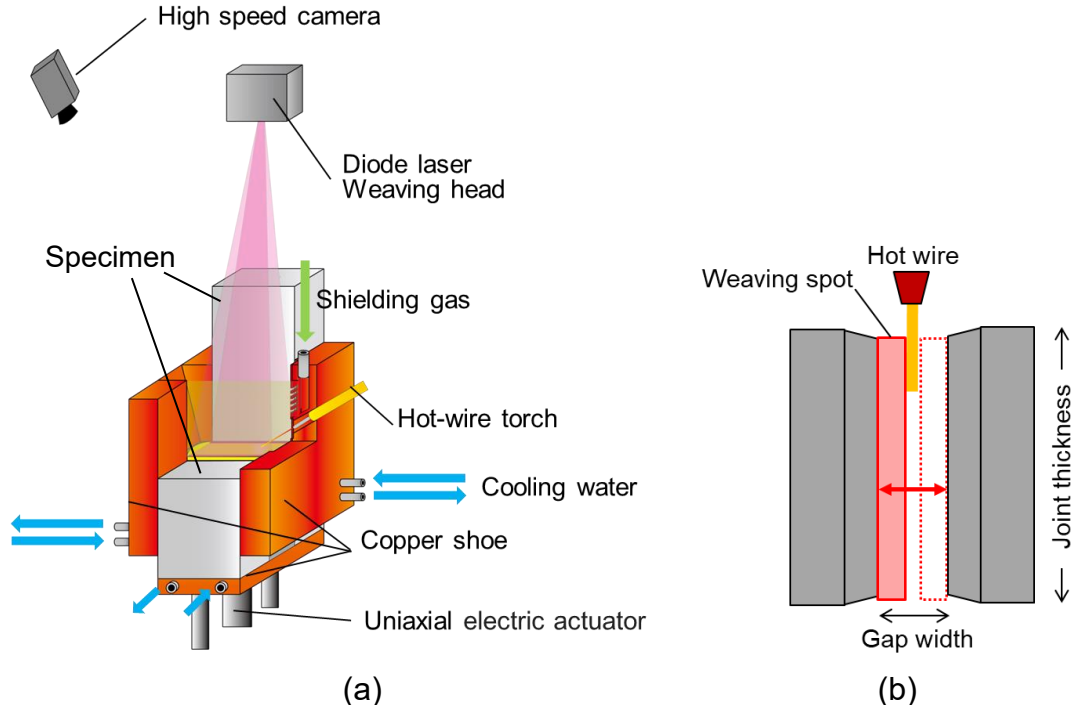
Fig. 3.1 Schematic layout of the small size jig and specimen of the proposed process
(a) a joint configuration and overall equipment (b) the top view of large rectangular laser beam irradiation through on a weld joint.

Figure 3.1(a) shows the schematic layout of a diode laser beam, a hot wire, a specimen and the apparatus of a small size jig. A specimen was set between copper shoes and moved towards the opposite side in the vertical welding direction by a uniaxial electric actuator. The water-cooled copper shoe was used for backing material. Its design was to keep a weld pool shape of both wire feeding side and back side. The copper shoe had slots for inserting a hot-wire torch, shielding gas, and cooling water. An electrically-heated filler wire up to its melting point as called hot-wire was fed into the molten pool. A diode laser used as a heat source combined with focusing and homogenizing lenses to create an adjustable rectangular shape and the spot size according to the thickness and gap width of the used plate. A high-speed camera was used to monitor weld pool formation, welding stability, and hot-wire feeding during welding. Figure 3.1(b) shows the schematic layout on the top view of the weld groove. The large rectangular laser spot having the length fitting the specimen thickness was placed along with the groove surface. The width of the rectangular laser spot was changed up to the 10-mm gap to vary the laser energy density. The weaving system was used to sweep the rectangular laser spot in the parallel direction to the gap width when the narrower laser spot width was employed.
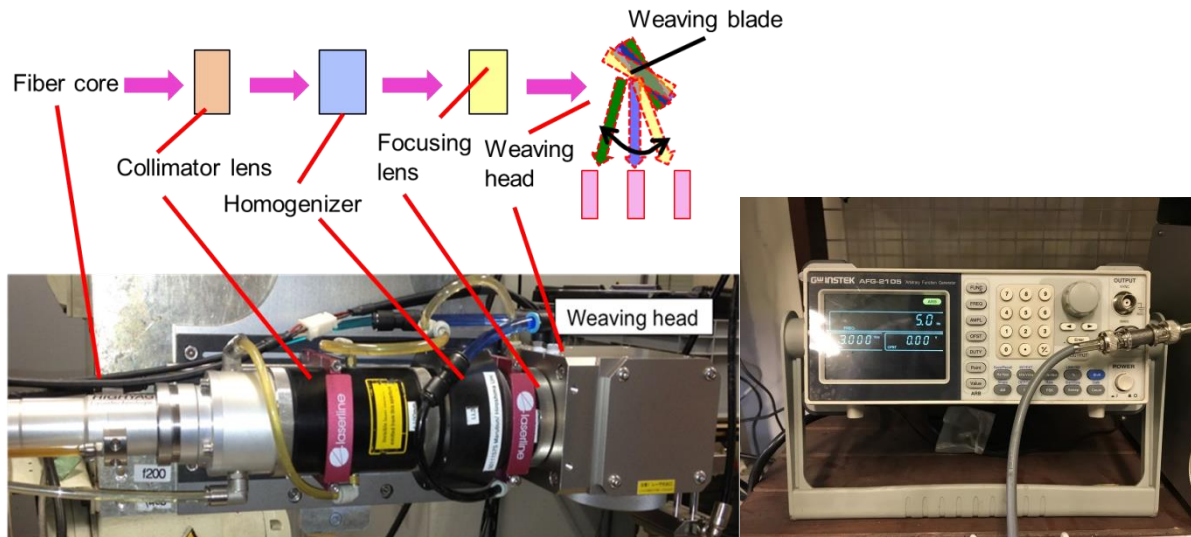
Fig. 3.2 Laser head and weaving system for rectangular laser spot.

Figure 3.2 illustrates the constituent of a laser head to create a rectangular laser beam which is combined with a weaving system. A fiber core leads the laser beam to a collimator lens in order to create a straight and large size laser spot, then the laser beam is conveyed to a homogenizing and focusing lenses which changes the shape of a laser beam from circle to rectangle. Thereafter the focal length of the rectangular laser beam depends on the focusing lens closed with homogenizer. Moreover, a weaving head was employed to move the beam on a groove area in this study. The laser beam incident on a weaving blade is reflected perfectly and the weaving blade is swept by a harmonic motor. The weaving motion can be controlled

by a controller unit to adjust a weaving waveform, amplitude and frequency. Further details of the weaving motion are discussed in 3.2.3.1.

Table 3.1 shows the length and width of rectangular laser spots created by the combination of optical lenses and a fiber core diameter. The combination of the fiber core diameter, collimator lens and focusing lens decides the rectangular beam width and the beam length can be adjusted by changing the combination of a homogenizing and focusing lenses. For instance, the combination of a 1-mm fiber core, 100-mm collimator, LL2.35 homogenizer and 400-mm focusing lens creates the rectangular laser beam having the 26-mm length and 4-mm width at a just focus. In this study, the laser beam length was adjusted to the base metal thickness.

Table 3.1 Rectangular beam shapes with combinations of optical lenses and fiber core.

| | Type (Homogenizer) | Focal length (Focusing lens) | | | | | | |
		200	250	400	500	600	800	1000
Laser length	LL2.20	23	28	45	56	68	90	113
	LL2.35	13	16	26	32	39	51	64
	LL2.35-edge	13	16	26	32	39	51	64
	LL2.54	8	11	17	21	25	34	42
	LL2.85	5	7	11	13	16	21	27
	LL2.146	3	4	6	8	9	12	15
Laser width	Colli 100 mm (Core 0.4)	0.8	1.0	1.6	2.0	2.4	3.2	4.0
	Colli 80 mm (Core 0.4)	1.0	1.3	2.0	2.5	3.0	4.0	5.0
	Colli 100 mm (Core 1)	2.0	3.0	4.0	5.0	6.0	8.0	10.0
	Colli 80 mm (Core 1)	2.5	3.1	5.0	6.3	7.5	10.0	12.5

Fig. 3.3 Diode laser oscillator.

The continuous wave (CW) diode laser was used in this research. The laser oscillator as a heat source is shown in Fig. 3.3. The laser oscillator is Laserline LDF 6000-40 with a limited laser power of 6 kW. Four wavelengths of 910, 940, 980 and 1030 nm are employed to irradiate laser power as a high-power heat source.

(a) (b)

(c) (d)
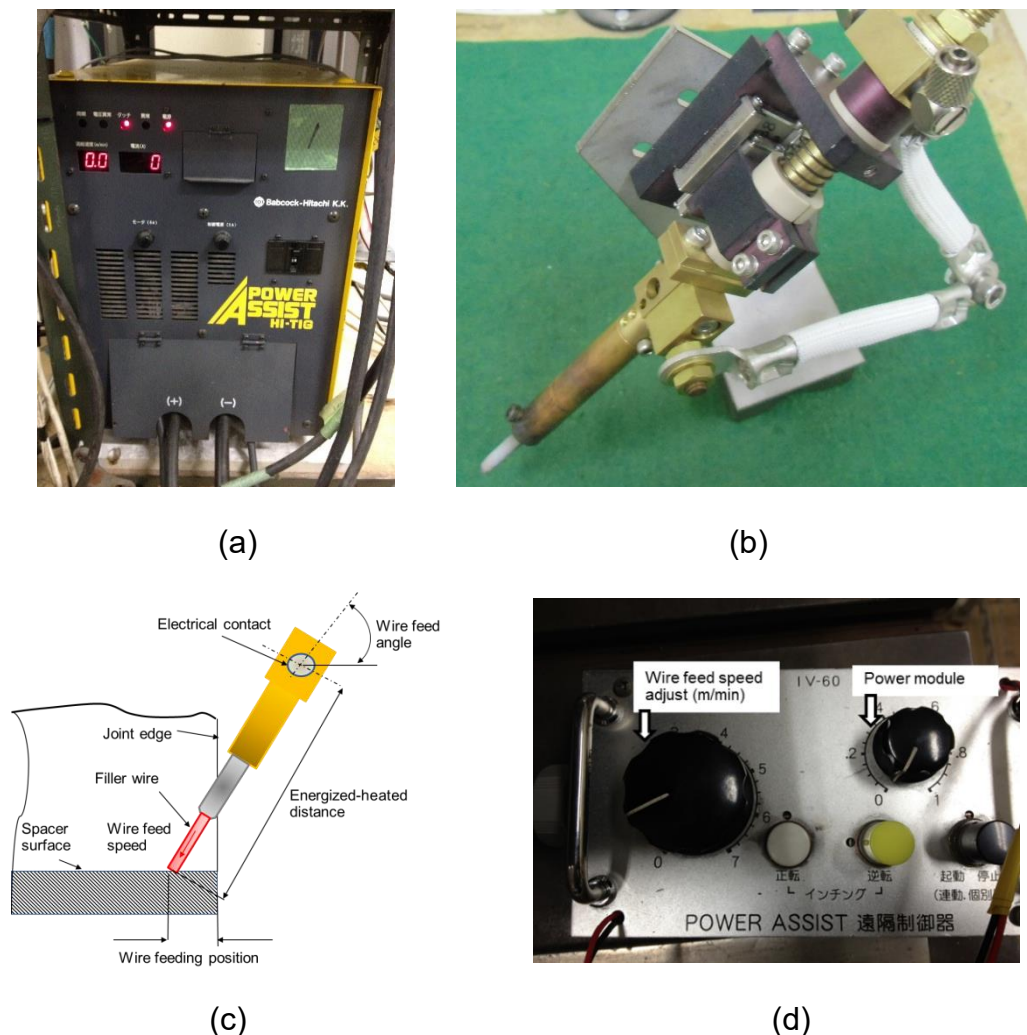
Fig. 3.4 Hot-wire equipment (a) Hot-wire power source, (b) Hot-wire torch, (c) Hot-wire setup parameters and (d) Remote controller.

Hot-wire equipment is shown in Fig. 3.4. A hot-wire power source in Fig. 3.4(a), which is Power Assist HI-TIG IV662, supplies a pulse current with its maximum average current of 165 A. A positive pole is usually connected to a hot-wire torch as shown in Fig. 3.4(b) and (c). Essential parameters for hot-wire setting are a wire feed speed (m/min), energized-heated distance (mm), a wire current (A), a wire feeding angle (°), and a wire feeding position (mm). All of the essential parameters are drawn as the schematic illustration in Fig. 3.4(c). The wire feeding speed is adjusted as a depending on a groove size and the welding speed. In the practical use of the proposed process, it was set at of 1.2-times large value compared to the calculated value. The energized-heated distance affects the filler wire temperature by Joule heating and the optimum wire current. The wire feed position and the wire feed angle

slightly affect wire melting. The wire current that should be adjusted adequately depending on the feeding speed, a wire diameter, wire material and laser energy on a wire tip. In this study, the setting of the wire feeding speed and wire current were adjusted by the hot-wire remote controller as shown in Fig. 3.4(d).

Fig. 3.5 High-speed camera equipment.

Figure 3.5 shows the high-speed camera equipment for an observation during welding. The camera of Pencil camera V-193-M1 model was used connected with NAC: MEMRECAM GX-5 module. The high-speed camera was provided to monitor molten pool creation and hot-wire feeding during welding operation in order to make clear the welding mechanism.

Fig. 3.6 Shielding gas mixer.

Figure 3.6 shows a shielding gas mixer. In order to mix oxygen (O_2) with argon shielding gas (Ar) for the investigation of the O_2 effect on joint creation, a shield gas mixer (Log MIX, manufactured by Front Corp.) was used. This mixer has a maximum

flow rate of 10 l/min for Ar and 2 l/min for O_2. The flow rates of each shielding gas condition can be changed by varying argon and oxygen flow rates concurrently.

3.2.2 Materials used

KE-47 steel plate was used in this study. It must be noted that material of YP47 steel is equivalent to KE47 steel. It hereby is called KE47 steel as the base metal. The dimensions of a small size specimen are 100 (width) x 200 (height) x 26 mm (thickness) as shown in Fig. 3.7. Two specimens were fixed and aligned as a vertical joint configuration. The square groove was set with a 10-mm gap using a bottom spacer having dimensions of 10 (width) x 20 (height) x 28.5 mm (depth). The filler metals of YM-60A (JISZ3312G59JA1UM3M1T) and YM-80A (JISZ3312G78A4UMN5C1M3T) with a diameter of 1.6 mm were used. Those filler wires are a solid wire for MAG (Metal Active Gas) having 590 MPa-class and 780 MPa-class tensile strength respectively. The chemical compositions of the base metal and filler metals are presented in Table 3.2.

Table 3.2 Chemical compositions of base metal and filler wire.

Materials	Chemical Composition, wt%											
	C	Si	Mn	P	S	Al	Cu	Ni	Nb	Ti	Cr	Mo
KE-47	0.09	0.07	1.52	0.007	0.002	0.014	0.32	0.69	0.01	0.01	0.02	0.00
YM-60A	0.06	0.35	1.45	0.010	0.007	-	0.20	-	-	-	-	0.38
YM-80A	0.06	0.40	1.69	0.006	0.003	-	0.20	3.01	-	0.05	0.46	0.29
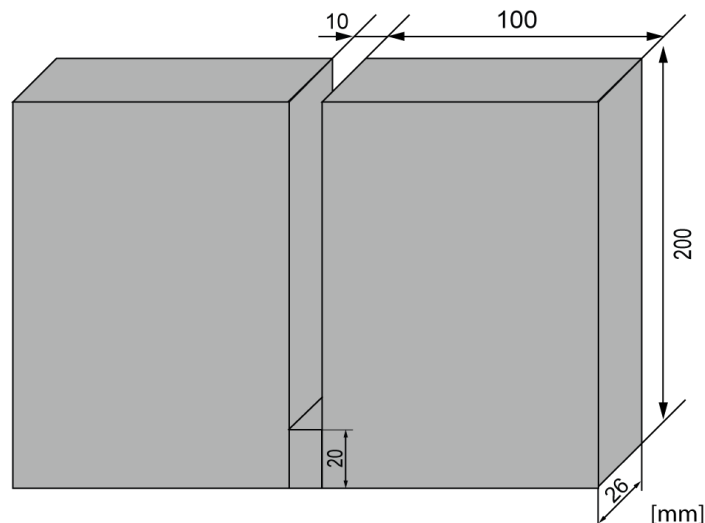
Fig. 3.7 Specimen dimensions used to optimize welding conditions.

3.2.3 Methodology for investigation of effect of laser power density and laser energy distribution on welding phenomena

The principal factor of the proposed welding process to get a sound joint is adequate laser power density in order to keep the molten pool and to melt the base metal as shown in Fig. 3.8. As the main heat source is only laser power, the rectangular beam shape should be controlled. As shown in Fig. 3.9, when the proposed process is applied to a thick-joint and a large-size laser beam is used to fit a groove area, the average power density becomes low and spreads the whole groove stably. It is good at keeping the molten pool but poorly melting the base metal. In this case, the welded joint needs more laser power to melt the base metal; however, the increase in a laser power gives higher initial cost and heat input. In the proposed process, the narrower laser spot than a gap is employed and combined with a weaving system to control laser beam motion throughout the gap. This method can increase the heating energy around the groove surfaces and thus can improve base metal melting, but the heating energy on a middle of molten pool is decreased. Since the hot-wire system does not need much laser power to melt itself, the heat energy from the laser irradiation on the middle of the molten pool can be optimized. Consequently, the novel welding process is developed to reduce laser power consumption and to achieve a low heat input process.
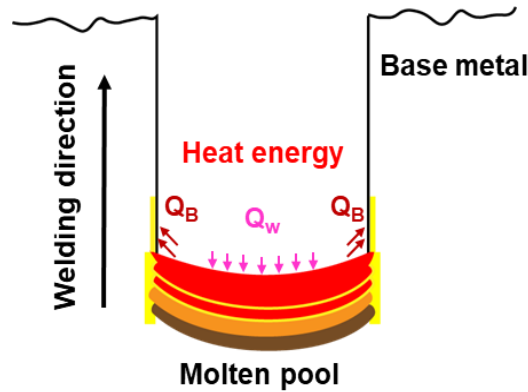
Fig. 3.8 Basic of welding phenomena.

Large size	Narrow size	Middle size
Joint thickness	Joint thickness	Joint thickness
Low power density beam	High power density beam	Middle power density beam
Good at keeping molten pool	Good at melting base metal	Good at melting base metal
Poorly melting base metal	Poorly keeping molten pool	Fairly keeping molten pool

Fig. 3.9 Effects of laser beam size on welding phenomena.

3.3 Optimization of laser-irradiating conditions on welding phenomena and joint creation

The weaving motion is the movement of a narrow rectangular laser beam throughout a gap. When the laser beam is moving, the laser energy density also is being changed due to distinctive interaction time. It accords with weaving frequency and weaving waveform. Figure 3.10, for example, shows the characteristic of the weaving waveform and frequency using the measured actual oscillating signal. Figure 3.10(a), (b), (c) and (d) are 5-Hz sine wave, 15-Hz sine wave, 5-Hz exponential wave, and 15-Hz exponential wave respectively. The weaving amplitude indicates the laser beam moving distance on the gap direction. In this case, the 5-mm moving distance from groove center toward both groove sides is applied. Changing the weaving waveform, sine and exponential waves affects the interaction time near the groove surface largely.
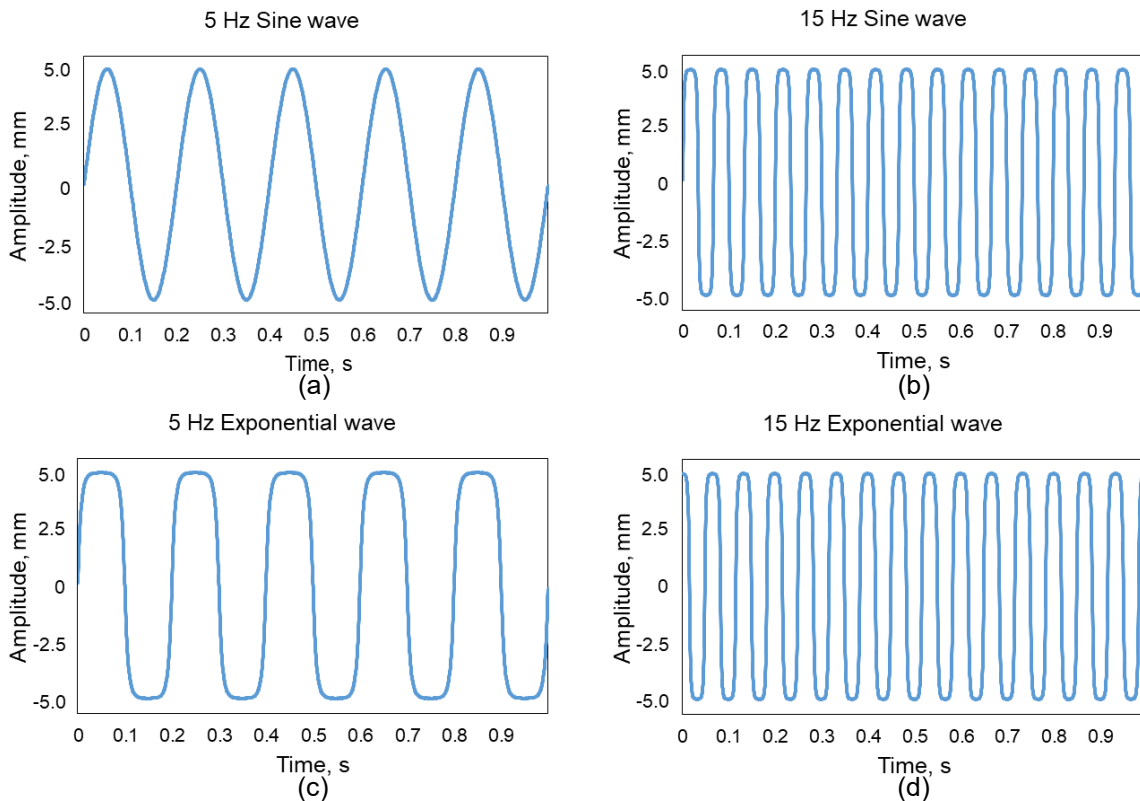
Fig. 3.10 Weaving waveform and frequency (a) 5-Hz sine wave (b) 15-Hz sine wave (c) 5-Hz exponential wave (d) 15-Hz exponential wave.

Table 3.3 presents the interaction time of each weaving condition indicated in Fig. 3.10. To clarify the effects of the weaving waveform and frequency on groove surface melting and molten pool formation, the pulse duration time while holding near the groove surface and moving on the middle groove are calculated. An exponential waveform has longer interaction time on a groove wall than a sine waveform at the same frequency. On the other hand, the exponential waveform has a shorter interaction time in the middle zone.

Table 3.3 Interaction time for typical weaving conditions.

Exponential waveform	1 cycle	Holding time on a groove wall	For 1 s	Moving time in 1cycle	For 1 s
	ms	ms	ms	ms	ms
5 Hz	200	72.5	362.5	55	275
15 Hz	66.67	25	375	17	255
Sine waveform	1 cycle	Holding time on a groove wall	For 1 s	Moving time in 1cycle	For 1 s
	ms	ms	ms	ms	ms
5 Hz	200	34	170	132	660
15 Hz	66.67	11.5	172.5	44	660

The evaluation of the laser energy density of a weaving beam and average laser power density is shown in equations (3.1), (3.2). E is the laser energy density irradiation during 1 cycle, P_{peak} is the power density on the beam, t is the interaction time during 1 cycle weaving, f is the weaving frequency and P_{ave} is the average laser power irradiating during 1 cycle.

$$E = t \times P_{peak} , \text{J/mm}^2 \qquad\qquad (3.1)$$

$$P_{ave} = E \times f , \text{W/mm}^2 \qquad\qquad (3.2)$$

As shown in Table 3.3, the exponential waveform takes longer time near the groove wall than the sine waveform does on the same weaving frequency. It means that the laser irradiation with the exponential waveform obtains higher laser energy and more average laser power density on the groove walls.

It finds the interaction time during 1 cycle changes largely depending on the weaving frequency even if the same waveform is used. In one cycle, the 5-Hz weaving frequency has a longer holding time than the 15-Hz weaving frequency, this means that the 5-Hz frequency irradiates the higher laser energy near the groove walls, but in one second both 5 Hz and 15 Hz frequencies have the similar average laser power. The previous investigation has cleared that the pulse interaction time in the one cycle has affected the melting efficiency strongly and it has been considered rather than the interaction time in one second. Thus, the 5-Hz exponential waveform was applied in this study.

3.3.1 Effects of a laser spot size with weaving system

Laser-irradiating conditions of a laser spot size, laser power density and laser spot weaving were investigated on molten-pool formation and weld-bead creation. Three laser spot sizes of 10 mm × 26 mm, 4 mm × 27 mm and 2 mm × 27 mm were applied by changing the optical-lens and fiber-cable combination to investigate the effects of the laser power density and laser spot width. The weaving-irradiating method was also applied with a narrow laser spot of 4 mm × 27 mm and 2 mm × 27

mm. The effects of laser-irradiating condition were obtained based on high-speed imaging during welding and cross-sectional observation.

Table 3.4 gives the welding conditions used. Oblique laser irradiation with single hot-wire feeding that had been investigated previously was used. A laser irradiating angle of 15° and a welding speed of 3.33 cm/min were fixed in all experiments. A 6-kW diode laser oscillator was used as a heat source with combined focusing and homogenizing lenses providing a long and narrow rectangular shape for the laser spot.

Table 3.4 Welding parameters.

Laser irradiation method	Stationary	Weaving	
Fiber core, mm	1.0	0.4	1.0
Homogenizer	LL2.85	LL2.35	LL2.35
Focus lens, mm	1000	400	400
Laser power, kW	6		
Laser-irradiating angle, degree	15		
Defocus, mm	0	20	20
Spot size, mm x mm	10^w x 26^l	2^w x 27^l	4^w x 27^l
Laser power density, W/mm^2	23	111	55
Weaving frequency, Hz	none	5	
Weaving waveform	none	Exponential	
Filler wire diameter, mm	1.6		
Welding speed, cm/min	3.3		
Wire feed speed, m/min	5.31		
Wire current, A	161	181	164
Wire feeding angle, degree	45		
Wire feeding position, mm	5		
Shielding gas, 10 l/min	Ar		
Pre-irradiation time, s	90		

The joint-configuration layout and apparatus for stationary laser irradiation and weaving laser irradiation is presented schematically in Fig. 3.11. The hot-wire feeding speed was adjusted to fill the groove, and the wire current was set to heat the filler wire tip to near its melting point appropriately in consideration of a heat input from direct laser irradiation under several laser power densities. Argon gas was used for shielding. A high-speed camera was used to observe the molten-pool formation and stability, and the feeding of the hot wire during welding. An image of the molten pool and hot wire was captured from the upper side of the groove. The shooting conditions of a frame rate of 50 fps and a shutter speed of 1/20000 s were used with an 810-nm band-pass filter. The image that was captured during welding

can be used to observe molten-pool formation and hot-wire feeding, and to investigate qualitatively the temperature distribution on a molten pool.

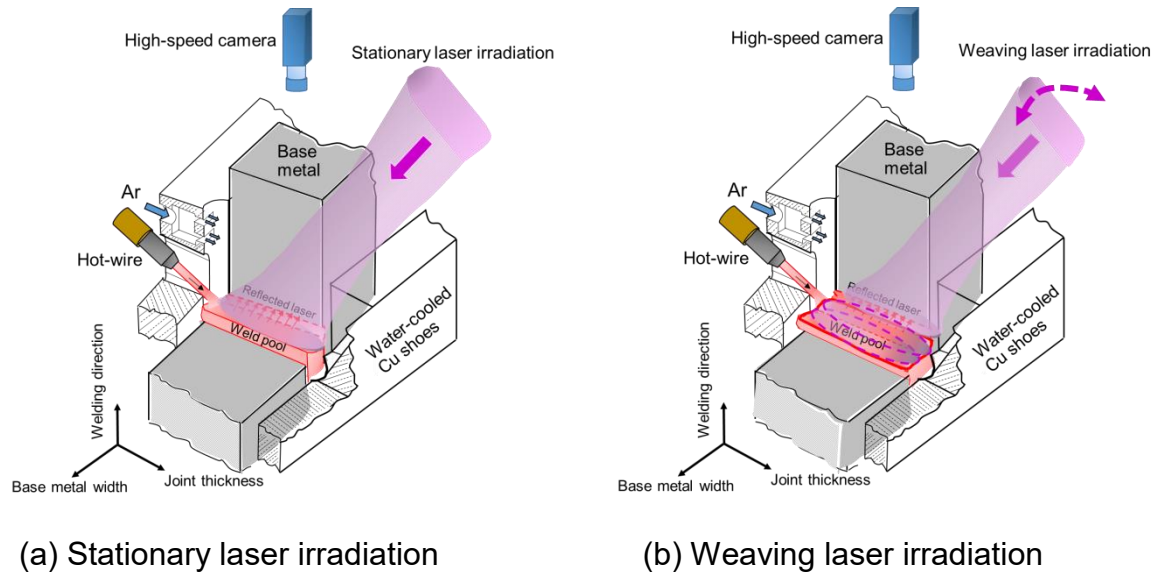(a) Stationary laser irradiation   (b) Weaving laser irradiation

Fig. 3.11 Schematic layout of joint configuration and apparatus.

Figure 3.12 shows a schematic of the laser-beam-irradiating conditions with three laser spot widths in the groove during weaving. The widest laser spot width of 10 mm with the lowest laser power density of 23 W/mm^2 was used for stationary laser irradiation to fit the groove width (gap). Narrower laser spot widths of 4 and 2 mm with the middle and highest laser power densities of 55 and 111 W/mm^2 used with a laser weaving system. The ratio between the laser beam spot width (W_L) and gap width (W_G), or the W_L/W_G ratio, was defined as a key parameter. The W_L/W_G ratio is 1.0, 0.4 and 0.2 for the 10-mm, 4-mm and 2-mm laser-beam spot width.
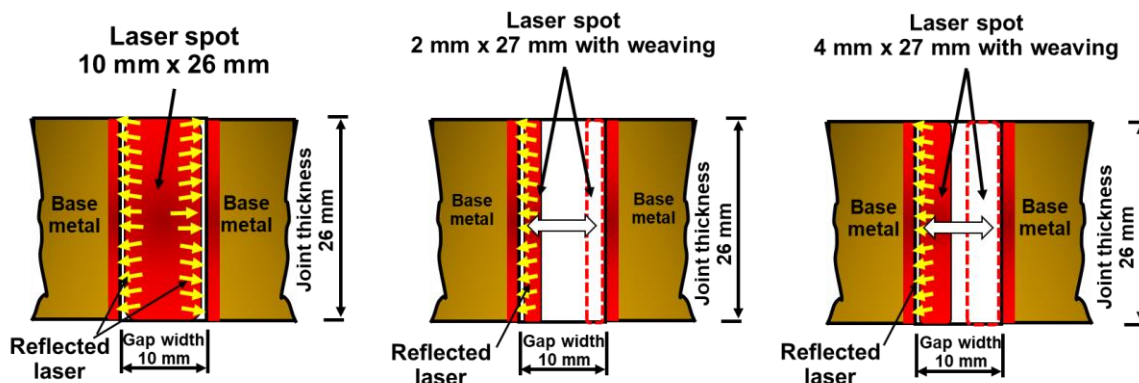
Fig. 3.12 Schematic of laser-beam shapes and laser-weaving conditions.

The weaving system can sweep the large rectangular laser spot parallel to the gap width. The weaving amplitude can be adjusted to a variable gap and the weaving frequency can also be changed. The weaving amplitude was defined to fit the 10-mm gap, and a 5-Hz weaving frequency was used. Table 3.3 shows interaction time of the laser-beam spot motion. The holding time of the laser spot near the groove surface was ~72.5 ms and the time taken to move through the opposite groove surface was only ~27.5 ms.

Figure 3.13 illustrates laser beam profiles of narrow rectangular beams used in this study. At the same laser power, the 2 mm x 27 mm laser spot has a higher-peak power density. On the other hand, the 4 mm x 27 mm laser spot has a broad power density. Figure 3.14 (a) and (b) show the schematic layout of the beam moving in the groove when the gap width was 10 mm and Δt was the moving time in 1 mm of a 5-Hz exponential waveform. In case of the laser spot width of 2 mm, the moving distance to a groove surface from the start is 4 mm with moving speed of 0.15 m/s. In case of the laser spot width of 4 mm, the moving distance is 3 mm with the moving speed of 0.11 m/s. The laser power was fixed at 6 kW in this research; thereafter the energy density can be calculated with equation (3.1) in each moving time and accumulated to summarize the energy distribution on the groove.

Fig. 3.13 Laser beam profile.
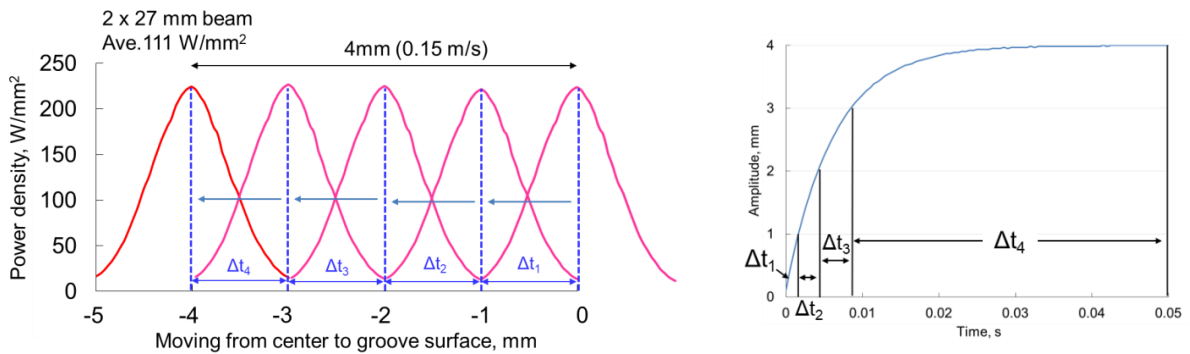
(a) 2 mm beam width.
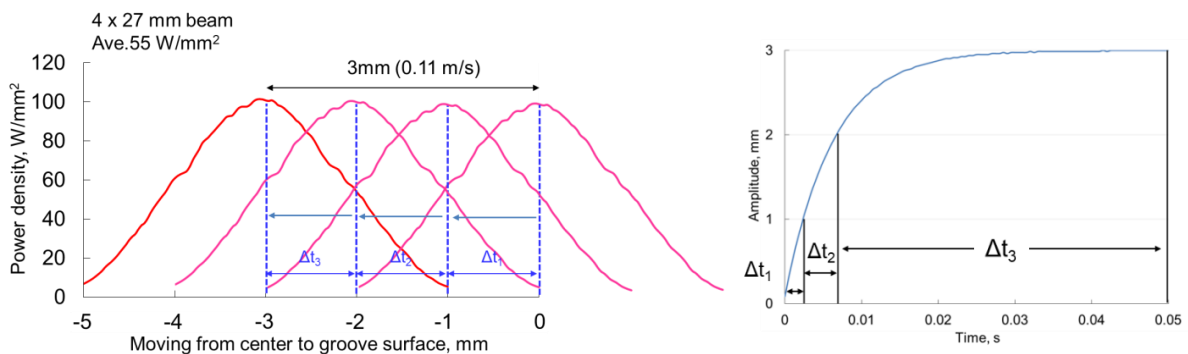
(b) 4 mm beam width.

Fig.3.14 Schematic illustration of moving motion and power distribution.

Figure 3.15 indicates the laser energy distributions of three laser spot widths in the groove with a 10-mm gap. These distributions were calculated in one cycle of a 5-Hz exponential waveform. A previous report [83] showed that the critical laser power density to melt the groove surface (base metal) was 35 W/mm^2 (7 J/mm^2 in 1 cycle of 5 Hz) for the same welding speed of 3.3 cm/min by using the stationary laser irradiation. From the results, it can be presumed that the weaving laser irradiation by using the long-length and narrow-width laser beam maintains a higher power density than the critical value for the groove surface (base metal) melting, whereas stationary laser irradiation using a long-length wide-width laser beam does not maintain the power density above the critical value.
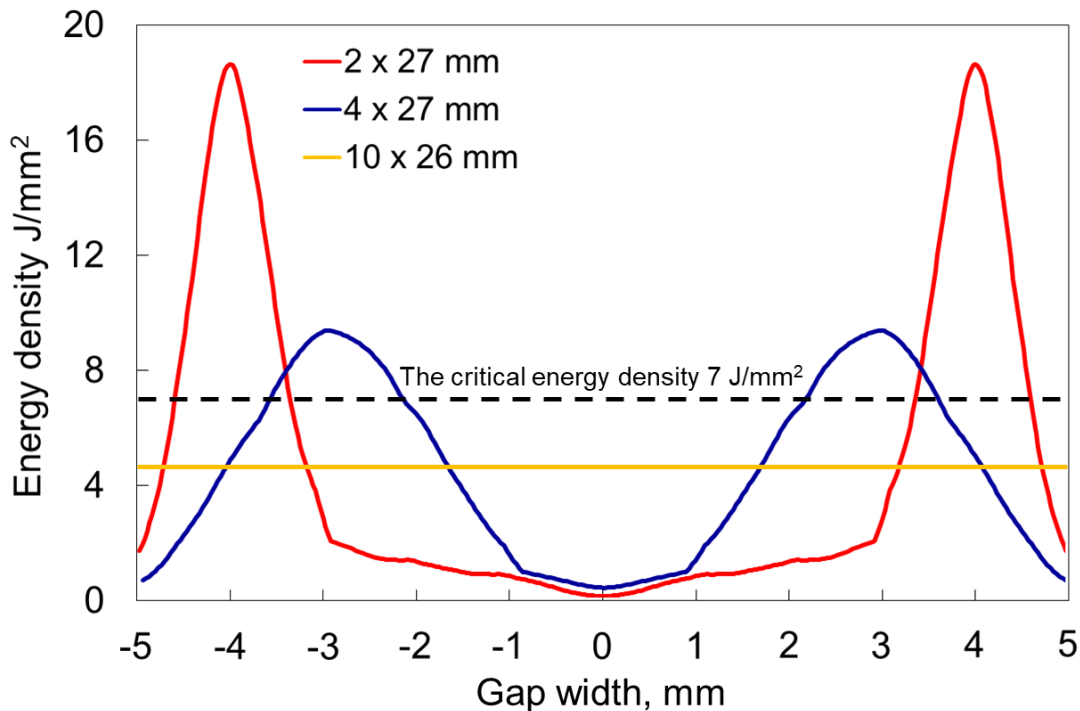
Fig. 3.15 Energy distribution on the groove of a weaving beam in one cycle of a 5-Hz exponential waveform and a stationary beam.

3.3.1.1 Molten-pool temperature distribution during welding and cross-sections

Figure 3.17 shows the contour image of the relative radiative intensity on a molten-pool surface transformed from the high-speed image in Fig. 3.16. The grayscale image that was captured thorough the 810-nm band-pass filter with an 8-bit color depth was converted to a color relative-intensity image. The small relative intensity in blue means a lower temperature on the molten pool because of the low heat input from laser irradiation. The large relative intensity in red means a higher temperature because of the high heat input from laser irradiation.

For all laser-irradiation conditions, the intensity at the edge regions of the laser and wire sides on the molten pool is lower than that at the center. Therefore, the lower temperature at the edge regions on the molten pool induces a high probability

of a lack of fusion compared with the center region. A higher intensity near both grooves (base metal) was observed when weaving irradiation was applied with a narrow 2- and 4-mm laser-spot width compared with stationary irradiation without weaving by using the wider laser-spot width of 10 mm. This high intensity means that a high temperature was created by the higher laser power density of 55 W/mm^2 for the 4-mm width and 111 W/mm^2 for the 2-mm width compared with 23 W/mm^2 for the 10-mm width of the laser spot. The weaving irradiation with an exponential waveform and a long holding time at the groove boundary of 72.5 ms in the 5-Hz frequency as Table 3.3 created a higher temperature near both grooves (base metal) and encouraged base-metal fusion. Although a high intensity along the groove (base metal) is visible at the laser-irradiating side when the narrowest laser spot width of 2 mm with the highest power density was applied, the relatively lower intensity is visible at the opposite groove side and center region on the molten pool. It can be presumed that too narrow a laser-spot width, compared with the groove width (gap) does not maintain an adequate molten-pool temperature over the entire area in the gap during weaving because this narrow laser spot provides heat input only in the limited narrow region. Therefore, the temperature near one groove side, where the laser does not irradiate, drops rapidly during laser-spot irradiation at the opposite groove side. These results imply that a laser power density and relative laser spot width to groove width (gap) of 10 mm, or the W_L/W_G ratio, would affect molten-pool formation and base-metal melting during welding.

Stationary	Weaving 5 Hz-exponential wave	
$10^w \times 26^l$ mm	$2^w \times 27^l$ mm	$4^w \times 27^l$ mm
Power density, W/mm^2 (W_L/W_G ratio)		
23 (1.0)	111 (0.2)	55 (0.4)

Fig. 3.16 High-speed images during welding for three laser-irradiating conditions.
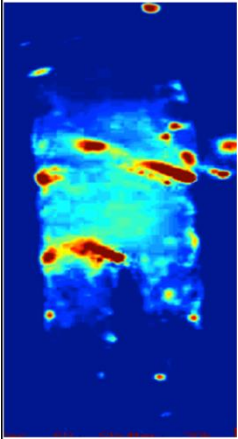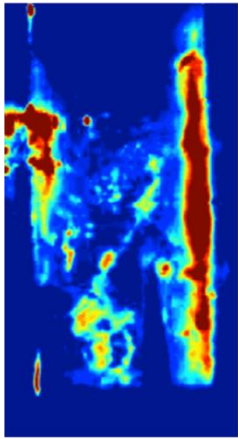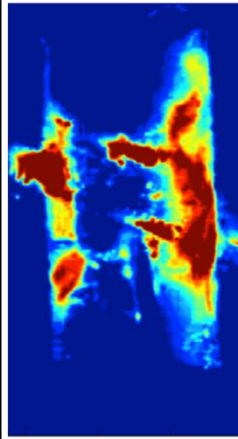
Stationary	Weaving 5 Hz-exponential wave	
$10^w \times 26^l$ mm	$2^w \times 27^l$ mm	$4^w \times 27^l$ mm
Power density, W/mm^2 (W_L/W_G ratio)		
23 (1.0)	111 (0.2)	55 (0.4)

Fig. 3.17 Intensity distribution on molten-pool surface by high-speed image captured during welding.

Figure 3.18 shows macro-cross-sections of welded for three laser-irradiating conditions. Sufficient weld metal at the edge of the wire-feeding side and insufficient weld metal at the edge of the laser-irradiating side result for all three conditions. The oblique laser-irradiating condition could not provide sufficient heat input at the edge on the laser-irradiating side in the groove and could not create sufficient temperature as shown in Figs. 3.16 and 3.17. This inadequate temperature condition resulted in insufficient base-metal melting and weld-metal creation in this region.

The lowest power density of 23 W/mm^2 in the stationary laser-irradiating condition using the widest laser spot of 10 mm $\times$ 26 mm did not provide sufficient heat input to the groove surfaces and the temperature was not elevated sufficiently as shown in Fig. 3.17. Therefore, a large lack of fusion (LOF) of 45% was generated at the laser-irradiating side and wire-feeding side.

For two weaving laser-irradiating conditions, the lower power-density condition of 55 W/mm^2 with the wider laser spot of 4 mm $\times$ 27 mm creates a larger melting area and base-metal penetration compared with those under the higher power-density condition of 111 W/mm^2 using the narrower laser spot of 2 mm $\times$ 27 mm. The laser irradiation using the laser power density of 111 W/mm^2 with the spot size of 2 mm $\times$ 27 mm and a W_L/W_G ratio of 0.2 yields a stable and consistent small melting depth on the entire length without the edge at the laser-irradiating side. The average bead width of the laser-irradiating condition is 10.9 mm, but the LOF of 13% is generated on the edge at the laser-irradiating side. The laser-irradiating condition using the laser power density of 55 W/mm^2 with a spot size of 4 mm $\times$ 27 mm and a W_L/W_G of 0.4 yields a larger melting region than that of the aforementioned cases. The average bead width was 11.9 mm, but the very small LOF of 1% still occurred with on the edge at the laser-irradiating side.

The spot size of 2 mm $\times$ 27 mm provided a much higher laser power density of 111 W/mm^2 than the critical value of 35 W/mm^2, which achieved stable fusion of the groove surface (base metal), whereas the small W_L/W_G ratio of 0.2 did not maintain the molten-pool temperature stable over the entire area and contribute to heat-conduction fusion of the groove surface (base metal). Therefore, the laser irradiating condition with the 2 mm $\times$ 27-mm spot size created a uniform and small fusion area through the plate thickness. The spot size of 4 mm $\times$ 27 mm provided a higher laser power density of 55 W/mm^2 than the critical value of 35 W/mm^2, and the large W_L/W_G ratio of 0.4 kept the molten-pool temperature over the entire area stable to contribute heat-conduction fusion of the groove surface (base metal). As a result, the laser-irradiating condition with the 4 mm $\times$ 27-mm spot size produced a large melting area especially on the center region in the thickness direction.

The above result indicates that the laser power density and W_L/W_G ratio affect the groove surface melting. A laser power density above the critical value of 35 W/mm^2 is required to achieve stable melting of the groove surface and to avoid defect formation. An adequate W_L/W_G ratio, which is 0.4 in this research, contributes to a more efficient and stable creation of groove surface fusion by maintaining a uniform and sufficient molten-pool temperature.

Stationary	Weaving (5-Hz exponential)	
$10^w \times 26^l$ mm	$2^w \times 27^l$ mm	$4^w \times 27^l$ mm
Wire Side	Cross section	10mm
Laser Side	Lack of fusion ratio,%	
45	13	1
Average bead width, mm		
9.5	10.9	11.9

Fig. 3.18 Macro cross-sections of welded specimens in various beam widths.

3.3.2 High-edged energy density of the rectangular laser beam

In the former investigations, when the uniform rectangular laser beam was used, the imperfection occurred on the edges of both groove sides as shown in Fig. 3.19. It was the result of the low power density on the uniform beam edges. In order to improve this problem and to optimize laser power density, the rectangular laser beam with high energy at edges was applied. The laser beam is created by a special

optic lens of LL2.35-edge irradiates the concentrated laser power at both edges of the laser beam where lack of fusion can occur easily. Figure 3.20 shows the beam profile and power density of the beam at 6-kW laser power. The rectangular beam of 26-mm length and 4-mm width (just focus) was made by a 1-mm fiber core, 100-mm collimator lens and 400-mm focus lens. The beam has higher power energy on groove edges and it can be assumed that this beam profile can reduced the lack of fusion on edges.
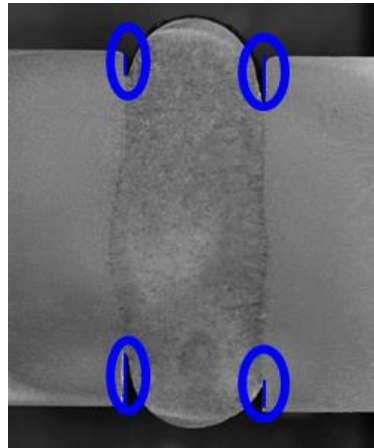
At edges lack of fusion
can occur easily

Fig. 3.19 An example of the lack of fusion on the edges of the weld joint.

Total power: 6 ,000 W

Fig. 3.20 Laser beam profile of high-edged energy type and its power energy.
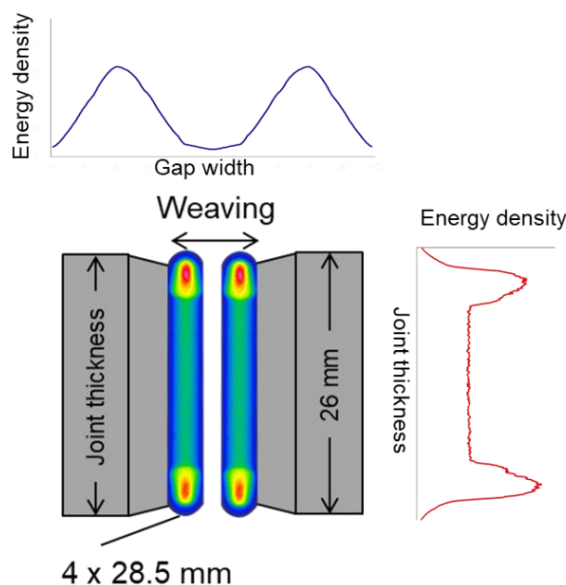
Fig. 3.21 Schematic layout of a weaving laser beam and energy density distribution.

3.3.2.1 Effects of high-edged energy density of the rectangular laser beam

The methodology and joint configuration of this study are shown in the schematic layout of single-pass vertical welding in F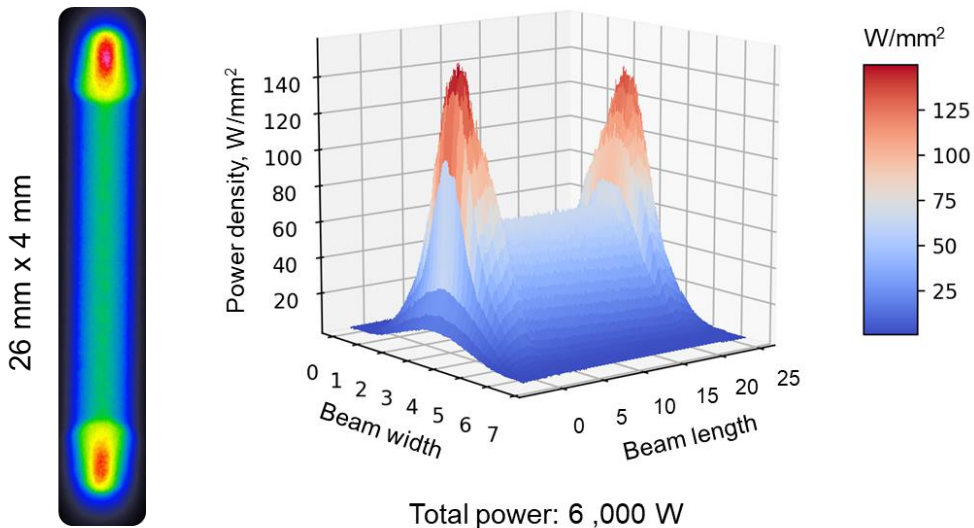ig. 3.11(b). The oblique laser irradiation with tilt angle of 15^0 and single hot-wire feeding was used. Because in the application of large size specimen the laser head could not access on the top of groove, the oblique laser was employed instead of the perpendicular laser irradiation.

Table 3.5 shows the welding conditions used in this study. The continuous wave (CW) of diode laser with laser power of 6 kW and welding speed of 3.3 cm/min were fixed in this experiment. The laser head of 1-mm fiber core was assembled with a collimator lens of 100 mm, a focus lens of 400 mm and a homogenizer.

Two homogenizers were used in this experiment such as LL2.35 and LL2.35-edge. Both of them could create the same dimension of the rectangular laser beam, but the LL2.35-edge homogenizer, which is the special optic lens, could concentrate high energy density on laser beam edges.

For the 10-mm gap, the rectangular laser spot size had a length of 28.5 mm and a width of 4 mm at 20-mm defocus. The laser spot length fitted thickness of base metal. Although the laser spot width was narrower than the gap, the weaving laser irradiation of 5-Hz exponential waveform was applied to distribute the laser power density sufficiently and keep high heating on groove walls. Figure 3.21 shows the schematic layout of a weaving laser beam with high-edged energy and the energy distribution on the groove. Only one beam can concentrate energy density in the edges and groove surfaces where the melting region is need.

Table 3.5 Welding parameters.

Gap width size, mm	10
Laser type	Diode laser
Fiber core, mm	1.0
Homogenizer	LL2.35, LL2.35-edge
Focus lens, mm	400
Laser power, kW	6
Laser irradiation angle, degree	15°
Defocus, mm	20
Spot size, mm x mm	4^w x 27^l, 4^w x 28.5^l
Laser distribution type	Uniform energy, High energy on edges
Weaving frequency, Hz	5
Weaving waveform	Exponential waveform
Filler wire diameter, mm	1.6
Welding speed, cm/min	5
Wire feed speed, m/min	7.6
Wire current, A	213
Wire feeding angle, degree	45
Wire feeding position, mm	4
Shielding gas, 10 l/min	Ar
Pre-irradiation time, s	90

Figure 3.22 shows macro cross-sections of two laser rectangular beam distribution types that identify %lack of fusion ration, %dilution ratio, penetration area, and HAZ width. When the uniform energy density in the rectangular beam was used, it was considered that the temperature at the corner of the laser beam was relatively less than the inside of that. Therefore, un-melted groove surface could occur easily and became the lack of fusion (remarked in the red line). When the high energy density at edges in the rectangular beam was used, it was found the decrease in lack of fusion, higher dilution ratio and more penetration than uniform energy density. It is as the result in improving the complete welded joint and that reduces laser power consumption. Consequently, the beam having the high-edged type and weaving system could optimal power distribution on the groove area.

Uniform energy density	High energy density at the rectangle laser edges
Lack of fusion ratio, %	
40.2	9.3
Dilution ratio, %	
0.8	3.9
Penetration Area, mm^2	
2.38	13.5
HAZ width, mm	
7.6	8.7
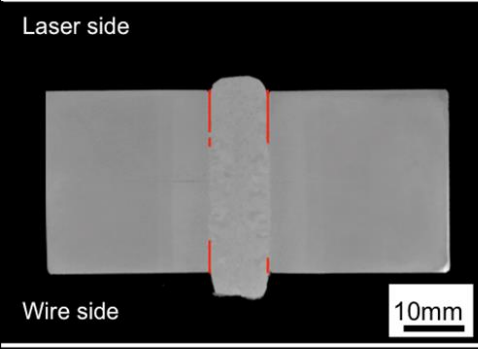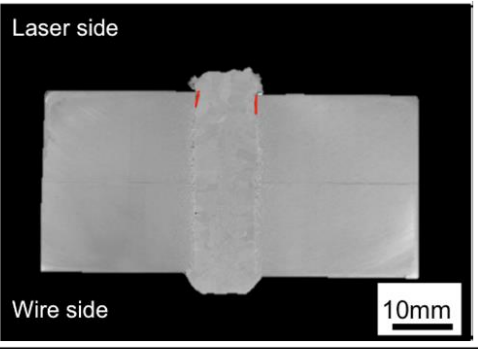
Fig. 3.22 Marco cross-section of uniform and high-edge energy density of the rectangular laser beam.

3.4 Effects of oxygen additions to the argon shielding gas

In past decades, a number of studies investigated the influent of oxygen in weld metal in conventional arc welding processes such as GMAW and GTAW [87-90]. Oxygen additions in shielding gas play an important role as an active element in arc welding. The oxygen in the weld pool has positive effects on the weld penetration, the shape of the weld and the number of nonmetallic inclusions or the volume of acicular ferrite. In addition, the filler we used is the solid wire of GMAW. Its weld metal requires the oxygen content of 200 – 250 ppm to obtain a high absorbed energy property. Therefore, this section would like to study the effects of oxygen added to argon shielding gas in the proposed welding process.

Table 3.6 Welding parameters.

Gap width size, mm	10
Laser type	Diode laser
Fiber core, mm	1.0
Homogenizer	LL2.35-edge
Focus lens, mm	400
Laser power, kW	6
Laser irradiation angle, degree	15°
Defocus, mm	20
Spot size, mm x mm	4^w x 28.5^l
Laser distribution type	High energy on edges
Weaving frequency, Hz	5
Weaving waveform	Exponential waveform
Filler wire diameter, mm	1.6
Welding speed, cm/min	3.3
Wire feed speed, m/min	5.5
Wire current, A	163
Wire feeding angle, degree	45
Wire feeding position, mm	4
Shielding gas, 10 l/min	Ar, Ar+5%O_2, Ar+10%O_2, Ar+20%O_2
Pre-irradiation time, s	90

Table 3.6 shows the welding conditions used. The continuous wave (CW) of diode laser with laser power of 6 kW and welding speed 3.3 cm/min were fixed in this experiment. The laser head of 1-mm fiber core was assembled with a collimator lens of 100 mm, focus lens of 400 mm and homogenizer of LL2.35-edges to create 4x28.5 mm rectangular laser beam at defocus 20 mm. 5 Hz exponential waveform was used. In this experiment, the shielding gas was varied an amount of oxygen as 5%, 10%, and 20% to study effects of oxygen content on welds compared with pure argon shielding gas.

Figure 3.23 shows oxygen content in the weld metal of the proposed welding process. It finds that the oxygen added in argon shielding gas can be added in the weld once an amount of oxygen in argon shielding gas rises to 5%. However, the oxygen content does not significantly change when oxygen added in argon shielding gas increases from 5%O_2 to 20%O_2. The proposed welding process is not similar to arc welding process. The oxygen cannot be added in the molten pool by an effect of arc mechanism and the shielding gas is mainly used for protecting molten pool. Since oxygen is an active element, oxygen additions to argon shielding gas affect the surface tension and further change the Marangoni convection direction in the

molten pool that may result in the welding dilution in this welding process. Figure 3.24 shows the cross-sections when the ratio of O_2 in the Ar shielding gas changes. In case of the pure Ar shielding gas, the lack of fusion is largely generated at groove surface of wire feeding side, but when the ratio of O_2 in the shielding gas increases, especially it is up to be 10% and 20%, the cross sections showed higher dilution ratio and the imperfections greatly reduces. However, oxygen generates the oxide film on the weld pool surface and a large number of added oxygen could generate heavy oxide layer. Thus, the oxygen added in argon shielding gas should be optimized.
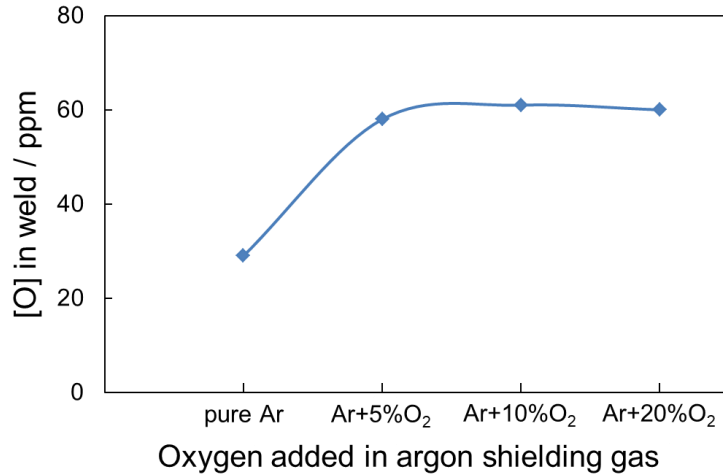
Fig.3.23 Oxygen content in weld metal of mixed shielding gas.

Ar	Ar+5%O_2	Ar+10%O_2	Ar+20%O_2
Lack of fusion, %			
23.2	14.8	0	0.54
Dilution ratio, %			
15.98	12.8	16.04	18.1
Penetration Area, mm^2			
63.96	55.69	64.15	74.9
HAZ width, mm			
11.3	10.8	11.5	11.8
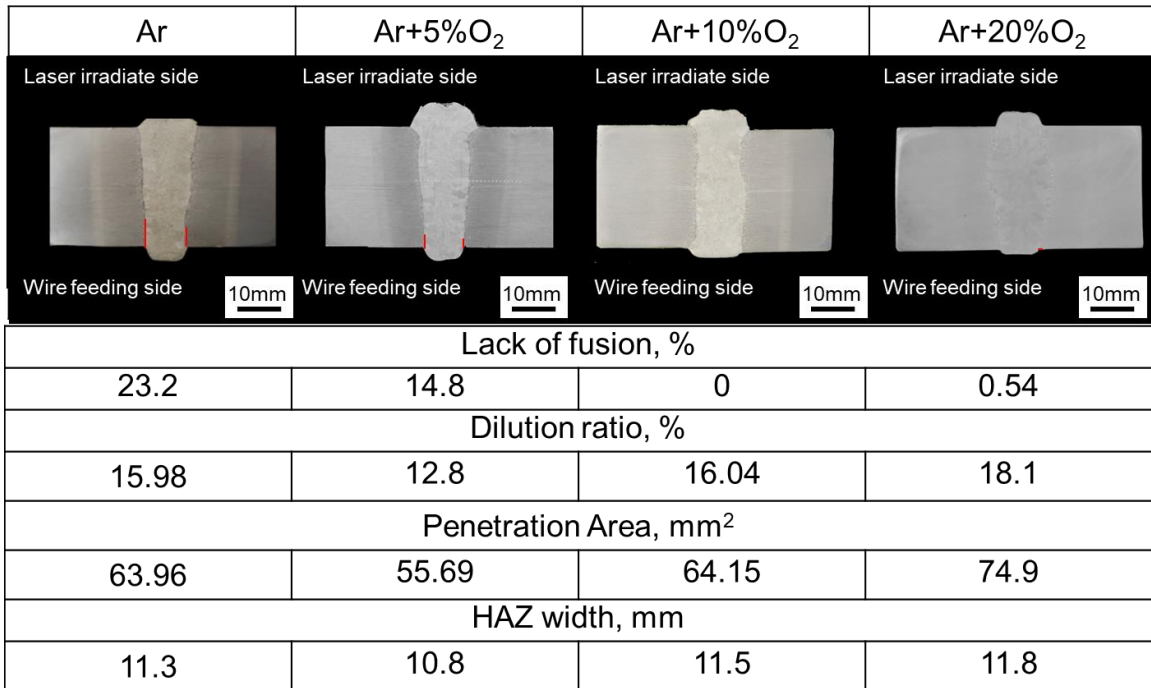
Fig. 3.24 Macro cross-sections of mixed shielding gas.

Figure 3.25 shows the Vicker hardness test results through the weld metal, HAZ and base metal at the thickness center when pure Ar, Ar+5%O_2, Ar+10%O_2, and Ar+20%O_2 were used as a shielding gas. All the weld joints have no significant difference in hardness distribution. The weld metal obtains high mean hardness value about 300 HV that is much higher than the base metal hardness of 200 HV on account of the different material strength between the filler wire and the base metal. It also shows the softening degree in HAZ.

Fig. 3.25 Hardness distribution on weld metal and HAZ.

Fig. 3.26 Microstructure of weld metal.

Figure 3.26 shows the microstructure of weld metal in each shielding gas. The weld metal of pure Ar shielding gas reveals upper bainite structure and the microstructure of Ar+5%O_2, Ar+10%O_2 and Ar+20%O_2 shielding gas can be confirmed that an increase in the amount of acicular ferrite in upper bainite structure is formed compared with the pure Ar shielding gas in accordance with raising oxygen content in weld metal.

3.5 Summary

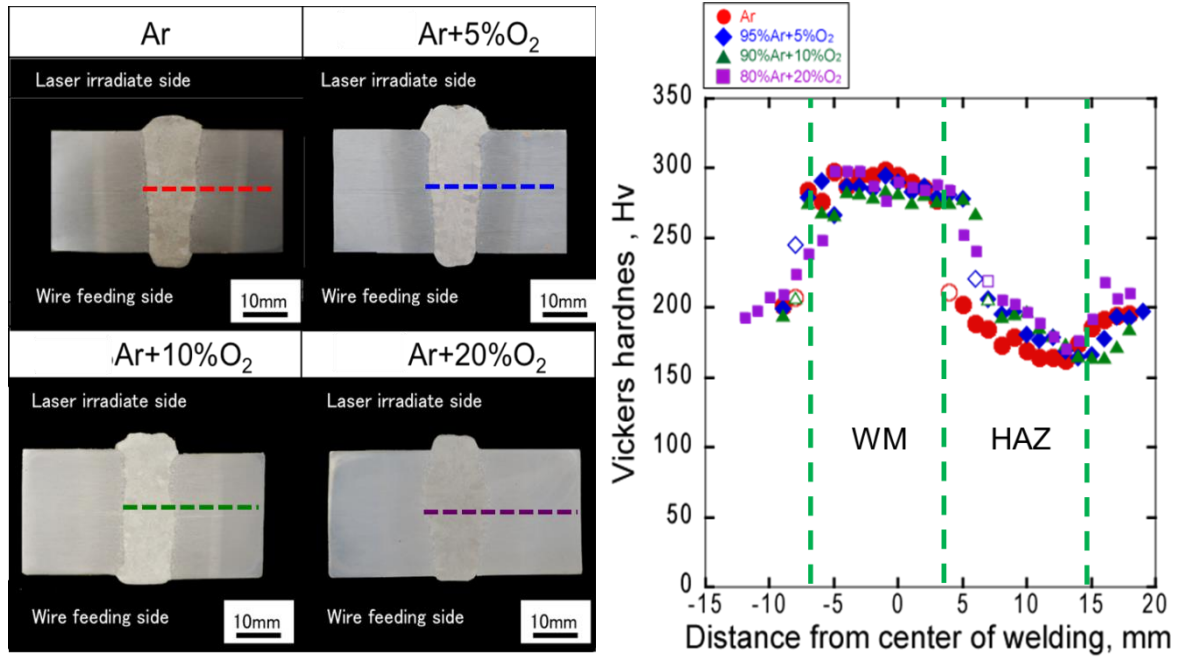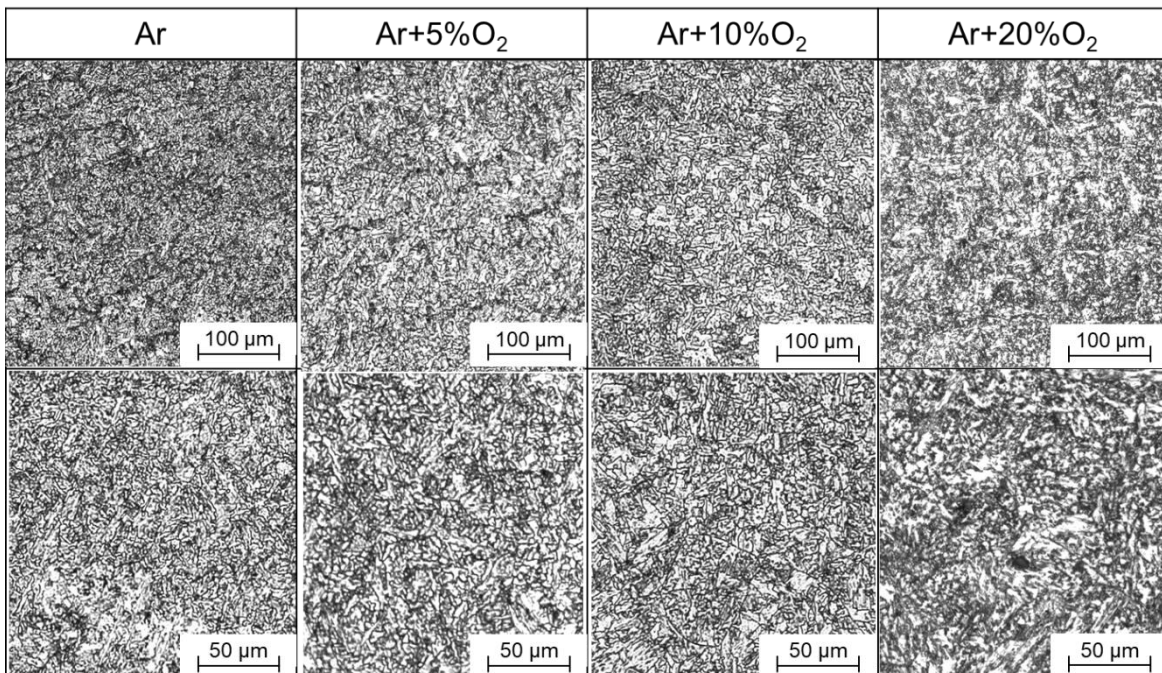In order to reduce the heat input of single-pass vertical welding joint, the hot-wire laser welding method was investigated to replace high heat input of a conventional arc welding process. Moreover, the proposed process could optimize power density distribution to reduce laser power and it achieved a sound joint and steady welding phenomenon. The optimal conditions can be drawn as follows:

1) A diode laser beam irradiated a controllable rectangular beam to optimize power density distribution on the groove combined with a hot-wire system. The narrow beam having high power density with a weaving system played an important role in optimizing laser power to keep the molten pool and to melt the base metal.

2) The spot size of 2 x 27 mm and a W_L / W_G ratio of 0.2 and the spot size of 4 x 27 mm and a W_L / W_G ratio of 0.4 with a 5-Hz exponential waveform having different power density were studied. The sound W_L / W_G ratio, which was 0.4 in this research, achieved the largest base-metal fusion area because it maintained an adequate uniform and stable temperature of the molten pool. The small W_L / W_G ratio, which was 0.2 in this research, maintained a smaller fusion area because it produced a sudden temperature drop and temperature fluctuation of the molten pool with laser spot weaving.

3) High-edged energy beam type made by a particular optic lens could concentrate more power on the beam edges which increased dilution and reduced lack of fusion on the groove edges. Therefore, the combination of a weaving system and high-edge energy type was an optimal condition for one beam.

4) Furthermore, mixed shielding gases were studied by adding 5%, 10% and 20% oxygen into Argon shielding gas. In this experiment increasing oxygen had a positive effect on higher penetration and decreasing lack of fusion. However, it could generate an oxide film on the weld pool or some slag between the copper shoe and the weld bead. An amount of oxygen, therefore, should be optimized.

Chapter 4

Optimal parameters of the novel welding process in application of the large size specimen

4.1 Introduction

In the aforementioned investigations in the Chapter 3, laser irradiation with a weaving system and oxygen-added Ar shielding gas were optimized to achieve a sound joint. In the practical shipbuilding field, however, vertical welding must be applied in the extremely large-size and heavy-thick plate. Therefore, in this part, the proposed process used for the large size jig is developed and investigated the welding phenomena and mechanical properties of the welded joint.

In the first part, the development of the hot-wire laser system, the welding configuration for large size jig used for a long-weld specimen similar to EGW in order to do the trial large in a practical use are presented. Then the obtained optimal welding conditions as investigated in the first part are applied to analyze the effects of the proposed welding process on long weld length as same as in the actual field welding compared with a EGW weld joint.

In the second part, the weld joint properties of the novel welding process of large size specimen performed in the above part such as weld bead appearance, macro cross-section, hardness distribution, microstructure, tensile test, and fracture toughness test are evaluated in accordance with the standard requirement.

Accordance to a limited diode laser of 6 kW, an adequate laser power density with the 10-mm gap width is only up to 28.5-mm thickness. However, the actual thickness of this structure is more than 50 mm. Consequently, in the Chapter 5, twin diode lasers employed for heavy-thick steel plate are discussed.

4.2 Introduction of the joint configuration and equipment of the novel welding process in the large size jig
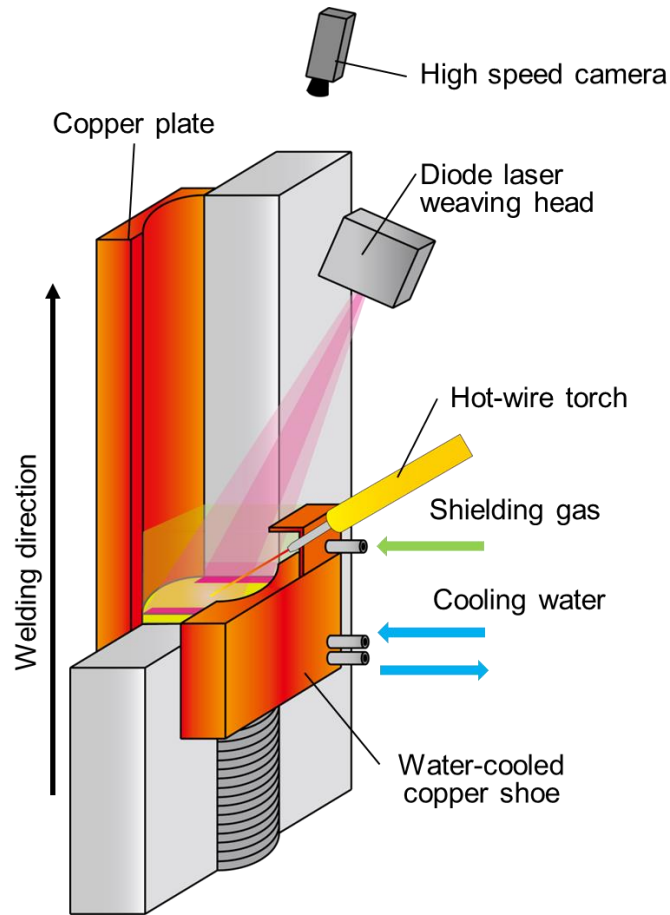
Fig 4.1 Schematic layout of the large size jig of the proposed process.

For single-pass vertical welding with a long-welded joint in a practical use of the shipbuilding, laser irradiation and hot-wire feeding can access only one side similar to EGW. Figure 4.1 presents a schematic layout of the joint configuration for a large-scale specimen. The specimen is set vertically on a copper plate making a back side groove. The obtained optimal conditions are applied to large size specimens. The hot-wire laser welding (HLW) with a self-propelled base is developed in order to trial for the long-welded joint in a practical use. The hot wire, oblique laser irradiating, a copper shoe and a high-speed camera, which access from the front side, are moved together. In this jig, the laser head angle and defocus length is fixed to create the proper laser spot size with a weaving system. Moreover, the shielding gas and cooling water are applied through the inside of the copper shoe.

4.2.1 In-situ observation

A high-speed image of the welding phenomena was captured by a high-speed camera. The camera of pencil camera V-193-M1 model connected with NAC: MEMRECAM GX-5 module with a focus lens of 35 mm with a diameter of 25 mm and an 810-nm bandpass filter as shown in Fig. 4.2. The capturing parameters are the frame rate of 50 fps, shutter speed of 1/1000 s, and closed aperture. Table 4.1 shows the monitoring condition. For setting a camera perspective to see the melting phenomena on the groove wall surfaces, it was perpendicular to groove wall surfaces and 80 degrees from the weld pool plane.
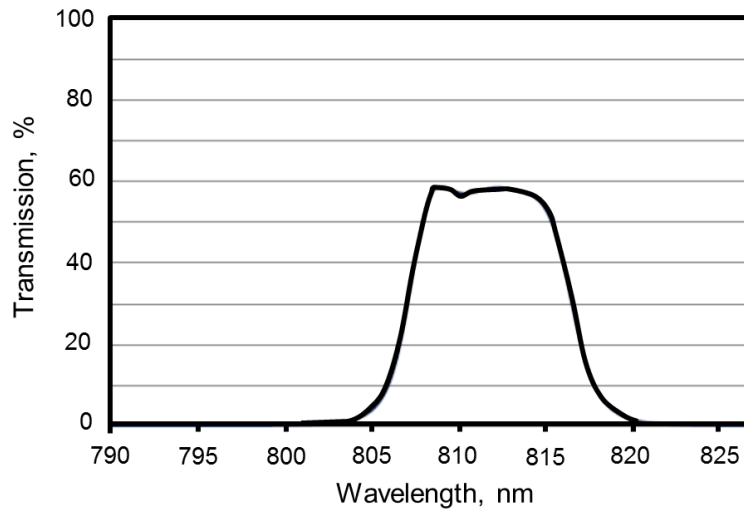

Fig 4.2 Transmission curve of 810 nm bandpass filter.

Table 4.1 Monitoring conditions of in-situ observation.

High-speed camera	GX-5
Frame rate, fps	50
Aperture	Closed
Focus lens, mm	35
Band pass filter, nm/FWHM	810 / 10
Lighting	N/A
Shutter speed, s	1/1000

4.2.2 Materials used

KE 47 steel plate, available in the ClassNK standard, was used as base metal material that thickness is reduced to 28.5 mm. There were two sizes of specimens (Medium: 250w x 500h and Large: 500w x 1300h mm) as shown in Fig. 4.3. Plates were fixed and aligned as a vertical joint configuration. The square groove was set with a 10-mm gap using a bottom spacer having dimensions of 10 (width) x 20 (height) x 28.5 mm (depth). YM-60A (JIS Z3312 G59JA1UM3M1T) with a diameter of 1.6 mm was used for hot-wire rod. The chemical compositions of base metal and filler metal are illustrated in Table 4.2.

Table 4.2 Chemical compositions of base metal and filler wire.

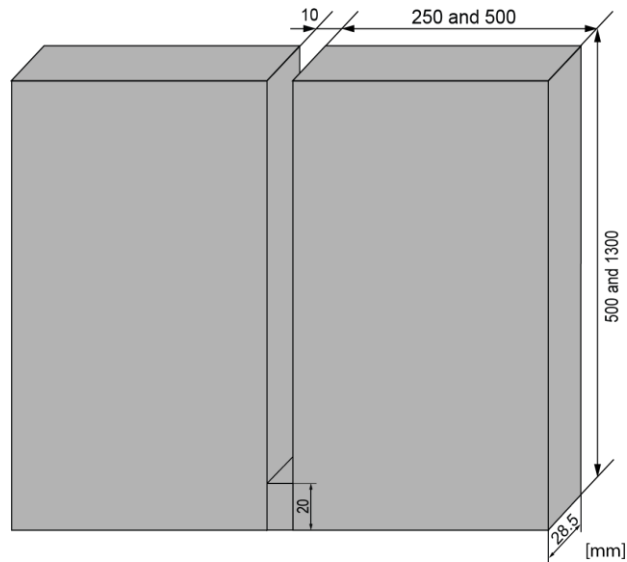| Materials	Chemical Composition, wt%											
	C	Si	Mn	P	S	Al	Cu	Ni	Nb	Ti	Cr	Mo
KE-47	0.09	0.07	1.52	0.007	0.002	0.014	0.32	0.69	0.01	0.01	0.02	0.00
YM-60A	0.06	0.35	1.45	0.010	0.007	-	0.20	-	-	0.7	-	0.38

Fig. 4.3 Specimen dimensions used for large size jig.

4.3 Welding performing of large size specimen and a weld bead appearance

Figure 4.4 shows the photograph showing vertical hot-wire laser welding during operating. The large size specimen was fit up with the 10-mm gap placed on a back-side copper plate. The self-propelled unit carried a laser head, a hot-wire torch, water-cooled copper shoe, and a high-speed camera to move together along a guide rail that is similar to EGW. The copper shoe was cooled by water flow inside to form a weld bead in front side and it supplied shielding gas to protect the weld pool. For long-welded length, it was possible to acquire high heating accumulation on hot-wire during welding and then a filler wire would be melted inside a ceramic guide. Thus, the hot-wire torch was covered by the water-cooled torch holder. The high-speed camera was used to observe weld pool phenomena on the top of the self-propelled unit and its parameter was shown in Table 4.1.
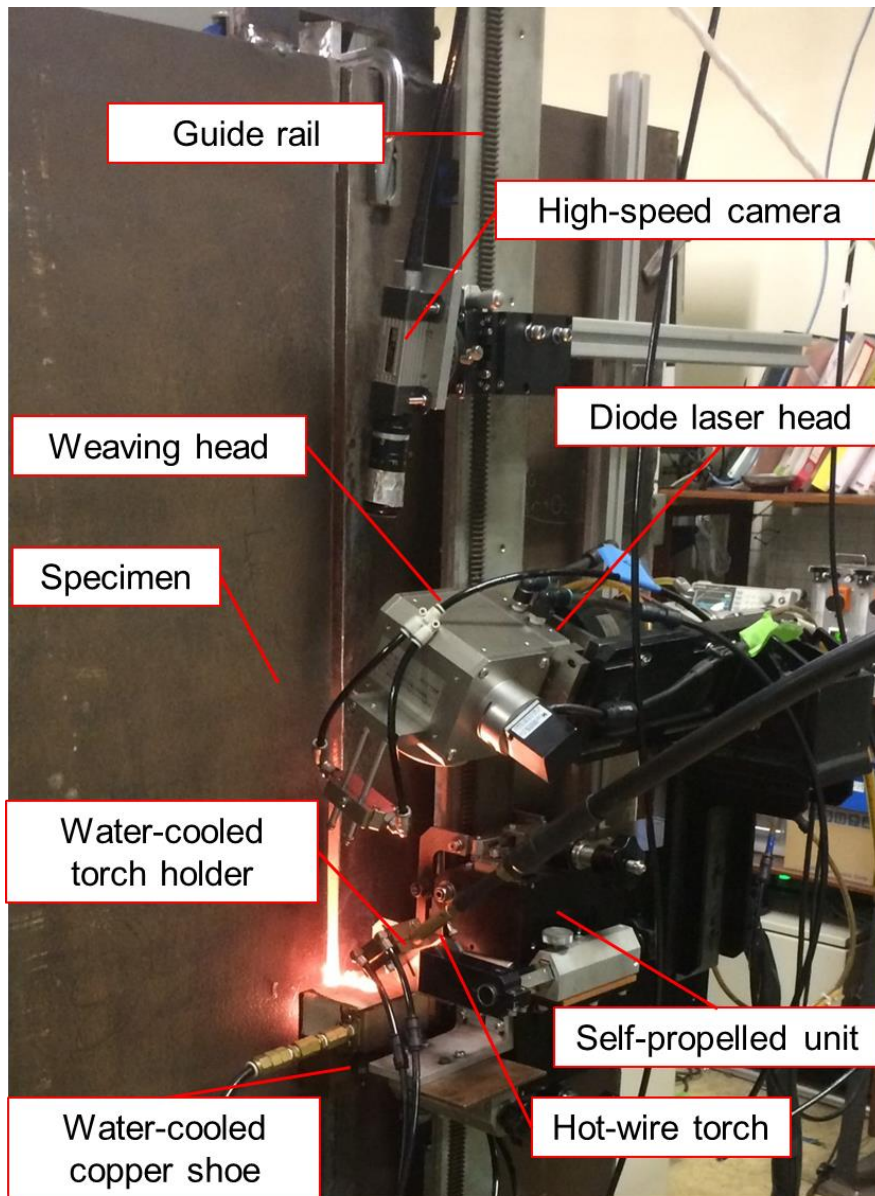

Fig. 4.4 Photograph showing the proposed welding process.

Table 4.3 gives the optimal welding conditions used for large size jig. The maximum of 6-kW laser power and mixed shielding gas of Ar+20%O_2 were used. The laser head of 1-mm fiber core was assembled with collimator lens of 100-mm, focus lens of 400 mm and LL2.35-edged homogenizer to create 4x28.5-mm rectangular laser beam at 20-mm defocus and 5-Hz exponential waveform was used. This experiment performed with two welding speeds due to the effect of large size specimen. The welding speed was varied in 2.5 and 3.3 cm/min.

Table 4.3 Welding parameters.

Gap width size, mm	10	
Laser type	Diode laser	
Fiber core, mm	1.0	
Homogenizer	LL2.35-edge	
Focus lens, mm	400	
Laser power, kW	6	
Laser irradiation angle, degree	15°	
Defocus, mm	20	
Spot size, mm x mm	4^w x 28.5^l	
Laser distribution type	High energy on edges	
Weaving frequency, Hz	5	
Weaving waveform	Exponential waveform	
Filler wire diameter, mm	1.6	
Welding speed, cm/min	2.5	3.3
Wire feed speed, m/min	5.2	5.92
Wire current, A	144	163
Wire feeding angle, degree	45	
Wire feeding position, mm	4	
Shielding gas, 10 l/min	Ar+20%O_2	
Pre-irradiation time, s	90	

In the previous study of optimizing welding conditions in a small size specimen, there was no any imperfection formed up to the surface of a welded joint which was produced with a laser power of 6 kW and a welding speed of 3.3 cm/min. As regards a large specimen of YP 47 steel, the heat of the molten pool tends to distribute more on the surface because the size of the test piece becoming larger has high conductivity, and the molten pool is cooled faster. In order to keep the molten pool, increasing an amount of heat input is needed by enlarging laser power or reducing welding speed. Electrogas arc welding (EGW), which is currently used, is able to perform the single-pass vertical welding with a welding speed of 5 cm/min. The proposed process can be competitive by an increase in laser power. However, the maximum of a laser oscillator used in the experiment is 6 kW. We decided to reduce the welding speed. Therefore, in this chapter, we changed the welding speed from 3.3 to 2.5 cm/min and fixed the 6-kW laser power. The welded joint of welding speed 2.5 cm/min was evaluated in various characteristics.
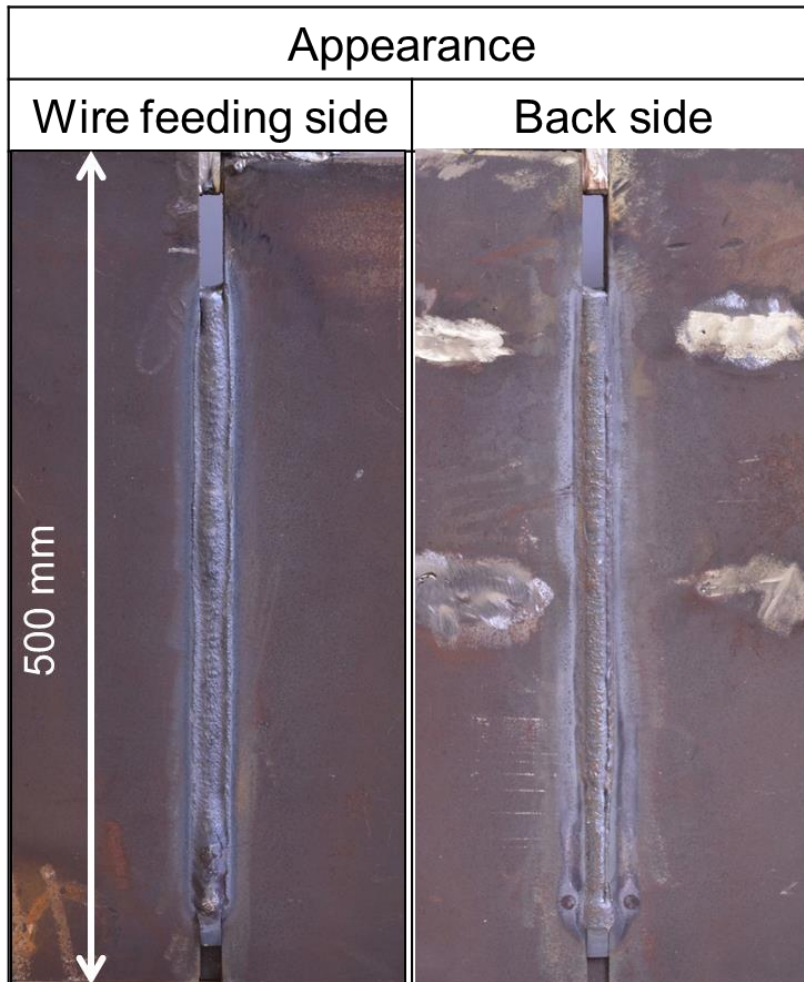

Fig. 4.5 An example of weld bead appearance of the 250^Wx500^L mm specimen with a welding speed of 2.5 cm/min.

Figure 4.5 shows the welded joint appearance of the specimen prepared with the welding speed of 2.5 cm/min using the proposed welding process. The weld bead achieves complete penetration on both the front side and back side, and it obtains a sound welded joint. There are no visible imperfections that can be observed. Because of adequate power distribution and hot-wire system, a stable welding process was achieved. The large size jig of the novel welding process could continue smoothly even though the heat source of diode laser and hot-wire feeding moved during welding.

Figure 4.6 shows the macro cross-sections of two long-welded specimens with different welding speed of 3.3 cm/min and 2.5 cm/min. Both welded joints obtain low dilution and narrow HAZ as a result of low heat input welding process. However, in 3.3 cm/min specimen a little lack of fusion on the edge was found sometimes regarding the large size specimen and during welding, an amount of heating molten pool could spread more rapidly in the large size specimen than the small size specimen. In this experiment, we tried to increase heat by reducing welding speed from 3.3 to 2.5 cm/min and a heat input also enlarged from 109 to 144 kJ/cm. The heat input was calculated by the laser power and the welding speed not including the absorption factor. The result showed that 2.5-cm/min specimen could achieve complete penetration and there were no imperfections. Consequently, the laser output is 6 kW for the large specimen with the welding speed at 2.5 cm/min. It is highly possible to produce a joint without welding defects.
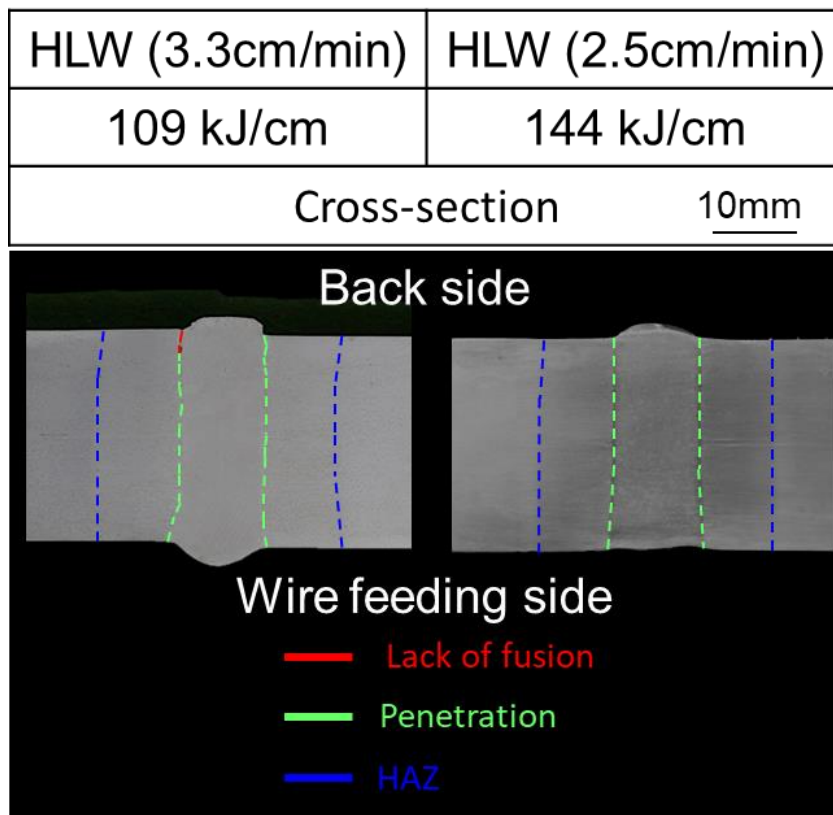

Fig. 4.6 Macro cross-sections of the 28.5^tx250^Wx500^L mm specimen produced by the large size jig using HLW.
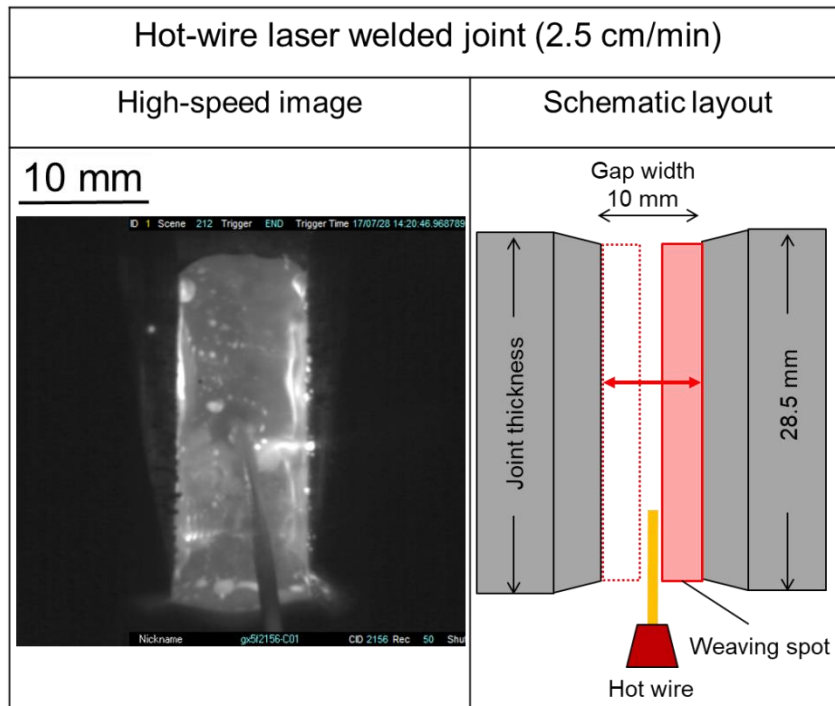
Fig 4.7 High-speed image and schematic layout of the proposed welding process during welding.

The welding phenomena during welding of the long-welded specimen with 2.5 cm/min welding speed were observed by a high-speed camera and its parameters are shown in Table 4.1. Figure 4.7 shows the schematic layout and a clear explanation of weld pool perspective compared with a high-speed image of weld pool phenomena of the proposed process during welding. The schematic layout describes a rectangular laser beam of 4^w x 28.5^L mm with a weaving system which is placed along with joint thickness moves throughout the gap width between groove surfaces. High-speed image of the large size specimen using 6-kW laser power and 2.5-cm/min welding speed with hot wire shows stable welding phenomena. The molten pool could penetrate the whole welded groove on both wire feeding side and back side continuously.

4.4 Joint properties of 1-pass vertical welding using hot-wire laser method

This part is to study the welded-joint properties of large size specimens using the proposed welding process. The long-welded joints that achieved complete penetration presented in previous part in the length of 500 mm and 1300 mm were investigated the properties such as macro/microstructure, hardness distribution, tensile test, and fracture toughness test according to the standard specification.

4.4.1 Hardness distribution

A micro Vickers hardness tester (MHT-1, manufactured by Matsuzawa Seiki Co., Ltd.) was used for the measurement. The load was 1 kgf and the holding time was 10 s in accordance with JIS Z 2244. The Vickers hardness defined in the following formula was calculated with equation (4.1) from the average value of the measured indentation diagonal length.

$$HV = 0.1892 \times \frac{F}{d^2} \tag{4.1}$$

Hereby, HV: Vickers hardness, F: load [N], d: average value [mm] of the diagonal length of the indentation.

Figure 4.8 shows the hardness distribution through the base metal, HAZ and weld metal on the middle of thickness. The result finds that the mean weld metal hardness of 226 HV is relatively higher than the base metal hardness of 206 HV due to a higher strength material and it also shows that the softening degree in HAZ is small as 188 HV and the softened width is narrow as 5 mm.
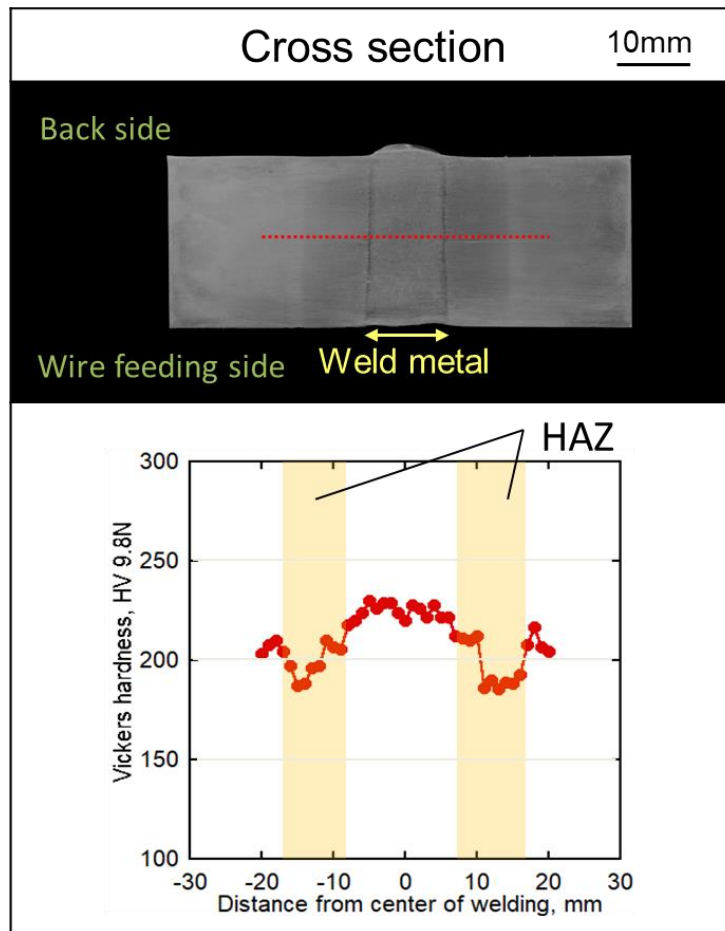

Fig. 4.8 Vickers hardness distribution in the middle of the welded joint.

4.4.2 Microstructure characteristics of the welded joint

This section is to investigate microstructure characteristics of the large size specimen that was mentioned above. 6-kW laser power and 2.5-cm/min welding speed results in heat input of 144 kJ/cm. Filler wire and base metal materials of YM-60A (JIS Z3312 G59JA1UM3M1T) and KE-47 were used respectively. The cross-section was polished firstly with various grit sizes of sandpaper number 100, 500, 1200, 2000 and 3000 in order and then polished with diamond paste with a particle size of 6, 1 μm and magnesium oxide (MgO) powder. In addition, it was etched by 3% nital solution to reveal microstructure and that was observed by optical microscopic (1LM21 lasertec)

Figure 4.9 shows the microstructure of HAZ of the welded specimen. Coarse grain heat affected zone (CGHAZ) is a part of HAZ caused by heat during welding process. Its microstructure changing in prior austenitic grain size affects toughness and properties of a welded joint. Therefore, a decrease in heat input can obtain narrow CGHAZ and improve the welded joint properties. The proposed welding process achieves the narrow CGHAZ as 0.84 mm in 28.5-mm-thick specimen as a result of the low heat input welding process.

Figure 4.10 illustrates the microstructure of weld metal and fusion boundary. The results show that fine lower bainite is generated in the weld metal. A large fraction of ferrite grain boundary and upper bainite are found in the fusion line. In addition, coarsening of crystal grain size in HAZ is observed pro-eutectoid ferrite and lower bainite.
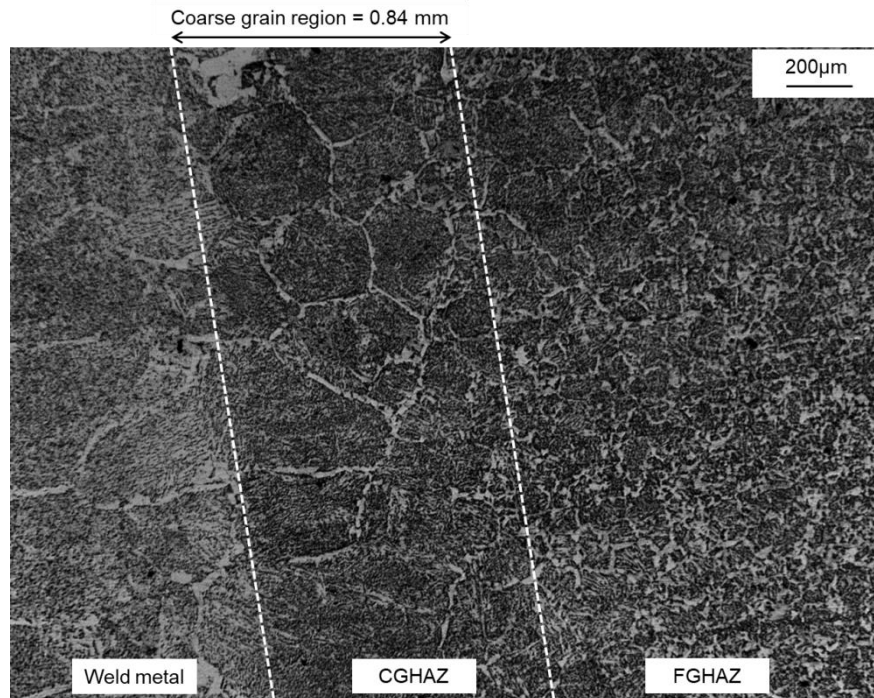

Fig. 4.9 Coarse grain heat affected zone region of large size specimen with a heat input of 144 kJ/cm (6kW, 2.5 cm/min).
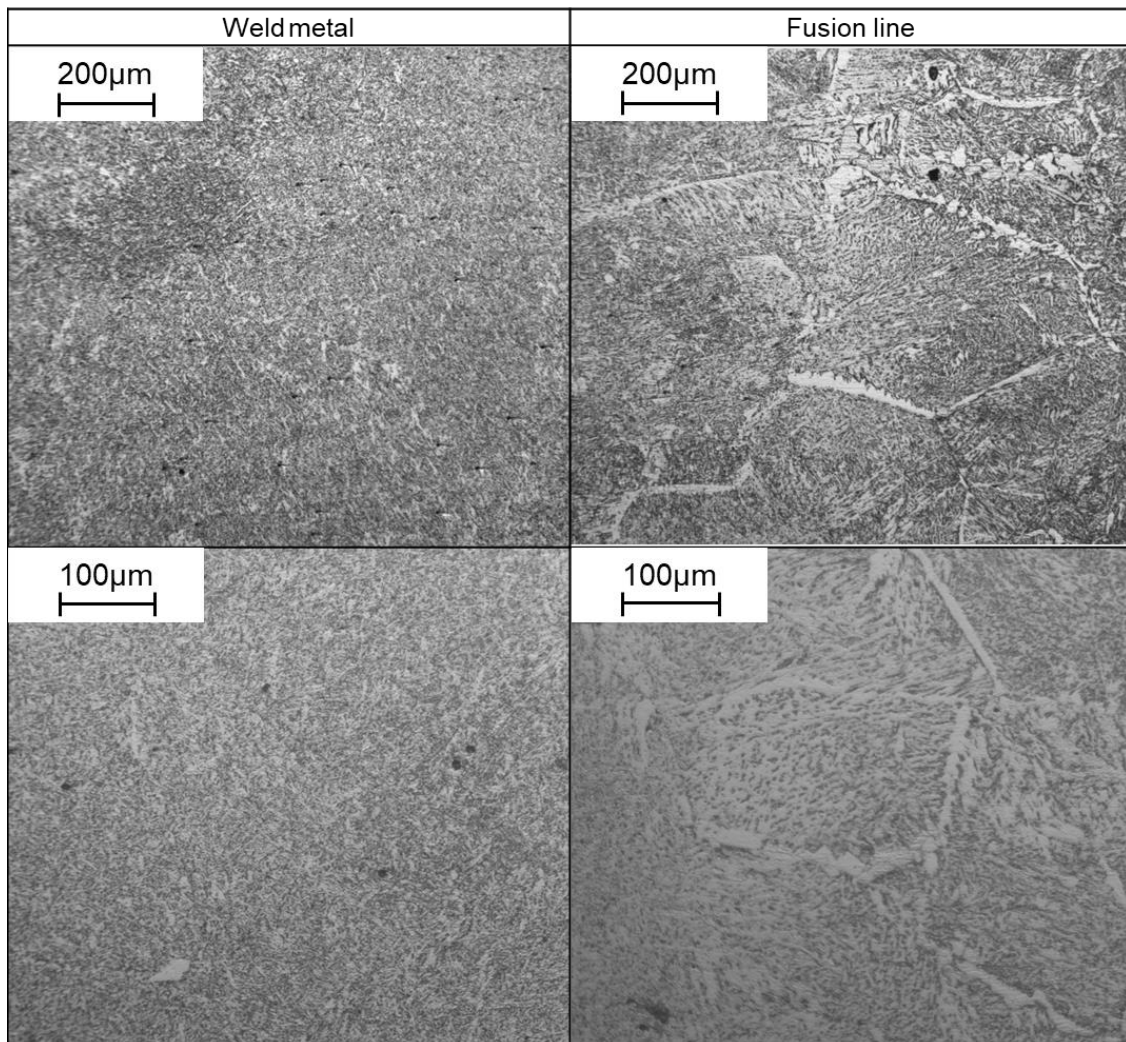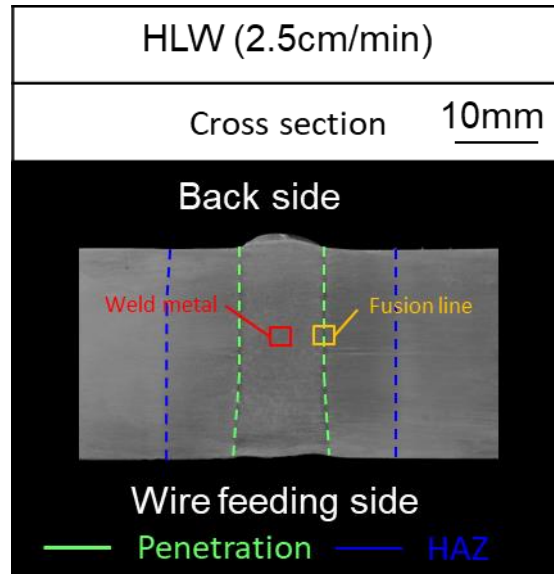
Fig 4.10 Microstructure of fusion boundary and weld metal.

4.4.2.1 Comparison of the welded joints of electrogas arc welding and hot-wire laser welding

Figure 4.11 shows the cross-sections of EGW and HLW welded joints having the same thickness. By comparison with the EGW process currently used in the field, although the welding speed of the EGW joint is 2 times higher, the HLW joint obtains extremely smaller dilution ratio, penetration area and narrower heat affected zone. In accordance with the microstructure as shown in Fig. 4.12, in the microstructure of weld metal, coarse ferrite is found, and bainite and acicular ferrite are also partly generated in the weld metal of the EGW joint. In the HLW joint, it reveals fine lower bainite. In the microstructure of HAZ, the EWG joint shows coarse grain boundary ferrite including bainite and acicular ferrite partly formed. In the HWL joint, intergranular ferrite, upper bainite and acicular ferrite are found, and it can be confirmed that the coarse grain boundary ferrite of the HLW joint is smaller than that of the EGW joint even in lower welding speed. Consequently, the HLW process which achieves an efficient welding process and the sound weld joint is relatively better than the EGW process as a result of a low heat input.

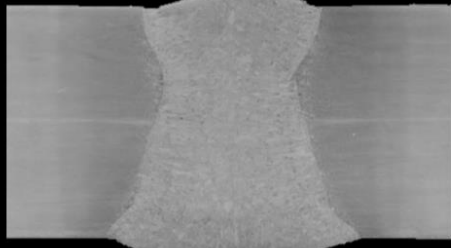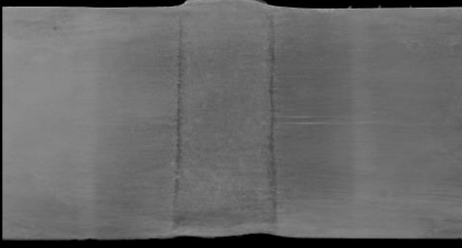| EGW (5 cm/min)	HLW (2.5 cm/min)
Cross-section	10mm
Back side	
Wire feeding side	
Dilution ratio	
21 %	12 %
Penetration Area	
144 mm^2	40 mm^2
HAZ width	
12.6 mm	9.5 mm

Fig. 4.11 Cross-sections of EGW and HLW.
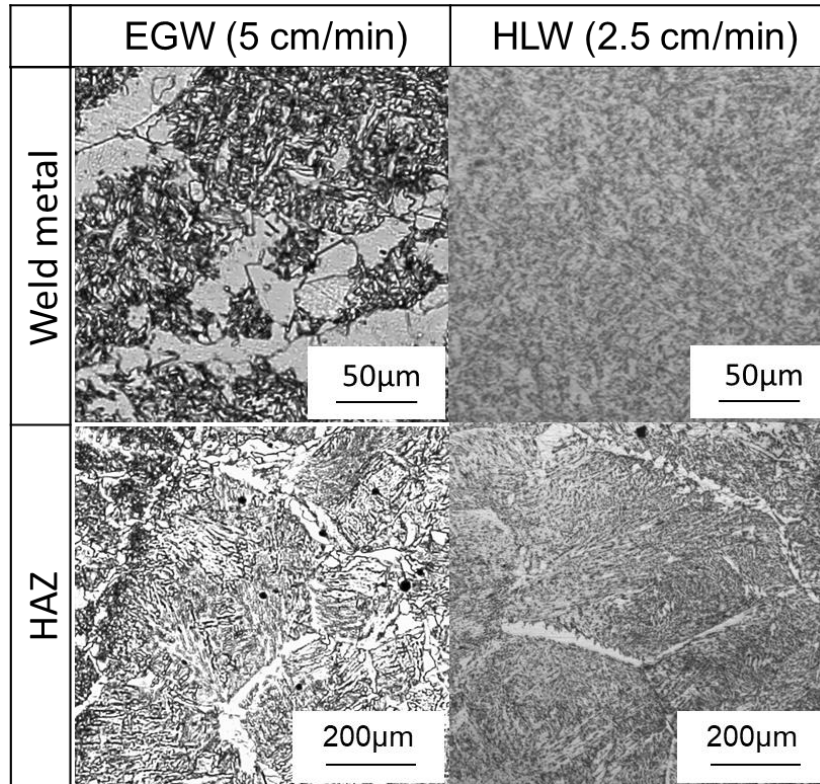
Fig. 4.12 Microstructure of weld metal and heat affected zone.

4.4.3 Tensile test of the welded joint

The large size specimen was cut to prepare a tensile specimen as shown in Fig. 4.13. The standard specimen size was made in accordance with JIS Z 2201 no.14B and the thickness became 26.9 mm after machining.

The tensile test result is shown in Fig. 4.14. Regarding the material strength of filler wire and base metal, the tensile specimen is broken in base metal and greatly elongated. The tensile strength over 570 MPa, the yield stress over 460 MPa and elongation over 17% meet the requirement of the ClassNK standard.

Specimen name	YM-60A_1.5m/h
Specimen type	JIS No.14B
Cross-sectional area, mm²	672.5
Testing rate, mm/min	2
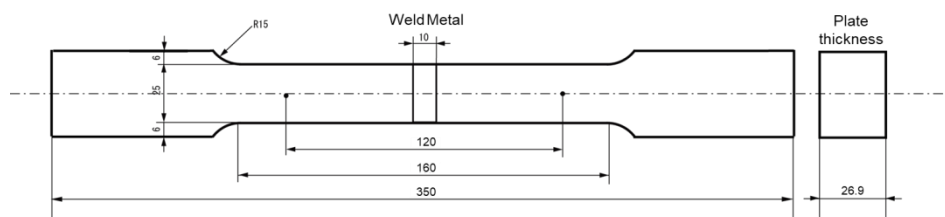
Fig. 4.13 Tensile test specimen.

Specimen name	HLW (1.5m/h)		Specification	
			Base metal	Filler wire
Thickness, mm	26.9		Base metal	Filler wire
Yield strength, MPa	461		460(min.)	490(min.)
Tensile strength, MPa	583		570-720	570-770
Elongation after fracture, %	23		17(min.)	19(min.)

Fig. 4.14 Tensile test result.

4.4.4 Charpy V-notch impact test of the welded joint

Figure 4.15 shows the cutting plan of the welded joint and notch locations. The stand specimen size for Charpy impact test is 10 mm x 10 mm x 55 mm according to JIS Z 2242. The Charpy test equipment has a heavy pendulum of 25.31kg and arm length of 0.7 m in this test.

This impact test is a method to evaluate absorbed energy of material for brittle fracture at low temperature. In this study, we varied the test temperatures to find out the ductile and brittle transition temperature (DBTT) and the notch locations were at weld metal (WM) and fusion line (FL).

Fig. 4.15 Cutting plan and notch locations.

Fig. 4.16 Absorbed energy VS test temperature at weld metal and fusion line.

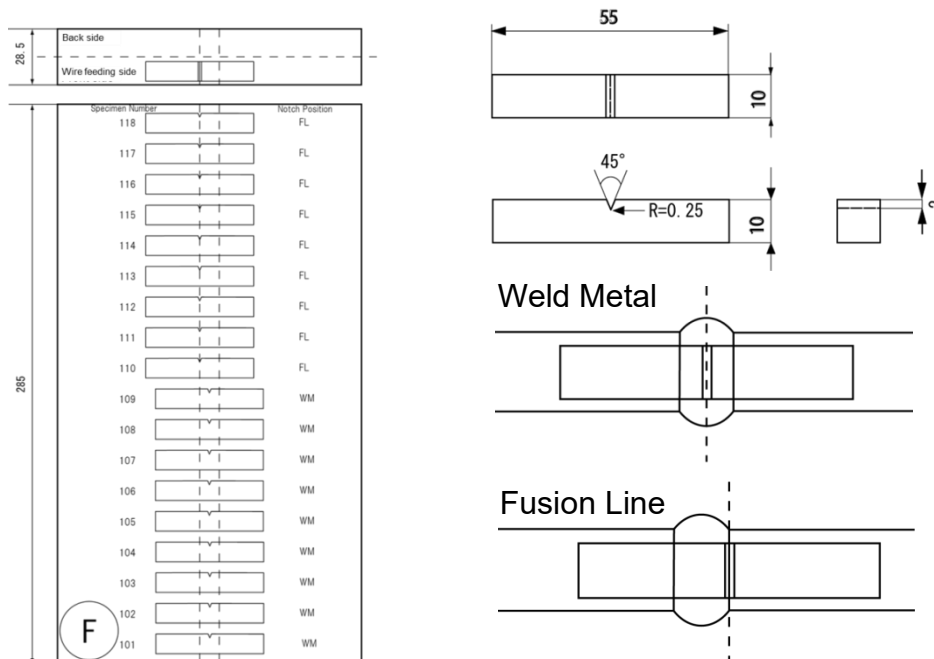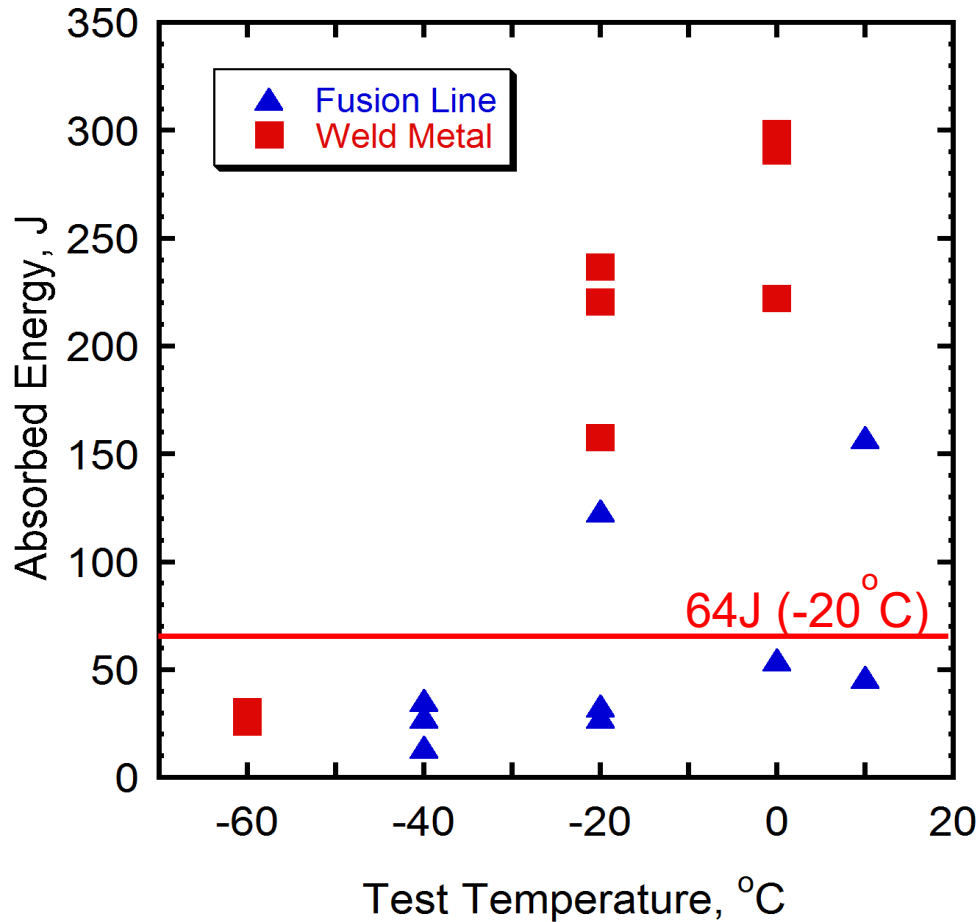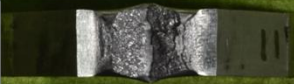The Charpy V-notch impact test results of the notch location at weld metal and fusion line is shown in Fig. 4.16. The weld metal shows high absorbed energy at temperature of -20 ^{o}C, which satisfied the ClassNK standard (64 J at -20 ^{o}C). The fracture surface of the Charpy impact specimens is shown in Fig. 4.17(b). At 0 ^{o}C, the fracture surface indicates completely plastic deformation. At -20 ^{o}C, shows plastic deformation with a little brittle deformation and at -60 ^{o}C, shows a brittle manner without plastic deformation. Thus, the DBTT is between -20 ^{o}C to -60 ^{o}C.

However, Fig. 4.16 shows that the fusion line obtained the unstable absorbed energy even in temperature above -20 ^{o}C. Large grain size and grain boundary ferrite observed in the fusion line microstructure are mentioned in Fig. 4.10 that affects the unstable absorbed energy although the low heat input can be achieved. The fracture surface of the Charpy impact specimens is shown in Fig. 4.17(a). Almost all specimens showed a brittle deformation in a straight direction. Then the microstructure of the fracture path in a low absorbed energy specimen (no.F112) is observed in Fig. 4.18. The crack path propagates along with a fusion boundary that has a fraction of grain boundary ferrite. Moreover, the cleavage fracture surface is observed by SEM.

Notch Position: Fusion Line			
No.F118: 46.3 J, 10℃ Crack Direction: Straight		No.F113: 28.0 J, -40℃ Crack Direction: Straight	
No.F117: 157.5 J, 10℃ Crack Direction: Straight		No.F112: 33.1 J, -20℃ Crack Direction: Straight	
No.F116: 54.6 J, 0℃ Crack Direction: Straight		No.F111: 28.0 J, -20℃ Crack Direction: Straight	
No.F115: 35.7 J, -40℃ Crack Direction: Straight		No.F110: 123.4 J, -20℃ Crack Direction: Straight	
No.F114: 13.8 J, -40℃ Crack Direction: Straight			
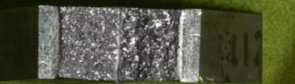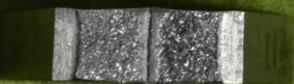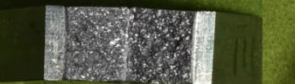
(a) Fusion line

Notch Position: Weld Metal			
No.F109: 290.4 J, 0℃ Crack Direction: Straight		No.F104: 30.5J, -60℃ Crack Direction: Straight	
No.F108: 222.0 J, 0℃ Crack Direction: Straight		No.F103: 236.6 J, -20℃ Crack Direction: Straight	
No.F107: 298.4 J, 0℃ Crack Direction: Straight		No.F102: 157.5 J, -20℃ Crack Direction: Straight	
No.F106: 26.8 J, -60℃ Crack Direction: Straight		No.F101: 220.5 J, -20℃ Crack Direction: Straight	
No.F105: 25.6 J, -60℃ Crack Direction: Straight			
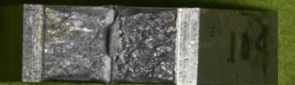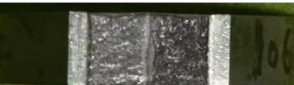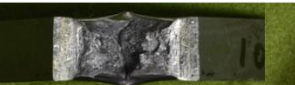
(b) Weld metal

Fig.4.17 Fracture surface and direction of Charpy impact test specimen in (a) fusion line and (b) weld metal.

61
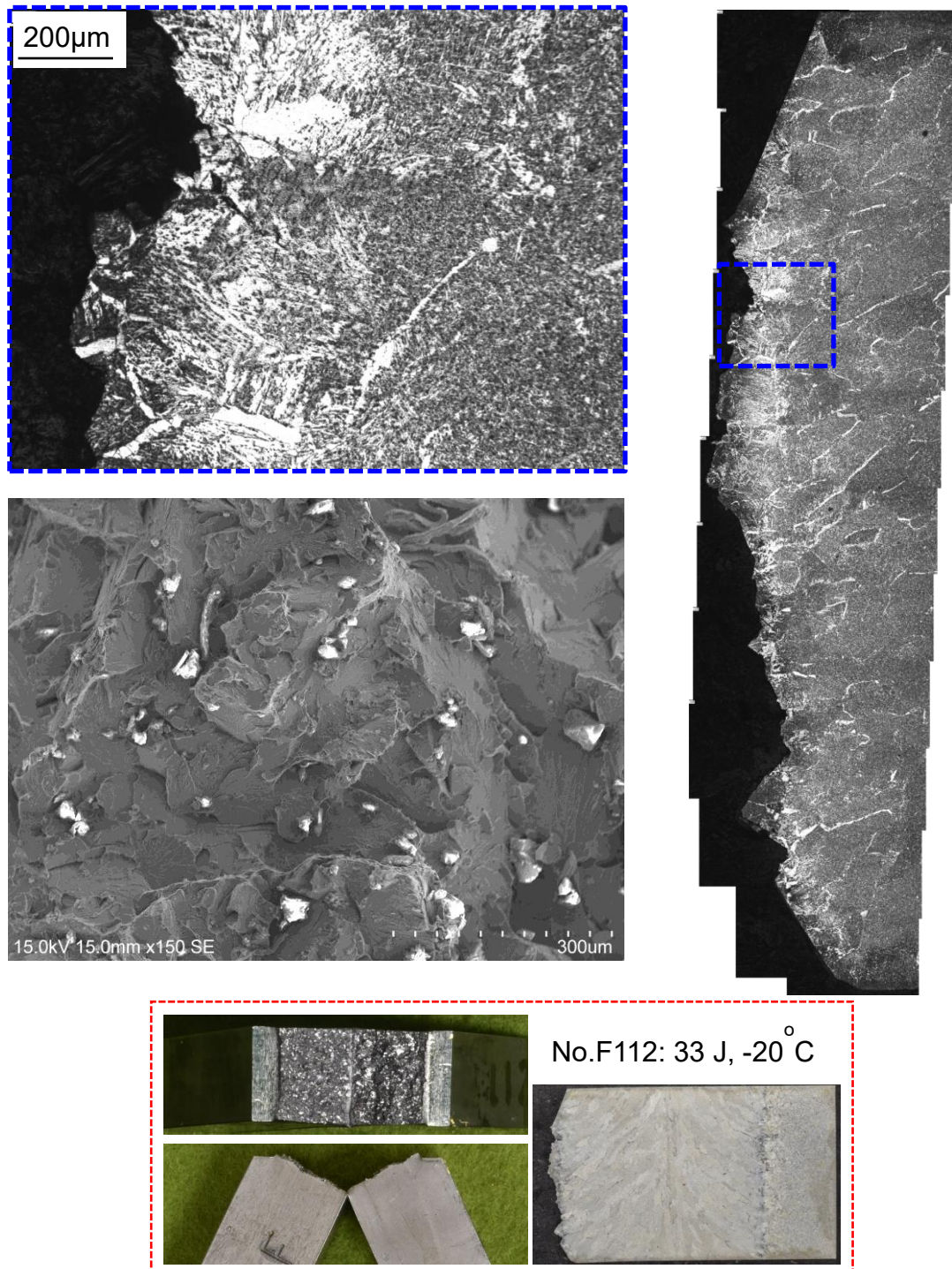
Fig. 4.18 Microstructure of fracture path and fracture surface in Charpy impact specimen at fusion line.

4.4.5 Crack tip opening displacement (CTOD) test of the welded joint

The CTOD test is one fracture toughness test that is used when some plastic deformation can occur prior to failure. The schematic diagram of a test piece is shown in Fig. 4.19. A specimen given the tip of a crack is bent by an external force. While the test is in process, the crack tip opening displacement (V_p) and load are recorded automatically and the CTOD value (δ_c) is calculated from V_p. The higher the CTOD value is, the higher the fracture toughness is.

In this experiment the location of notch in the weld metal using two specimens. The CTOD test results are shown in Table 4.4. The weld metal exhibits the high resistance to brittle propagation at -10 ^{0}C with the CTOD values exceeding 0.25 mm. According to the load/displacement chart in Fig. 4.20, both charts show plastic deformation before failure and the fracture surface in Fig. 4.21 is to ensure that the crack opening straightly propagates.
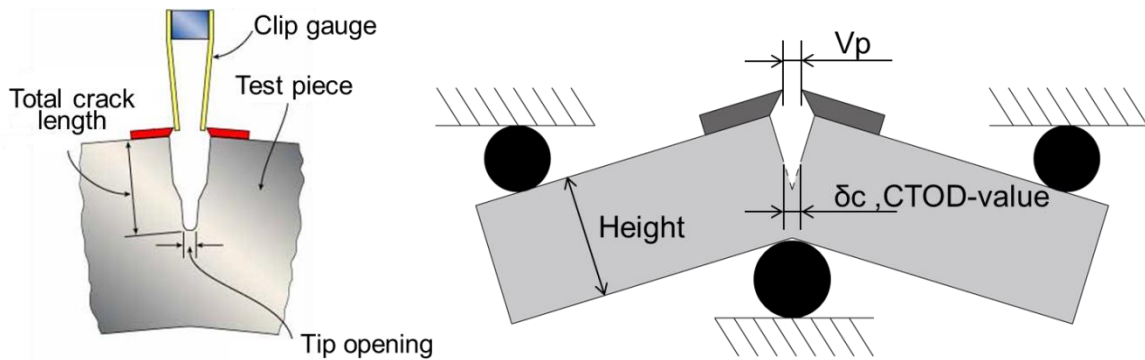
Fig. 4.19 Schematic illustration of CTOD test.

Table 4.4 CTOD test results.

Test Piece	YM60-1	YM60-2
Width, mm	22.1	21.8
Height, mm	44.6	44.6
Shape in the notch	U	
Notch location	Weld Metal	
Test temperature,℃	-10	
F, kN	43.9	44.2
V_p, mm	1.601	2.561
δc (CTOD-value), mm	0.467	0.725
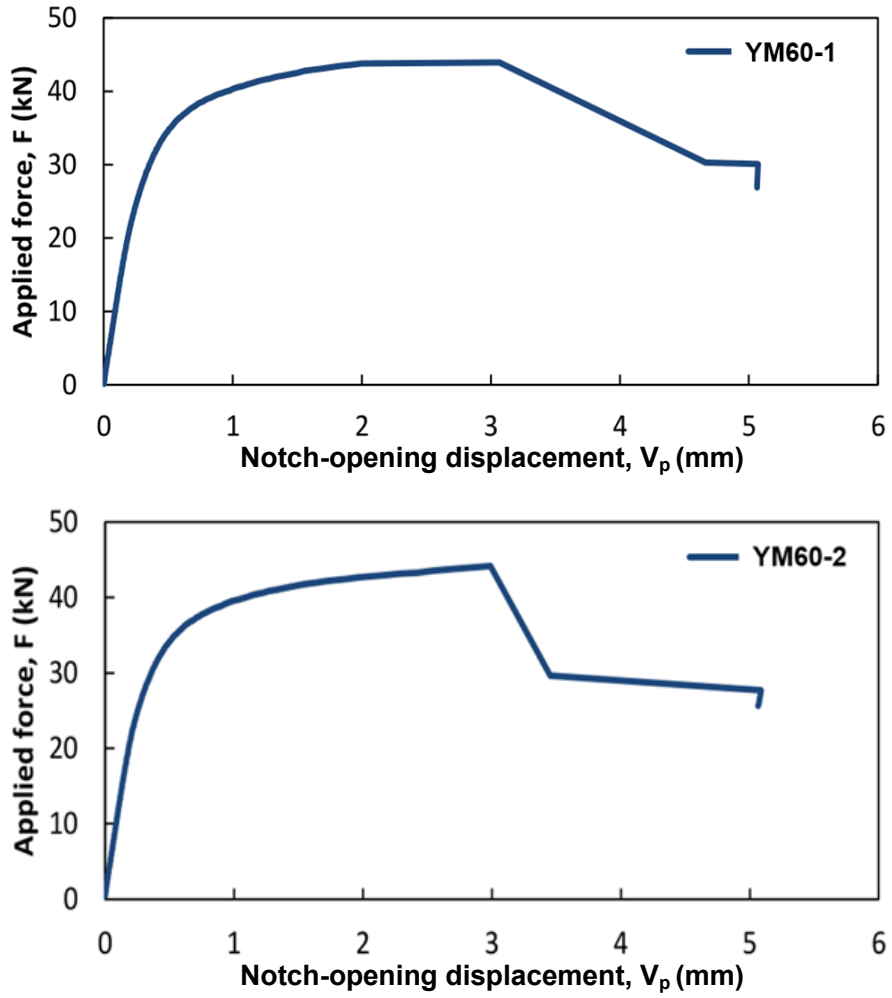
Fig. 4.20 Load VS Crack opening displacement (V_p).
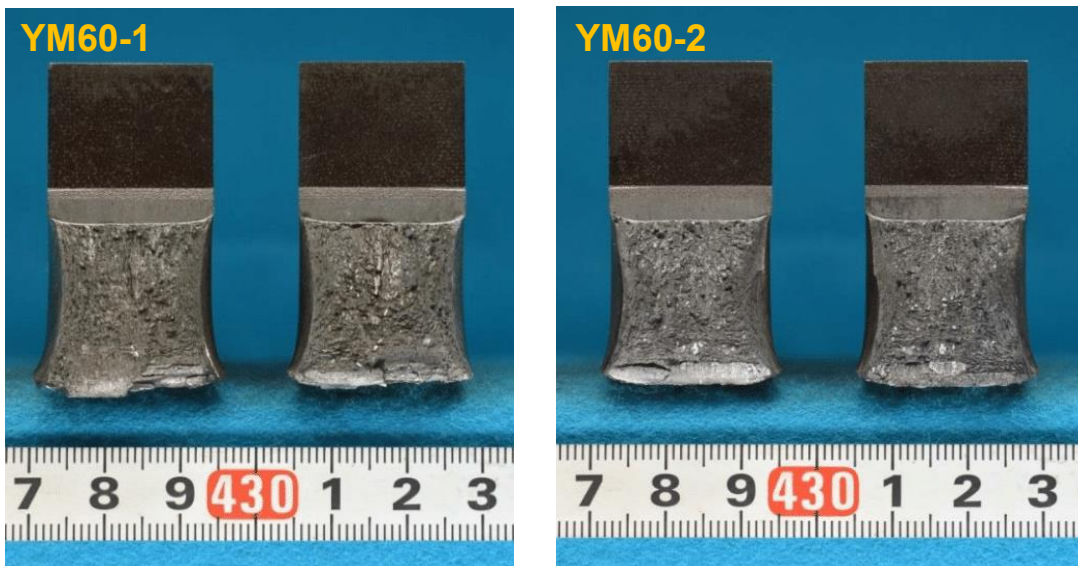
Fig. 4.21 Fracture surface of CTOD specimen.

4.5 Summary

In order to improve the proposed welding process for a practical use, the vertical hot-wire laser welding system with a self-propelled base was developed in order to do the trial for the long weld joint similar to the field welding based on the previous investigations of the optimization of welding conditions, and then the properties of the welded joint were investigated.

1) The optimal welding conditions of laser power distribution, hot-wire system, shielding gas, etc. were developed to apply for the large size specimen of 500 mm and 1300 mm in length. During welding, this process achieved stable welding phenomena continuously the whole welding period and a sound welded joint could be observed even the heat source of laser head and hot-wire system moved.

2) The HLW joint of long-welded specimen obtained low dilution and narrow heat affected zone as a result of the low heat input welding process and the heat input of the HLW welded joint is much lower than that of the EGW welded joint at the same thickness of base metal.

3) According to properties of the HLW welded joint, the tensile strength met the requirement of the specification. The V-notch Charpy impact test result of notch location at weld metal showed high absorbed energy at -20^0C according to CTOD test results that exhibited the high resistance to brittle propagation at -10^0C. However, the fusion line obtained the unstable absorbed energy because grain boundary ferrite could be observed in the fusion line.

Chapter 5

Development of vertical welding for heavy-thick steel plate using twin diode lasers and hot wire

5.1 Introduction

In the previous chapter, the conceptual idea of the new welding method and preliminary investigations in welding phenomena were presented. The combination of a diode laser with a rectangular beam spot and a hot-wire feeding system were performed on steel plates with its thickness up to 28.5 mm. In addition, the effects of welding conditions such as the laser beam with high-edged energy, weaving motion, shielding gases and so on were investigated. In this chapter, the twin diode laser system is applied to increase a total laser power for thicker plates with 50-mm thickness. Moreover, optimization of laser irradiation conditions is studied using a twin diode laser system with special optics systems such as a weaving head and a high-edged energy lens.

Firstly, the principles and basic ideas to improve the laser beam control using twin diode lasers for 50-mm thickness are presented and then this part illustrates introducing the methodology of a joint configuration and apparatus applied for investigating the advanced laser beam control of twin diode lasers with a total power of 12 kW and the hot-wire system. The power density distribution is determined to be sufficient for melting the base metal and keeping the molten pool by using a high-edged energy beam and a weaving beam. In addition, double stable beams without weaving are also investigated.

Secondly, the weld bead appearances and cross-sections of heavy-thick joints in varied laser power distribution as described in the previous section are observed

Thirdly, this part shows the properties of vertical welding joints in 50-mm plates using twin diode lasers with the hot-wire system. The microstructure, Vickers hardness test, and Charpy impact test are presented.

5.2 Optimization of advanced laser beam control of twin diode lasers for vertical welding

Because of the limited power of a 6-kW diode laser, one laser beam isn't sufficient for melting the base metal and keeping the molten pool in a heavy-thick joint. Therefore, this part would like to improve the laser beam control of twin diode lasers and to apply for 50-mm-thick specimen.

5.2.1 Investigating power distribution on rectangular laser beams for 50 mm steel plate

As shown in Table 3.1, the rectangular beam shape can be changed by combining the optical lenses of a laser head. In case of 50-mm thickness, in three welding conditions the beam length fits the thickness based on the optimal focal length and accessibility for setting a stable beam and a weaving beam. The laser beam shapes and their intensity distribution used in this chapter are shown in Fig 5.1 and Fig 5.2. Figure 5.1 shows large rectangular laser beams fitting a groove area. These beams irradiate into the groove stably without weaving. Figure 5.1(a) is a uniform energy beam that is excellent to keep power density on a whole area of a molten pool steady. On the other hand, a high-edged energy beam in Figure 5.1(b) made by a special homogenizer can concentrate more power density on the beam edges and in the meantime, it can keep power density on the molten pool so that we can improve dilution and reduce lack of fusion on groove edges. Figure 5.2 shows the narrow and middle rectangular laser beams. Both beams are narrower than a gap width and combined with the weaving head to move them throughout the gap area. The beam motion of weaving waveform and frequency is controlled and described in Table 3.3. The average power density of the narrow beam in Figure 5.2 (a) is higher than that of the middle beam in Figure 5.2 (b) and therefore can concentrate more power density on groove surfaces.

(a) Uniform energy beam   (b) High-edged energy beam

Fig. 5.1 Large rectangular laser beams fitting a groove area.

(a) Narrow beam   (b) Middle beam
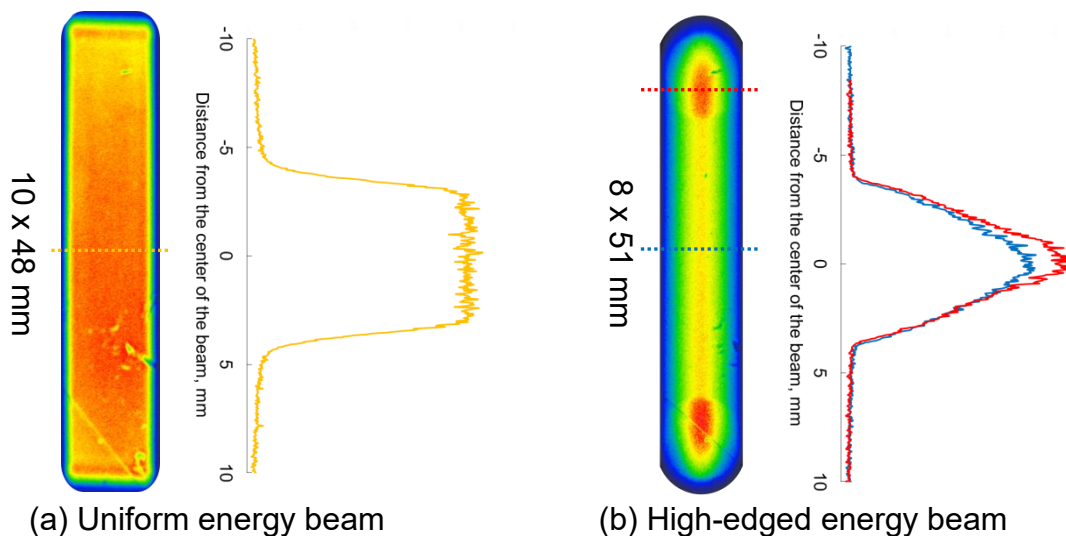
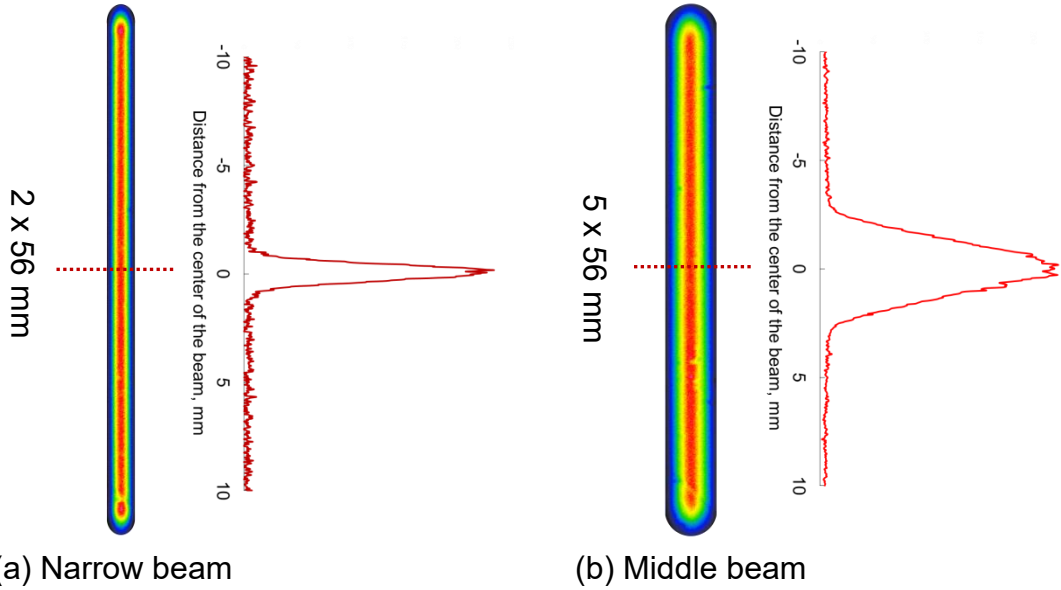Fig. 5.2 Narrow and middle rectangular laser beams combined with a weaving system.

5.2.2 Introduction of a joint configuration and equipment of the proposed process using twin diode lasers for a heavy-thick joint

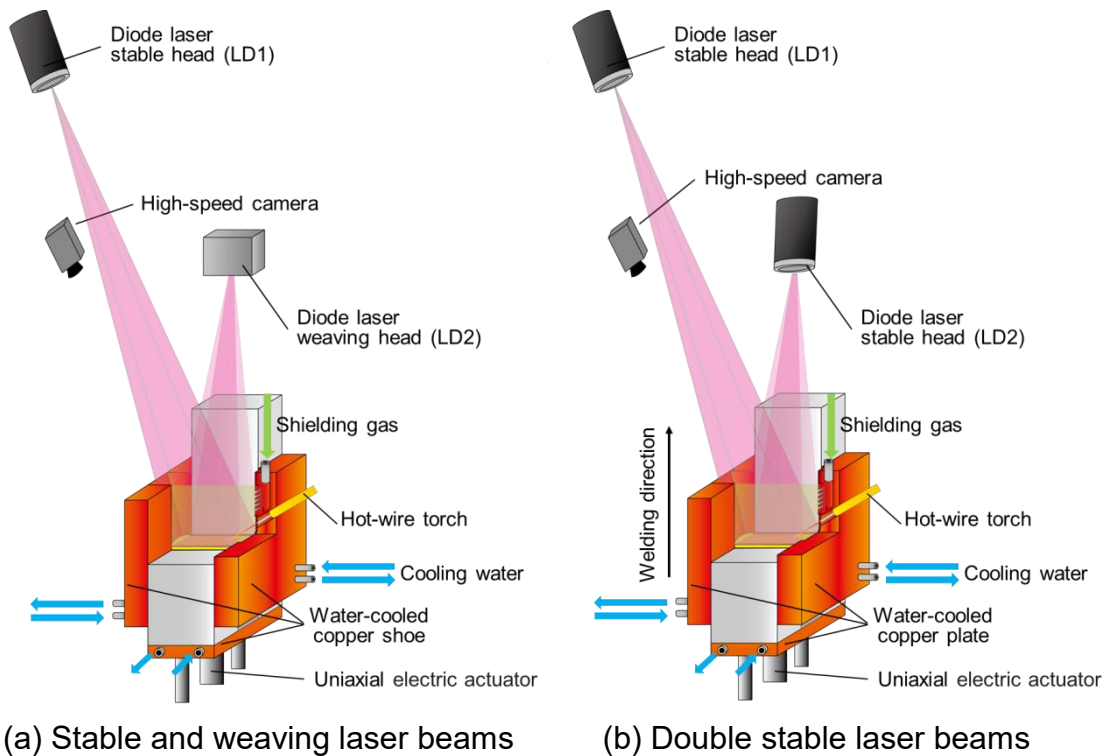(a) Stable and weaving laser beams   (b) Double stable laser beams

Fig. 5.3 Schematic layout of the experimental set-up for single-pass vertical welding using twin diode lasers.

The schematic layout of the experimental set-up for single-pass vertical welding using twin diode lasers and a hot wire is shown in Fig. 5.3. Two plates of a specimen were fixed inside a copper shoe and moved vertically by a uniaxial electric actuator. The covering copper shoe had a water cooling system inside used for keeping the weld pool shape of both a wire feeding side and the opposite side. Moreover, it had other slots for inserting a filler wire and a shielding gas to protect the molten pool. A filler wire deposited into the molten pool was electrically heated up to its melting point as called hot wire. Two high-power diode lasers were used as the main heat sources. For rectangular laser spot, a process fiber cable assembled with focusing and homogenizing lenses created an adjustable rectangular shape of a beam spot size according to a thickness and gap width, and a high-speed camera was applied to monitor weld pool formation, welding stability, and a hot-wire feeding during welding. Figure 5.3 (a), (b) shows the schematic layout of the proposed process using stable and weaving beams, and double stable laser beams respectively.

The welding phenomena during welding were monitored by a high-speed camera. Pencil camera V-193-M1 model was connected with NAC: MEMRECAM GX-5 module shown in Fig. 3.5. Table 5.1 shows the monitoring condition. The camera has a focal length of 35 mm with 25 mm diameter combined with a bandpass filter of 750 nm. Besides, the frame rate is 50 fps and the shutter speed is 1/20000 s.

Table 5.1 Monitoring condition of in-situ observation.

High-speed camera	GX-5
Frame rate, fps	50
Aperture	Closed
Focus lens, mm	35
Band pass filter, nm/FWHM	750 / 10
Lighting	N/A
Shutter speed, s	1/20000

5.3 Effects of power distribution on a heavy-thick welded joint using twin diode lasers and hot wire method

This part is to apply the combinations of two rectangular beams in different power distributions into the 50-mm-thick specimen. In order to achieve a sound joint, both diode lasers irradiate rectangular beams with special optics systems such as a weaving head and high edged energy lens to optimize power distribution and laser power that would be able to keep the molten pool and to melt the base metal stable.

5.3.1 Materials used

EH 40 steel that is available in shipbuilding standard was used as base metal material having a thickness of 50 mm. Its dimensions are shown in Fig. 5.4. The specimen size was 100w x 200h mm. Two plates were fitted up with a square groove having 10 mm gap, and a bottom spacer used for creating an initial molten pool had dimensions of 10w x 20h x 50d mm. JIS Z 3312 G78A4UM5C1M3T (a trade name of YM-80A, equivalent to ER110S-G) with a 1.6-mm diameter was used as a hot-wire filler material. Table 5.2 shows the chemical compositions of these materials.

Table 5.2 Chemical compositions of base metal and filler wire.

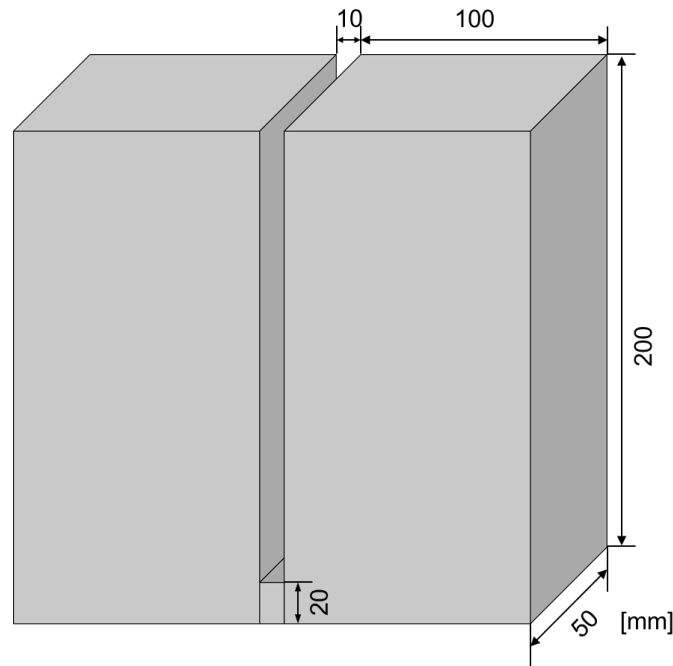| Materials	Chemical Composition, wt%											
	C	Si	Mn	P	S	Al	Cu	Ni	Nb	Ti	Cr	Mo
EH 40	0.12	0.31	1.34	0.007	0.003	0.012	0.01	0.01	-	-	-	-
YM-80A	0.06	0.40	1.69	0.006	0.003	-	0.20	3.01	-	0.05	0.46	0.29

Fig. 5.4 Specimen dimensions.

5.3.2 Experimental procedure

Table 5.3 shows the welding parameters of twin diode lasers and hot wire. As the intensity of laser beams in Fig. 5.1 and 5.2, there are three welding conditions used to investigate the effects of power distribution on the 50-mm-thick joint. Figure 5.5 (a), (b) and (c) illustrate both rectangular laser beams irradiated on a groove area in three conditions. The first diode laser (LD1) irradiated a large rectangular beam of 51 mm and 8 mm having a high energy density on both edges in its beam length. The beam was irradiated stably without weaving to keep power density on a whole area of a molten pool surface and to concentrate a high energy density on edges near plate surfaces, and this beam was used in all of the three welding conditions.

Table 5.3 Welding parameters of twin diode lasers and hot wire.

Laser type	LD 1	LD2		
Laser head type	Stable	Weaving	Weaving	Stable
Fiber core, mm	1.0	0.4	1.0	0.4
Collimator, mm	100	100	100	100
Homogenizer, LL-line	2.35-edge	2.20	2.20	2.85+2.20
Focus lens, mm	800	500	500	500
Laser power, kW	6	6	6	6
Laser irradiation angle	35°	$0°$	$0°$	$0°$
Defocus, mm	Just focus	Just focus	Just focus	Just focus
Spot size, mm x mm	8^w x 51^l	2^w x 56^l	5^w x 56^l	10^w x 48^l
Laser distribution type	High-edged	Uniform	Uniform	Uniform
Weaving frequency, Hz	None	5	5	None
Weaving waveform	None	Exponential	Exponential	None
Filler wire diameter, mm	1.6			
Welding speed, cm/min	3.3			
Wire feed speed, m/min	10			
Wire current, A	228			
Wire feeding angle	45			
Feeding position, mm	10			
Shielding gas, 10 l/min	80%Ar and 20%O_2			
Pre-irradiation time, s	80			

According to a study of power distribution in the groove area, the second diode laser (LD2) irradiated a varied beam size in three types of power distribution in a groove. The first condition in Fig. 5.5 (a), The LD2 irradiated a long and narrow rectangular beam of 56-mm length and 2-mm width and the second condition in Fig. 5.5 (b), the LD2 irradiated a middle rectangular beam of 56-mm length and 5-mm width. Thus, both laser beams that were narrower than gap width applied with

a weaving system using a 5-Hz exponential waveform. Figure 5.6 shows the schematic of laser beam motion and weaving amplitude in one cycle. In one cycle of a 5-Hz exponential waveform, the holding time of the laser spot on each groove surface is about 72.5 ms and the moving time between is about 27.5 ms.

(a) First condition   (b) Second condition   (b) Third condition
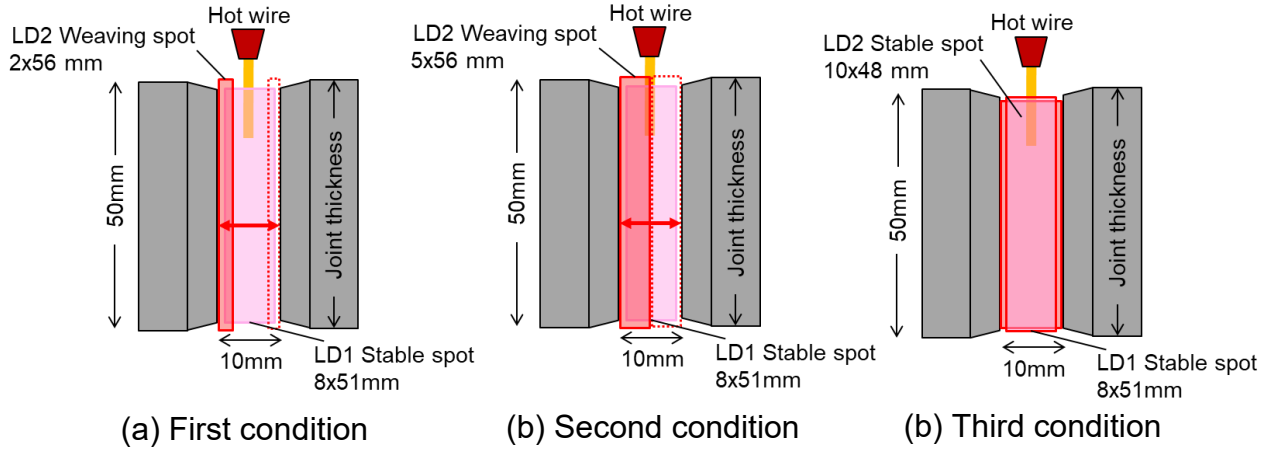
Fig. 5.5 Illustration of twin laser irradiations in three welding conditions.
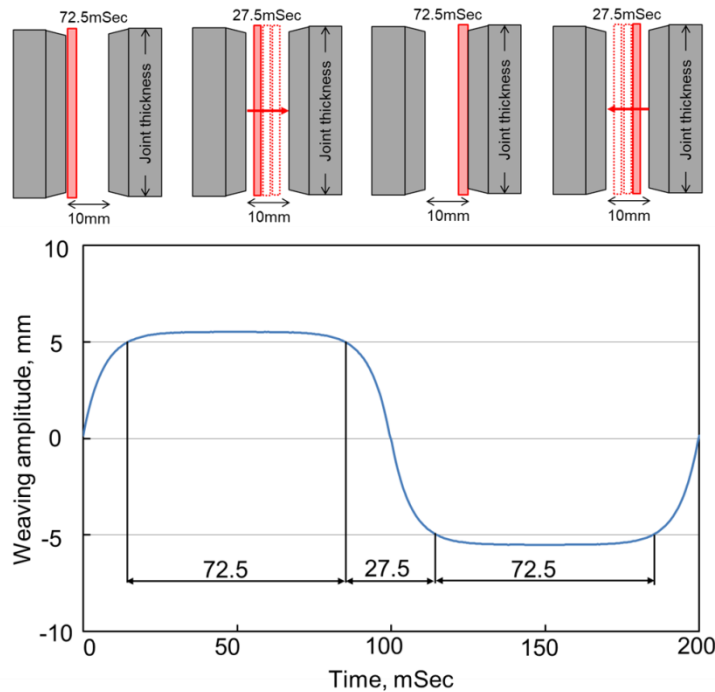
Fig. 5.6 Schematic layout of laser motion and amplitude at a 5-Hz exponential waveform.

In case of 2-mm beam width, the moving distance is 3 times wider than the laser spot width. Therefore, the average of a laser power density on the middle of groove was very low compared with it on near groove surfaces, and regarding narrow beam having high power density, the longer holding time generates more heat energy where it is close to groove surfaces. In case of 5-mm beam width, the beam moves slower due to shorter moving distance and it is placed on a half of a gap area, so this

beam can divide some power density into the weld pool and in the meantime when it is holding on the groove surface, there is some laser reflection to the groove surface. The third condition in Fig. 5.5 (c), the LD2 irradiated a large rectangular beam of 48-mm length and 10-mm width with uniform power density fitting groove area. The beam was irradiated stably without the weaving system. Therefore, this beam can keep heating on the molten pool, but it is poor to melt the base metal as a result of low laser reflection.

5.3.3 Welding performing of twin diode lasers for a heavy-thick joint and weld bead appearance
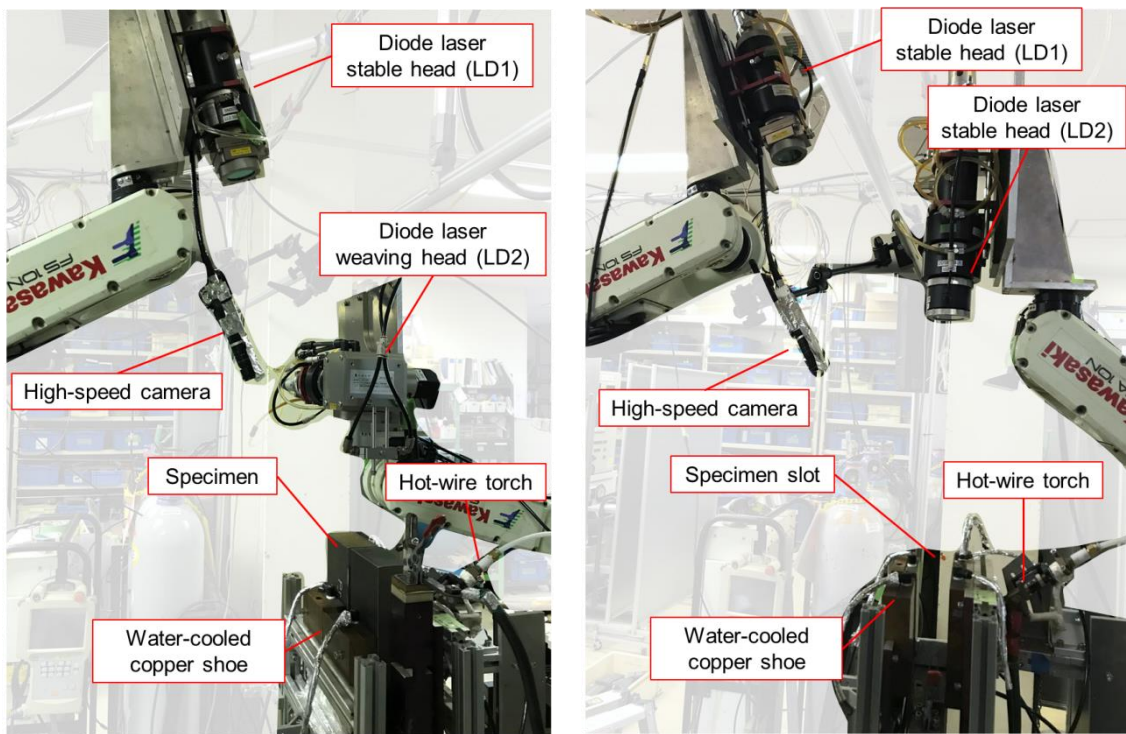
(a) Stable and weaving laser beams   (b) Double stable laser beams

Fig. 5.7 Photographs showing experimental set-up of twin diode lasers and hot wire.

Figure 5.7 shows photographs of the actual experimental set-up of vertical welding using 2 diode lasers and the hot-wire system for the 50-mm-thick specimen. Because of the access of both laser heads to the specimen and their focal length, only the small size jig can be employed. Figure 5.7 (a) shows diode lasers of a stable head (LD1) and a weaving head (LD2) which were applied for the first and second welding conditions as the aforementioned procedure. LD1 irradiated a large rectangular beam obliquely at a 35^0 angle on the opposite side of the wire feeding. In addition, the beam had a high-edged energy type, and LD2 irradiated a narrower rectangular beam straightly into the groove area. Figure 5.7 (b) shows double stable

diode lasers of the third welding condition. LD1 irradiated the same beam as first and second welding conditions, and LD 2 irradiated a large rectangular beam having a uniform energy type stably without weaving. Moreover, the whole welding period the high-speed camera monitored weld pool phenomena and hot-wire feeding. The specimen mentioned in Fig. 5.4 was fixed on a base plate by tack welding before inserted in a copper shoe and only one hot-wire feeding was used.

5.3.3.1 In-situ observation

The welding phenomena during welding were monitored by a high-speed camera. Pencil camera V-193-M1 model connected with NAC: MEMRECAM GX-5 module. The camera had a focal length of 35 mm with a 25-mm diameter and a bandpass filter of 750 nm. Besides, the frame rate was 50 fps. Before hot-wire feeding, the 6-kW weaving laser and 6-kW stable laser irradiated onto the groove area on the spacer surface to generate an initial molten pool for 80 s since a large quantity of the weld metal volume was deposited into the heavy-thick joint, and the molten pool by the pre-irradiation in the groove area could help to melt and distribute the feeding wire steadily. Figure 5.8 shows high-speed images taken before hot-wire feeding of the 2 x 56 mm weaving and 8 x 51 mm stable beams using the proposed process. In pre-irradiation images before hot-wire feeding, the 1.32 s image shows the weaving laser held on a groove surface and high-edged stable laser irradiation. In the 1.36 s image, the weaving laser is moving to the other side and then the 1.42 s image shows the weaving laser is held on the other side. This laser spot motion repeats during welding. The 80.00 s image shows the stable molten pool by pre-irradiation before hot-wire feeding on the whole groove area.
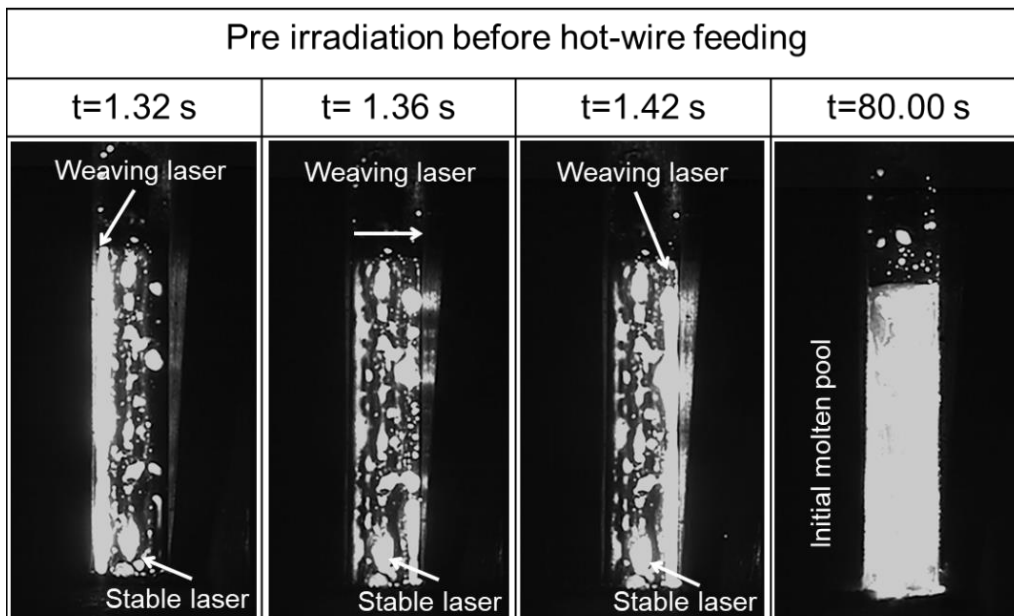

Fig. 5.8 High-speed images in pre-irradiation of the 2x56 mm weaving and 8x51 mm stable beams.

Figure 5.9 shows a schematic layout and a clear explanation of a weld pool perspective compared with a high-speed image of weld pool phenomena of the 2x56 mm weaving and 8x51 mm stable beams during welding. The image shows an example of a large rectangular weld pool generated by twin diode lasers and hot-wire feeding. The hot wire is fed into the molten pool and the specimen moves downward vertically. The steady weld pool formation and wire feeding were observed continuously for the whole welding period. The single hot-wire feeding could deposit the weld metal sufficiently for the heavy-thick joint, as a result the sufficient weld metal could be achieved both on the back side and wire feeding side.
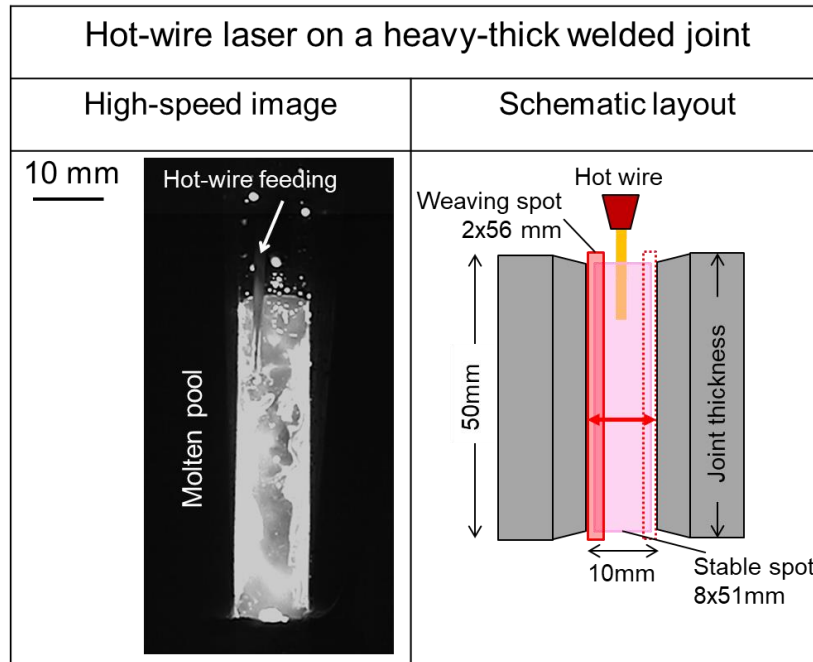
Fig. 5.9 High-speed images and schematic layout during welding of the 2x56 mm weaving and 8x51 mm stable beams.

5.3.3.2 Weld bead appearances

According to the weld bead appearances in Fig. 5.10, all of three welding conditions could carry on the vertical weld joints using the combination of twin diode lasers and the hot-wire system. The stable welding phenomena until the finish could be observed. In other words, the proposed process achieves a steady welding process continuously regarding the adequate power density distribution and hot-wire system. The weld beads obtain complete penetration and there is no visible lack of fusion that could affect the properties of the welded joint.

Weaving and stable laser beams		Double stable laser beams
8x51 mm and 2x56 mm	8x51 mm and 5x56 mm	8x51 mm and 10x48 mm

Wire feeding	Back	Wire feeding	Back	Wire feeding	Back

Fig. 5.10 Weld bead appearances of heavy-thick welded joints.

5.3.4 Cross-sections and joint properties of heavy-thick specimens using the proposed method

5.3.4.1 Macro cross-sections

Figure 5.11 shows the macro cross-sections. The cross-sections of the welded joint by using the proposed process were derived from different power distributions on the heavy-thick grooves cut at the same level of 70 mm from the welding start.

Accordance to the cross-sections of stable and weaving beams, the stable laser beam with the high-edged energy of LD1 that could concentrate more power density on edges of a welded joint and keep energy the whole groove combined with the weaving beam of LD2. The 2-mm beam width with the weaving system provided higher energy density and greater laser reflection to the groove surfaces compared with the 5-mm beam width, but the 5-mm beam width distributed higher energy density on the molten pool near groove surfaces and in the same time the peak of energy density could be reflected to the base metal. Therefore, both laser beams could melt the base metal sufficiently. The cross-sections of 2x56 mm beam and 5x56 mm beam even having different power density show similar weld beads and no lack of fusion can be found. The low dilution and narrow HAZ can also be observed, that is, this process is a low heat input welding method.

In case of double stable lasers, both laser beams were irradiated stably without a weaving system in the whole welding time. Regarding this combination, power distribution spread on an entire groove area that was excellent to keep the molten

pool, but poor at melting the base metal owing to low laser reflection on the groove walls. The cross-section shows very low dilution and reveals some lack of fusion near the wire feeding side. As shown in Fig. 5.12, the bead width on the wire feeding side is relatively small since the filler wire cut the laser beams above the molten pool. Therefore, the actual laser power density in this area become lower and dilution is smaller in the wire feeding side than in the middle and back side of the welded joint.

Consequently, the stable laser beam with the high-edged energy type and the weaving beam can optimize the laser power distribution in a heavy-thick groove. The power density concentrated on edges of a welded joint and groove wall surfaces can increase base metal dilution and reduce lack of fusion. Moreover, the hot-wire system can heat a filler wire up to its melting point, therefore the power density to melt a large amount of the filler wire deposited in the middle groove can be reduced.

Stable and weaving laser beams		Double stable laser beams
8x51 mm and 2x56 mm	8x51 mm and 5x56 mm	8x51 mm and 10x48 mm
Lack of fusion, mm		
0	0	8
Dilution Area, mm^2		
114	111	52
HAZ width, mm		
13	15	14
Coarse grain region, mm		
1.47	1.5	1.43

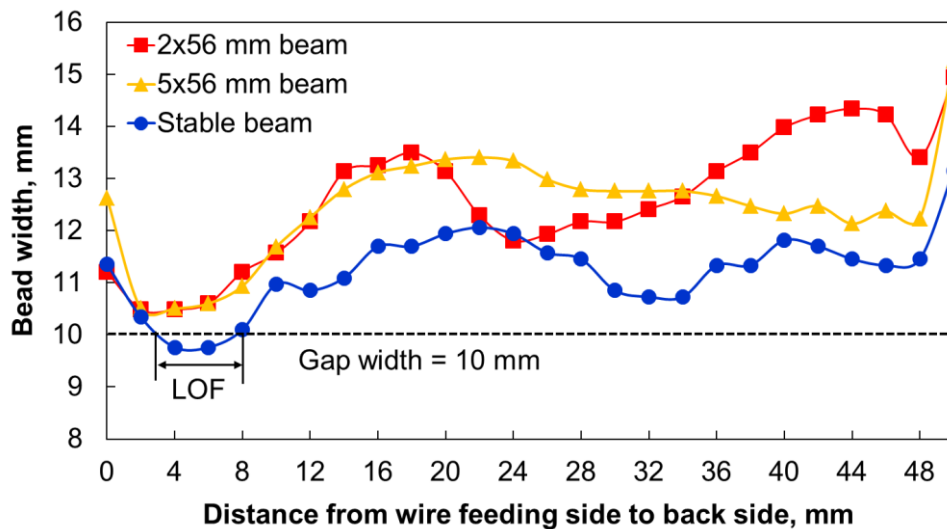Fig. 5.11 Macro cross-sections of heavy-thick specimens.

Fig. 5.12 Measured bead width of the welded joints.

5.3.4.2 Microstructure characteristics

Figure 5.13 (a), (b), (c) show microstructure of HAZ and FL of the welded specimens. The proposed process achieved the narrow CGHAZ about 1.5 mm in a heat input of 218 kJ/cm for the 50-mm specimen. As the study of the previous chapter, the 28-mm specimen using the heat input of 144 kJ/cm had 0.83-mm CGHAZ, therefore the heat input is the main effect to enlarge CGHAZ. The CGHAZ region of three specimens is not significantly different even though the weaving and stable lasers obtain the higher dilution. Consequently, the advanced laser beam control can change the power density distribution and also affect the melting of base metal, but not has an influence on the CGHAZ region. At the fusion boundary, a fraction of ferrite and bainite are found along with fusion line. At the CGHAZ, pro-eutectoid ferrite and lower bainite are observed.

Figure 5.14 shows an example of weld metal microstructure. The results show fine lower bainite and ferrite generated in the weld metal
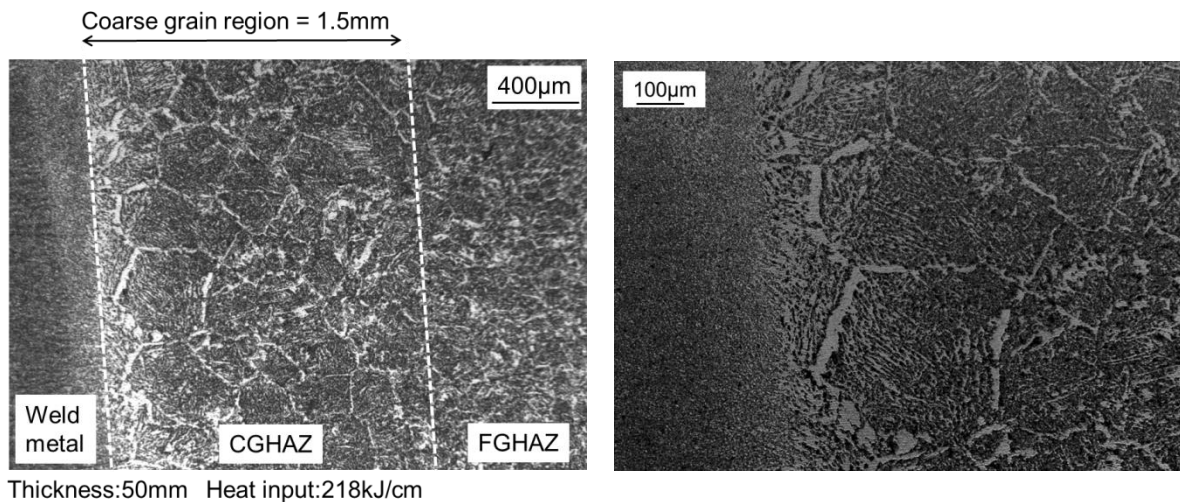
(a) Microstructure of weaving (2x56mm) and stable beams.
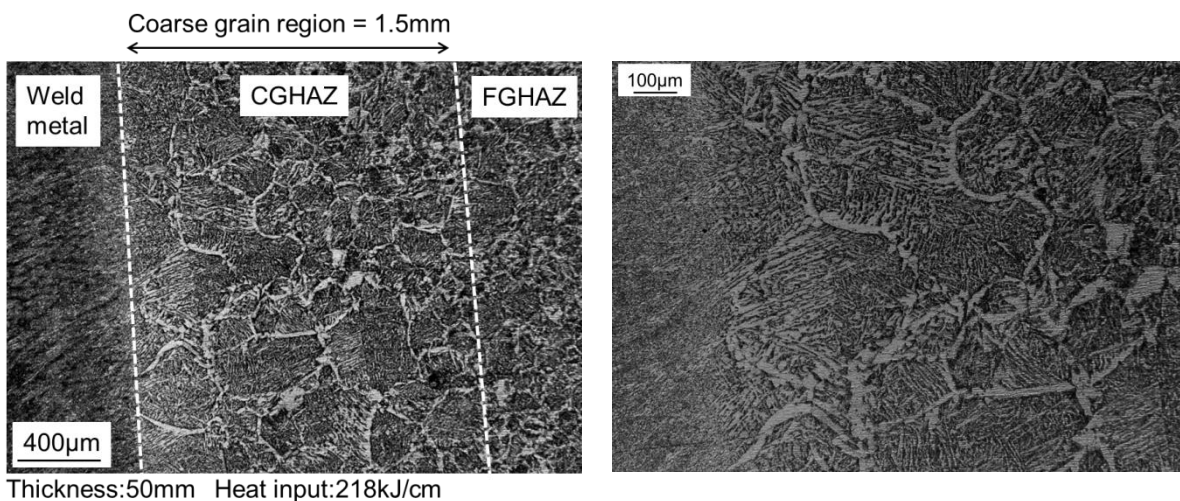
(b) Microstructure of weaving (5x56mm) and stable beams.

Fig. 5.13 Microstructure of heat affected zone and fusion boundary.
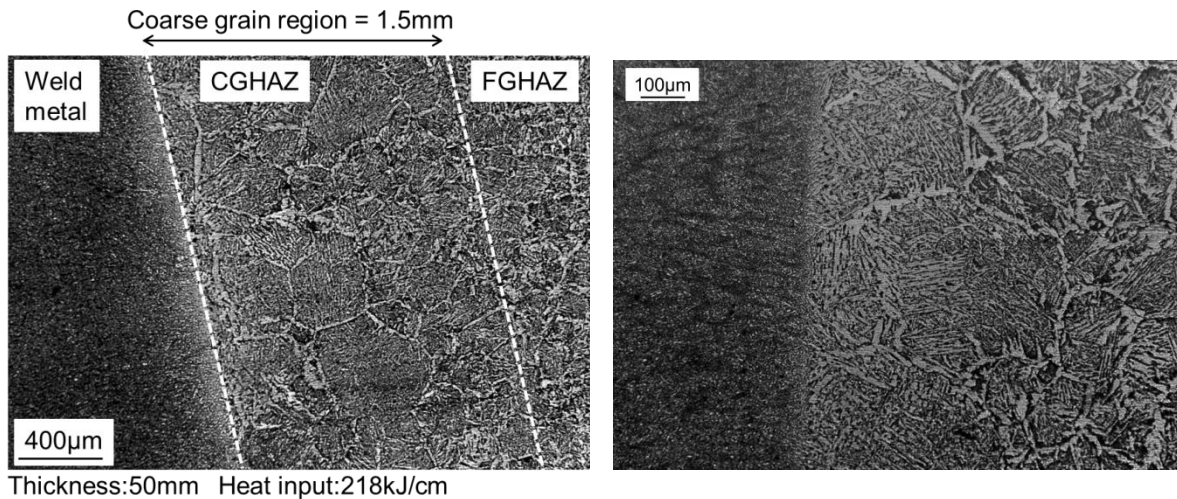
(c) Microstructure of double stable lasers.

Fig. 5.13 Microstructure of heat affected zone and fusion boundary (continued).
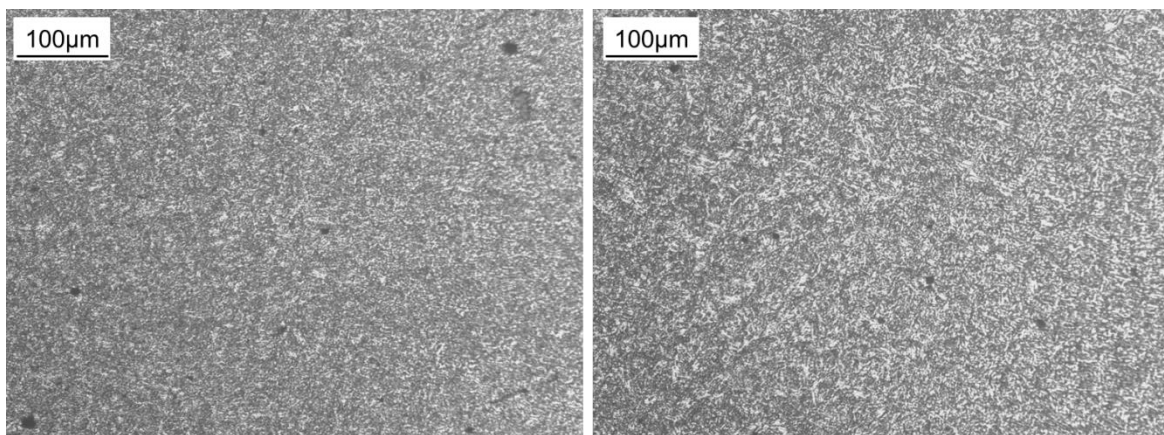
Fig. 5.14 Microstructure of weld metal.

5.3.4.3 Vickers Hardness distribution

A micro Vickers hardness tester (MHT-1, manufactured by Matsuzawa Seiki Co., Ltd.) was used for the measurement. The load was 1 kgf and the holding time was 10 s in accordance with JIS Z 2244.

Figure 5.15 shows the hardness distribution through the base metal, HAZ and weld metal on the middle of thickness. The results find that all of the welding conditions are alike. The mean weld metal hardness of 270 HV is much higher than the base metal hardness about 160-170 HV due to a high strength material of filler wire and it also shows that the softening degree in HAZ was 150-160 HV and similar to the base metal.

Fig. 5.15 Vickers hardness distribution in the middle of the welded joints.

5.3.4.4 V-notch Charpy impact test

The toughness property of the specimen of 2x56 mm weaving and 8x51 mm stable beam was investigated. Figure 5.16 shows the cutting plan and notch locations of test pieces. The V-notch is located at weld metal and fusion line with the test temperature of -20°C. The standard specimen size for Charpy impact test is 10mm x10mm x55mm according to JIS Z 2242. In this test, the Charpy test equipment has a heavy pendulum of 25.31kg and arm length of 0.7 m.

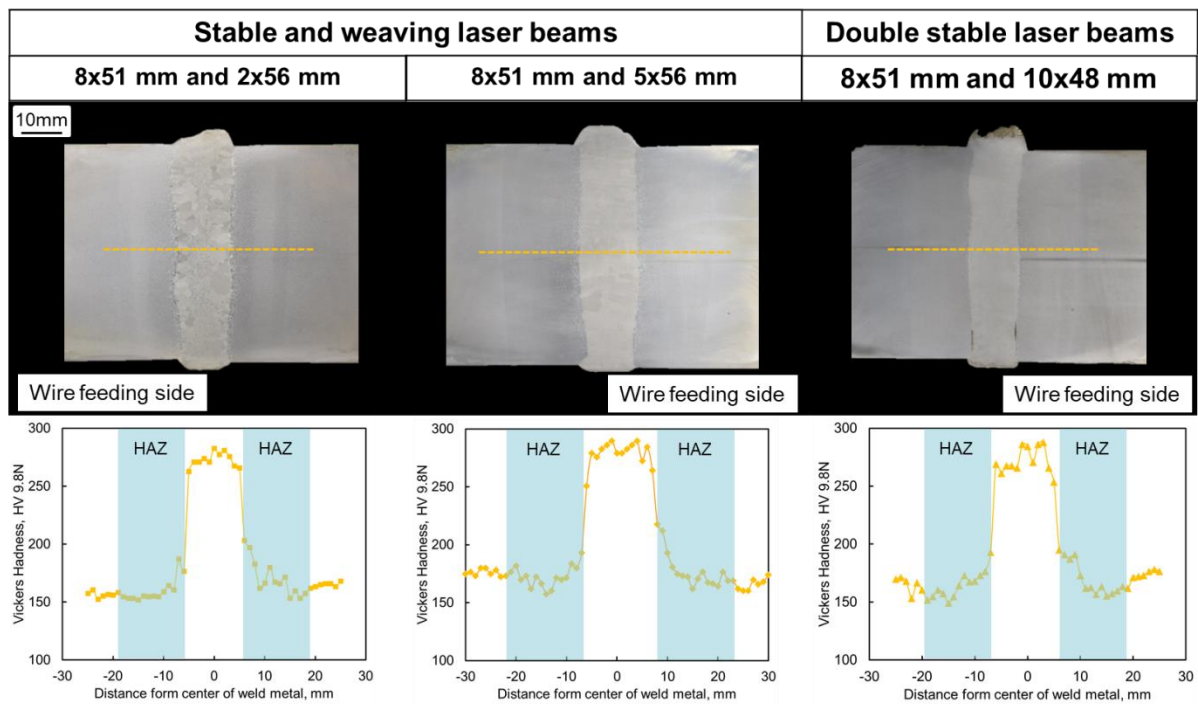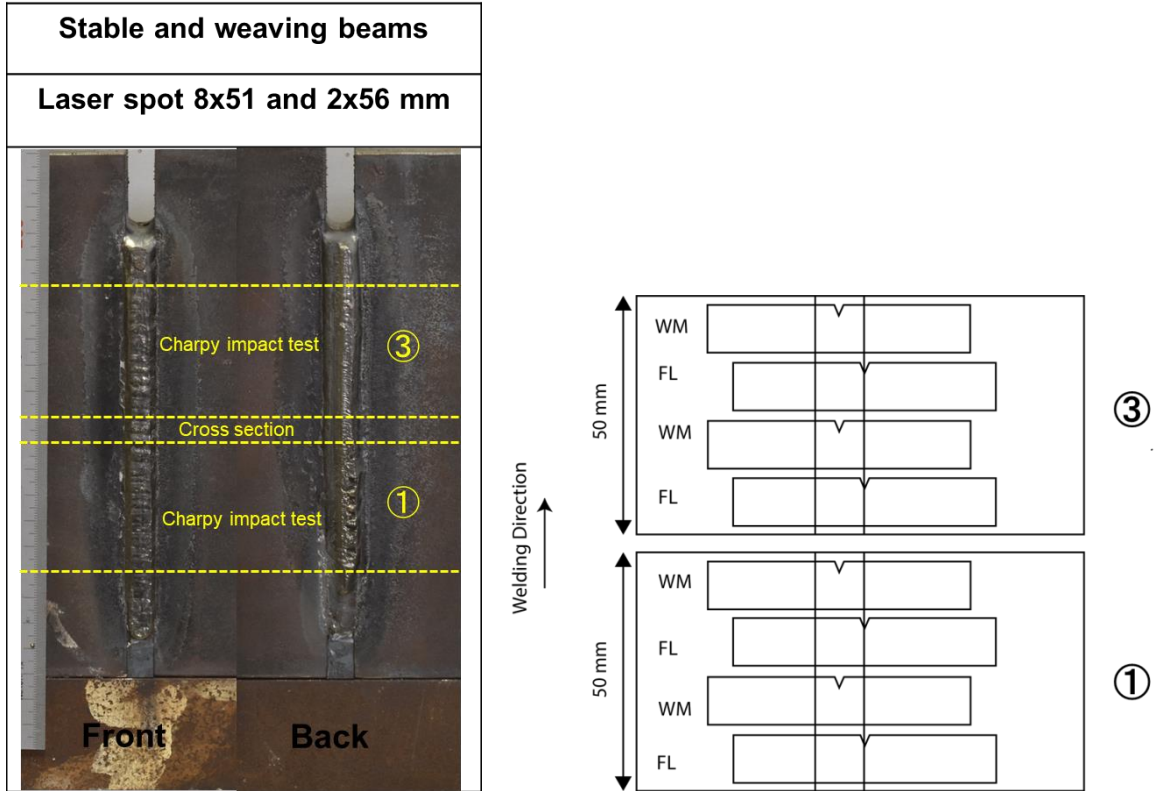The V-notch Charpy impact test result of the notch location at weld metal and fusion line is shown in Fig. 5.17. According to the Japan Marine Standard of the ClassNK, the minimum average impact test value of the welded joint is 64 J at -20 ^{o}C. The weld metal obtains high absorbed energy more than 64 J. However, the fusion line shows the low absorbed energy having the mean value of 40 J less than the specification requirement. Because grain boundary ferrite is observed in the fusion line as shown in Fig. 5.13 which affects the unstable absorbed energy although the low heat input can be achieved.

The fracture surface and crack direction are shown in Fig. 5.18. For fusion line, almost all specimens show a brittle deformation in a straight direction and in two specimens, the cracks propagate from fusion line to base metal showing high absorbed energy as called fracture path deviation (FPD). Then the microstructure of fracture path in a low absorbed energy specimen is observed in Fig. 5.19 to confirm that the crack path propagate along with fusion boundary having a fraction of grain boundary ferrite. Moreover, SEM observes the cleavage fracture surface.

(a) Cutting plan.
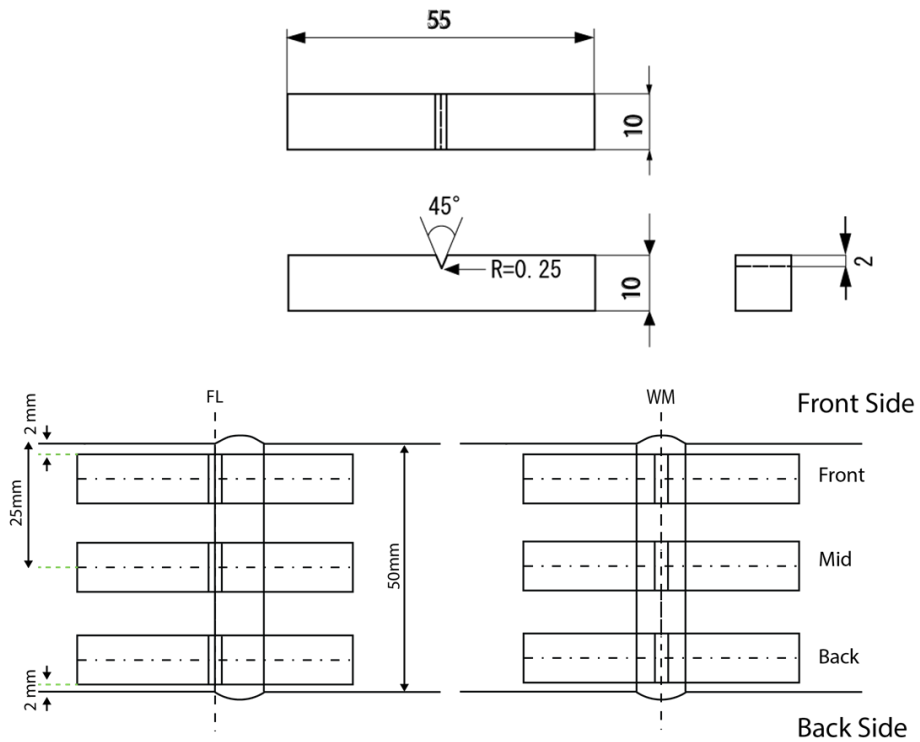
(b) Test pieces and notch location.

Fig. 5.16 Preparing specimen for V-notch Charpy impact test.
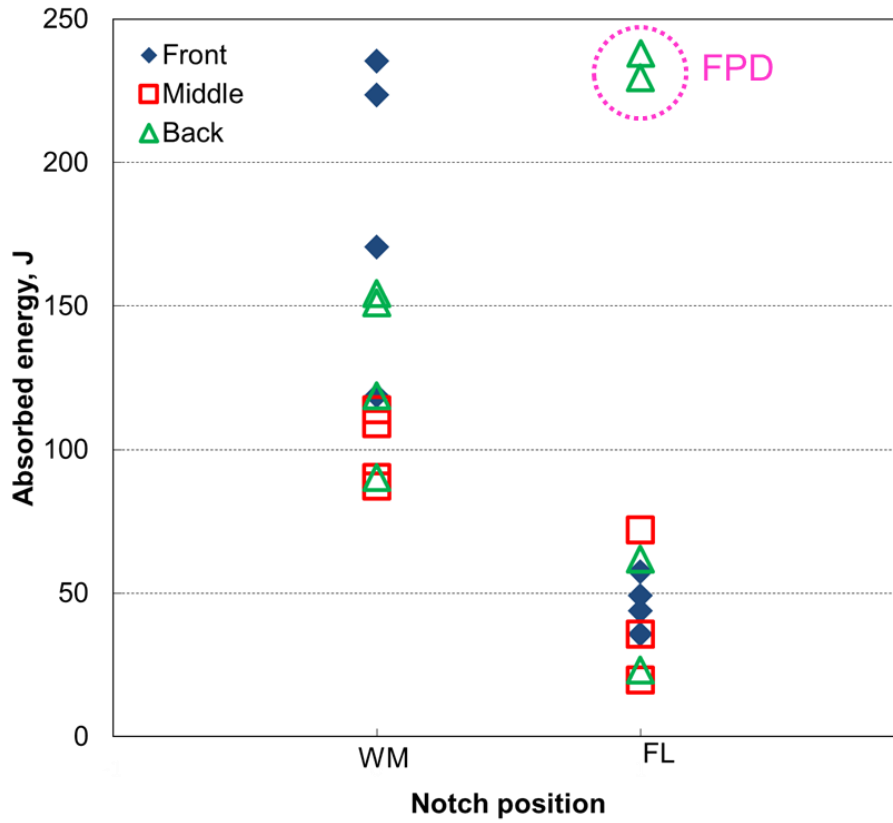
Fig. 5.17 Charpy impact test results at a test temperature of -20°C.

Notch Position: Weld metal, -20℃			
Front : 223.5 J Crack Direction: Straight		Front : 170.4 J Crack Direction: Straight	
Front : 235.2 J Crack Direction: Straight		Front : 118.6 J Crack Direction: Straight	
Middle : 113.8 J Crack Direction: Straight		Middle : 109 J Crack Direction: Straight	
Middle : 87.1 J Crack Direction: Straight		Middle : 90.2 J Crack Direction: Straight	
Back : 118.6 J Crack Direction: Straight		Back : 151 J Crack Direction: Straight	
Back : 90.2 J Crack Direction: Straight		Back : 154.2 J Crack Direction: Straight	

(a) Weld metal.
Fig. 5.18 Fracture surface and crack direction of test pieces.

(b) Fusion line.

Fig. 5.18 Fracture surface and crack direction of test pieces (continued).

Notch location:

FL-Middle (19.6 J)
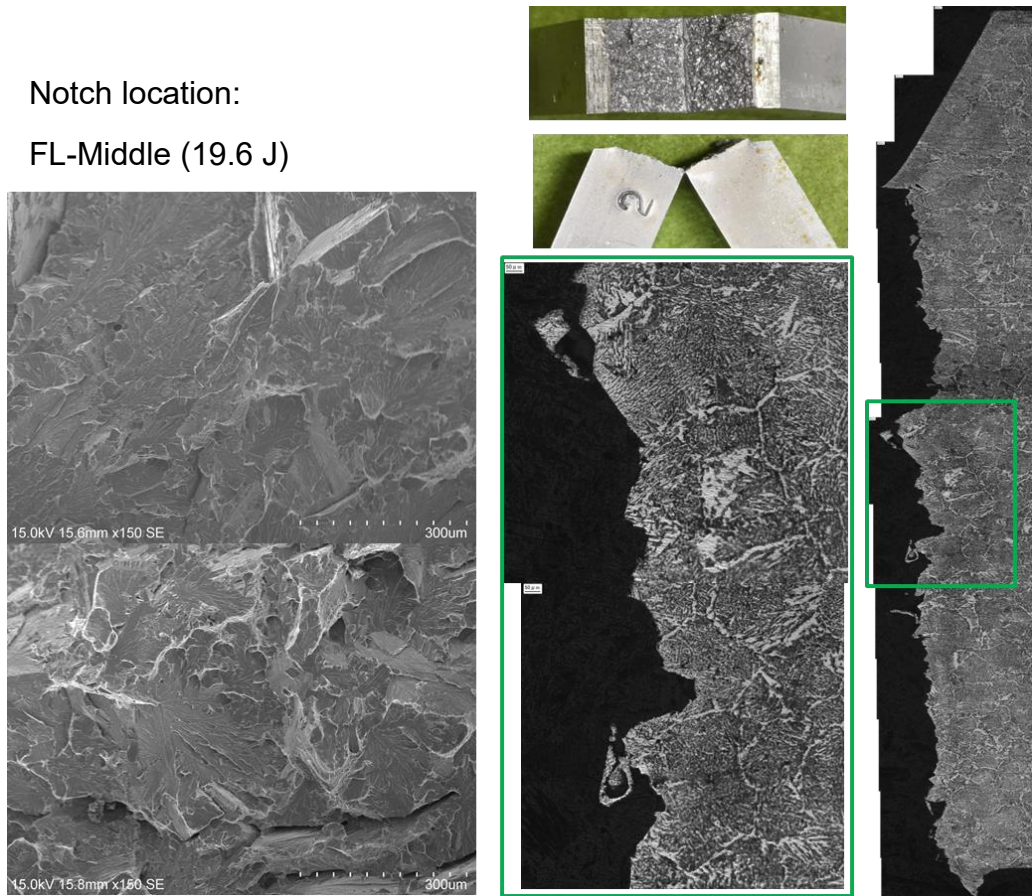
Fig. 5.19 Microstructure of fracture path and SEM of fracture surface in FL specimen.

5.4 Summary

Since limited power laser of a diode laser is 6 kW, the twin diode lasers and a hot-wire system was studied and applied to the heavy-thick joint with 50-mm thickness in the vertical direction. The results of optimizing power distribution and investigating welded joint properties can be drawn as follows:

1) The twin laser system with single hot-wire feeding was investigated power distribution on the heavy-thick groove. The large rectangular beam having high-edged energy was irradiated stably combined with either the narrow rectangular beam with weaving system or the stable large rectangular beam that could carry on the welding continuously until the end based on adequate the power distribution and hot-wire system.

2) The weld bead appearances showed complete penetration in both wire feeding side and back side without visible lack of fusion. Nevertheless, the cross-section of double stable laser beams showed very low dilution and narrow bead width and revealed the lack of fusion near the wire feeding side. Therefore, the stable beam with high-edged energy and the weaving beam of either 2-mm or 5-mm beam widths could keep stable molten pool and melt base metal. That could improve dilution on edges near plate surfaces and groove walls where the lack of fusion easily occurred in order to achieve a sound joint. Consequently, the novel single-pass vertical welding method can be applied to a heavy-thick joint and accomplish a high efficient method, the reductions in a total of laser power and heat input.

3) Microstructure revealed the narrow CGHAZ region of all welding conditions even the different weld dilution as a result of low heat input. The toughness results of notch location at weld metal showed a high mean value at -20^{0}C, but the fusion line obtained low average value as the faction ferrite could be found along with the fusion line.

Chapter 6

The application of single-pass vertical welding for Ni steel using hot-wire laser welding

6.1 Introduction

In recent years, the fabrication of the LNG fuel tank in the ships has been demanded increasingly instead of oil fuel in order to reduce SOx and NOx emissions. Due to the amount of heat energy for propulsion, its capacity is twice of the conventional fuel. Therefore, the LNG fuel tank capacity becomes larger. The materials such as aluminum, stainless steel (SUS304), 9%Ni and %7Ni steel are high resistant to low-temperature brittleness used for storing cryogenic which has a very low boiling point of -163 ^{0}C. The conventional welding process for a vertical joint is automatic TIG that employs multi-pass layers to fulfill a thick-welded joint. According to multi-pass welding, it spends a great deal of time in the construction and deteriorates welded joint properties. Thus, we would like to apply the novel vertical welding process using hot-wire laser welding method on Ni steel plate to cut down the time spent in multi-pass layers. Moreover, the heat input of the proposed welding process could achieve much less than that of a conventional single-pass vertical welding method, EGW and get an efficient welded joint.

The first part is the introduction of the methodology and joint configuration of the proposed welding process. The basic ideas in the Chapter 3 and the large size jig in the Chapter 4 are applied for the long-welded length of 7%Ni steel plate. The specimens in this study consist of three thicknesses 10 mm, 15 mm and 20 mm. To achieve a sound welded joint, the welding conditions such as a rectangular laser spot size, laser power, welding speed and so on are optimized. Then the welded joint appearances and cross-sections are observed to evaluate the effects of the heat from welding on the dilution in base metal, heat affected zone and microstructure.

The second part is to investigate the mechanical properties of welded joints of the proposed welding process such as hardness distribution, tensile test, and V-notch Charpy impact test compared with standard requirements.

85

6.2 Optimization of welding conditions for Ni steel plate using the proposed welding process

This part is to investigate welding conditions of the proposed welding process for Ni steel plate used as inner walls of the LNG storage tank. Because the thickness of LNG tanks in the field is variable regarding the capacity, in this experiment there are three different thicknesses of specimens such as 10, 15 and 20 mm which were employed to study the efficiency of the proposed welding process in several thicknesses.

6.2.1 Introduction of the joint configuration and welding conditions of the novel welding process for Ni steel plate
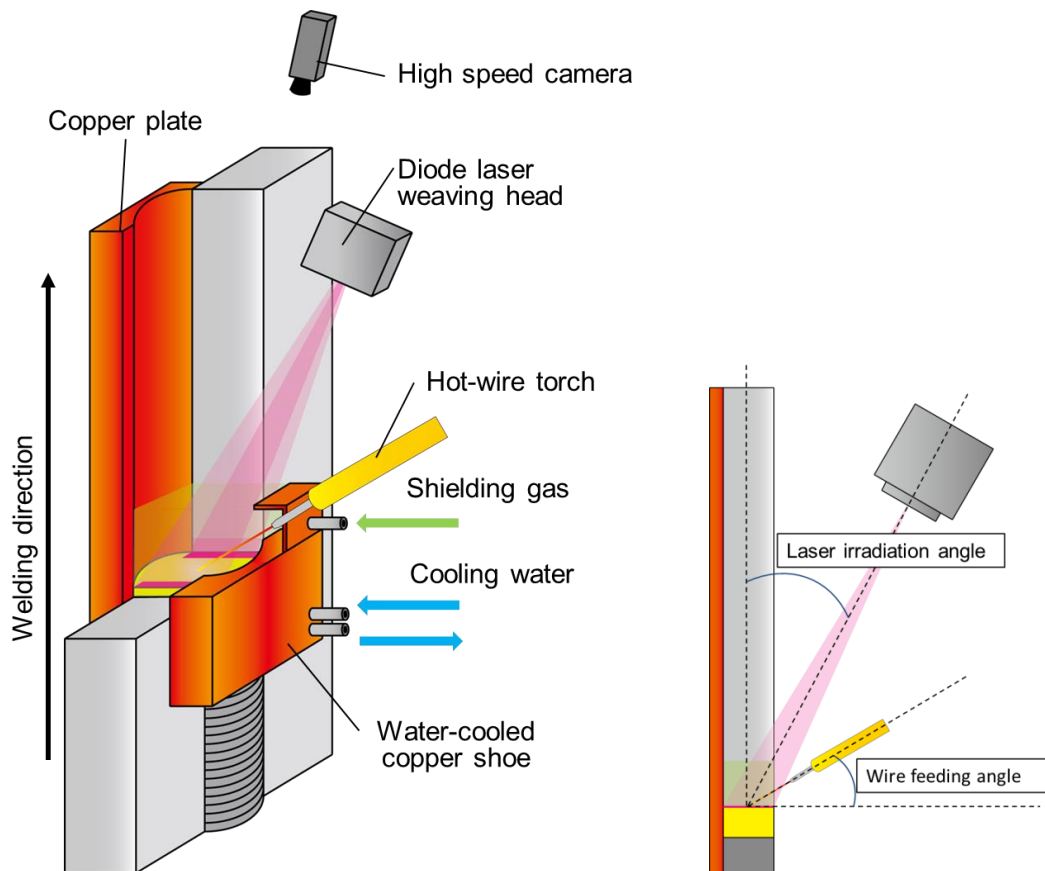
Fig. 6.1 Schematic layout of the large size jig of the proposed process.

In this experiment, test specimens were performed the long-welded length. Figure 6.1 shows the schematic layout of the joint configuration for the large-scale specimen. All of the equipment such as a laser power source, hot wire machine, a weaving system and so on follow in the Chapter 3. The two plates were set vertically. The hot wire and a diode laser with a weaving system were applied from the front side and the high-speed camera was attached to observe from the top side. All of them were moved vertically by a self-propelled system to control welding speed. A copper shoe kept the molten pool and supplied the shielding gas and cooling water inside.

6.2.1.1 In-situ observation

A high-speed image of the welding phenomena was captured by a high-speed camera. The pencil camera V-193-M1 model connected with NAC: MEMRECAM GX-5 module is shown in Fig. 3.5. A focus lens was 35 mm with a diameter of 25 mm and an 810-nm bandpass filter. The capturing parameters were the frame rate of 50 fps, shutter speeds of 1/1000 s and 1/2000 s, and closed aperture. Table 6.1 shows the monitoring condition. For setting a camera perspective to see the melting phenomena on the groove wall surfaces, it was perpendicular to groove wall surfaces and 80 degrees from the weld pool plane.
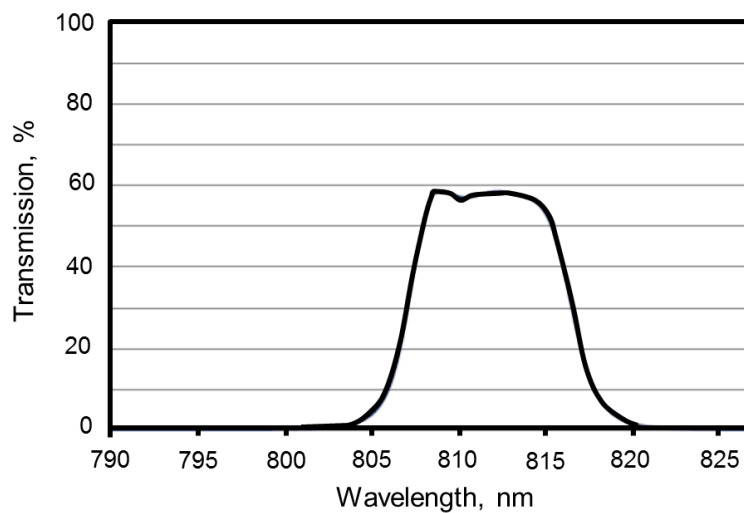
Fig. 6.2 Transmission curve of 810 nm bandpass filter.

Table 6.1 Monitoring conditions of in-situ observation.

High-speed camera	GX-5
Frame rate, fps	50
Aperture	Closed
Focus lens, mm	35
Band pass filter, nm/FWHM	810 / 10
Lighting	N/A
Shutter speed, s	1/1000, 1/2000

6.2.2 Materials used

7%Ni-TMCP steel plate was used as a base metal material. There are three thicknesses of 10, 15 and 20 mm as well as three different grades of A841 grade G Class 9, Class 10 and SL7N590 respectively. However, all grades are the 7%Ni-TMCP steel having similar chemical compositions as shown in Table 6.2 and the difference in the standard requirement and mechanical property range. The size of the specimen is shown in Fig. 6.3 having dimensions of 250w x 500h mm. Plates were fixed and aligned as a vertical joint configuration. The square groove was set with a 10-mm gap using a bottom spacer having dimensions of 10 (width) x 20 (height) x 10, 15 and 20 mm (depth). YGT9Ni-2 with a diameter of 1.2 mm was deposited as hot-wire filler wire and its chemical composition is shown in Table 6.2.

Table 6.2 Chemical compositions of base metal and filler wire.

Materials	Chemical Composition, wt%											
	C	Si	Mn	P	S	Al	Cu	Ni	W	Cr	Mo	Fe
A841 Gr.G Class 9	0.05	0.07	0.98	0.003	-	-	-	6.33	-	Add	Add	Bal.
A841 Gr.G Class 10	0.05	0.07	0.98	0.003	-	-	-	6.33	-	Add	Add	Bal.
SL7N590	0.05	0.07	0.98	0.003	0.0003	-	-	6.32	-	Add	Add	Bal.
YGT9Ni-2	0.02	0.08	0.07	0.001	0.001	-	0.8	75.1	3.1	-	19.7	1.0

Fig. 6.3 Specimen dimensions of 7%Ni steel.

6.2.3 Experimental procedure

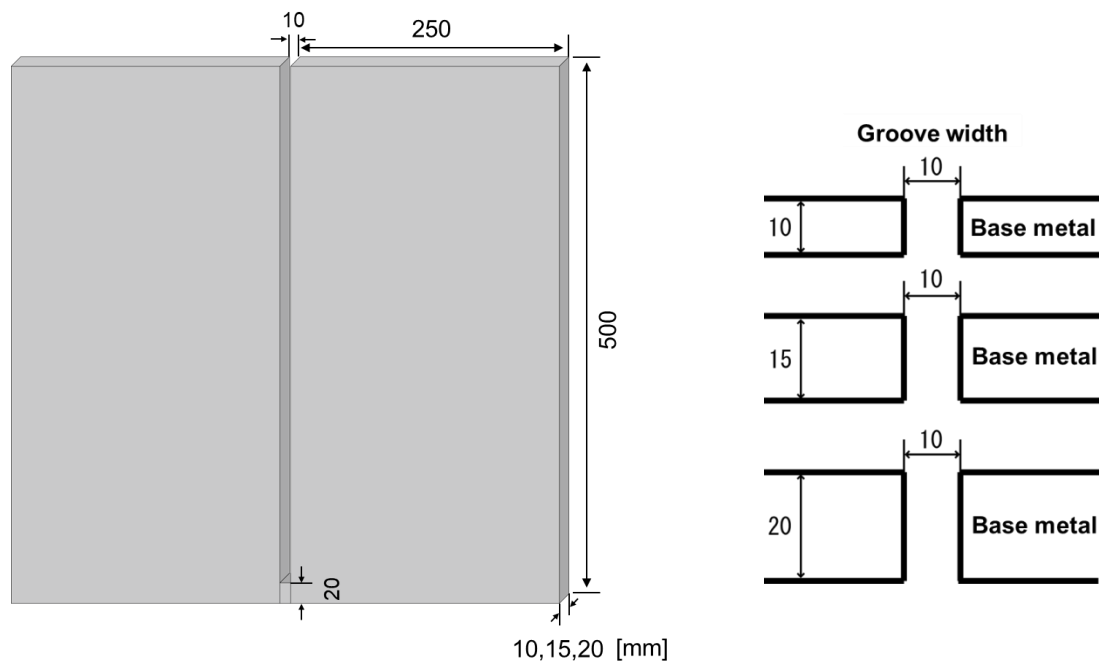There are three welding conditions regarding the thickness of specimen varied in 10, 15 and 20 mm. The welding parameters of the proposed welding process should be considered to optimize power density. A laser spot beam, laser power, and welding speed should be adjusted properly when the thickness changes. In this experiment, we have already optimized the welding conditions of three specimens.

For 10-mm thickness, Table 5.3 shows the optimal welding conditions used for large size jig of 10-mm thickness. The laser power of 4.5 kW with a welding speed of 6.7 m/min was used. The argon shielding gas with 30-l/min flow rate was used. The previous study in applying the weaving system obtained better dilution in base metal and less lack of fusion. Therefore, the laser head of 0.4-mm fiber core was assembled with a collimator lens of 80 mm, focus lens of 400 mm and homogenizer of LL2.85 to create 2x11 mm rectangular laser beam at just focus. 11-mm length of laser spot fitted the thickness of specimen and the weaving system of 5-Hz exponential waveform was applied. The laser spot beam on the groove area is shown in Fig. 6.4 (a).

Table 6.3 Welding parameters for 10-mm 7%Ni steel.

Gap width size, mm	10
Laser type	Diode laser
Fiber core, mm	0.4
Collimator, mm	80
Homogenizer	LL2.85
Focus lens, mm	400
Laser power, kW	4.5
Laser irradiation angle, degree	15°
Defocus, mm	0
Spot size, mm x mm	2^w x 11^l
Laser distribution type	Uniform distribution
Weaving frequency, Hz	5
Weaving waveform	Exponential waveform
Filler wire diameter, mm	1.2
Welding speed, cm/min	6.7 (4m/h)
Wire feed speed, m/min	9.53
Wire current, A	89
Wire feeding angle, degree	45
Shielding gas, 30 l/min	Ar
Pre-irradiation time, s	90

For 15-mm thickness, Table 6.4 shows the optimal welding conditions used for large size jig of 15-mm thickness. The laser power of 6 kW with a welding speed of 6.7 m/min was used. The argon shielding gas with 30-l/min flow rate was used. The previous study in applying the weaving system obtained better dilution in base metal and less lack of fusion. Therefore, the laser head of 1-mm fiber core was assembled with a collimator lens of 100 mm, focus lens of 400 mm and homogenizer of LL2.54 to create 4x17 mm rectangular laser beam at just focus. 17-mm length of laser spot fitted the thickness of specimen and the weaving system of 5-Hz exponential waveform was applied. The spot beam on the groove area is shown in Fig. 6.4 (b).

For 20-mm thickness, Table 6.5 shows the optimal welding conditions used for large size jig of 20-mm thickness. The laser power of 6 kW with a welding speed of 4.17 m/min was used. The shielding gas of argon with 30-l/min flow rate was employed. The previous study in applying the weaving system obtained better dilution in base metal and less lack of fusion. Therefore, the laser head of 1 mm fiber core was assembled with a collimator lens of 100 mm, focus lens of 400 mm and homogenizer of LL2.35 to create 4x26 mm rectangular laser beam at just focus. 26-mm length of laser spot fitted the thickness of specimen and the 5-Hz exponential waveform was applied. The spot beam on the groove area is shown in Fig. 6.4 (c).

Table 6.4 Welding parameters for 15-mm 7%Ni steel.

Gap width size, mm	10
Laser type	Diode laser
Fiber core, mm	1
Collimator, mm	100
Homogenizer	LL2.54
Focus lens, mm	400
Laser power, kW	6
Laser irradiation angle, degree	15°
Defocus, mm	0
Spot size, mm x mm	4^w x 17^l
Laser distribution type	Uniform distribution
Weaving frequency, Hz	5
Weaving waveform	Exponential waveform
Filler wire diameter, mm	1.2
Welding speed, cm/min	6.7 (4m/h)
Wire feed speed, m/min	14.1
Wire current, A	105
Wire feeding angle, degree	45
Shielding gas, 30 l/min	Ar
Pre-irradiation time, s	90

Table 6.5 Welding parameters for 20-mm 7%Ni steel.

|	
Gap width size, mm	10
Laser type	Diode laser
Fiber core, mm	1
Collimator, mm	100
Homogenizer	LL2.35
Focus lens, mm	400
Laser power, kW	6
Laser irradiation angle, degree	15°
Defocus, mm	0
Spot size, mm x mm	4^w x 26^l
Laser distribution type	Uniform distribution
Weaving frequency, Hz	5
Weaving waveform	Exponential waveform
Filler wire diameter, mm	1.2
Welding speed, cm/min	4.17 (2.5 m/h)
Wire feed speed, m/min	11.8
Wire current, A	91.6
Wire feeding angle, degree	45
Shielding gas, 30 l/min	Ar
Pre-irradiation time, s	90
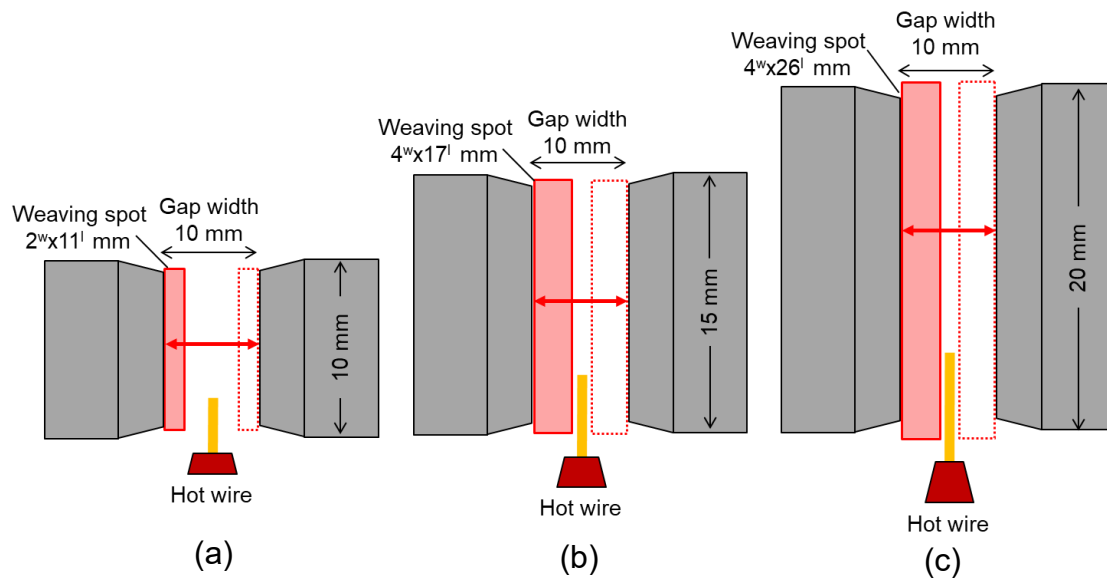
Fig. 6.4 Schematic layout of weaving laser spot placed on gap area of 7%Ni steel specimens (a) 10-mm (b) 15-mm and (c) 20-mm thicknesses.

6.2.4 Welding performing of Ni steel specimens and weld bead appearances

The experimental setup of the proposed welding process for Ni steel plate is shown in Fig. 6.5. The photograph shows that the plates were set vertically with a square groove having a 10-mm gap. The test specimen was placed on a back-side copper plate on the large-size jig and was fixed by clamp locks. To protect the gap shrinkage during welding, the spacer of 10-mm thickness was inserted on the top of the groove. This jig was similar to EGW. It was accessible from only the front side. The self-propelled unit carried a laser head, a hot-wire torch, a copper shoe, and a high-speed camera to move together along a guide rail. The copper shoe was cooled by water flow inside to form a weld bead in the front side and it supplied shielding gas to protect the weld pool. The high-speed camera was used to observe weld pool phenomena on the top of the self-propelled unit and its parameter was shown in Table 6.1.
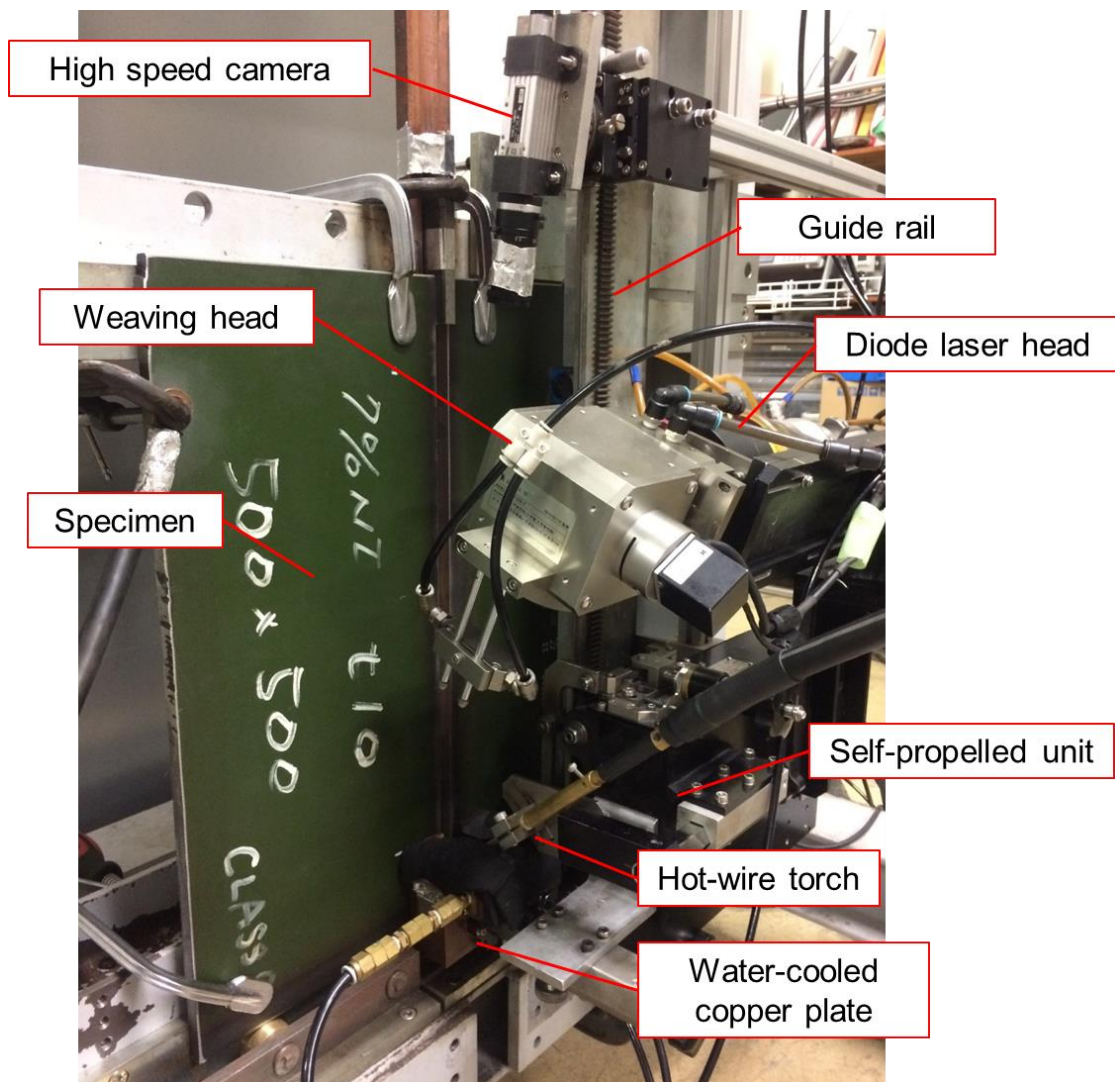

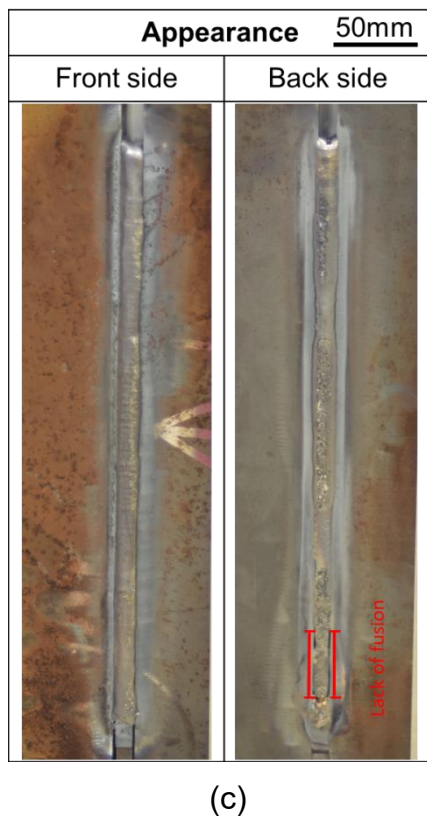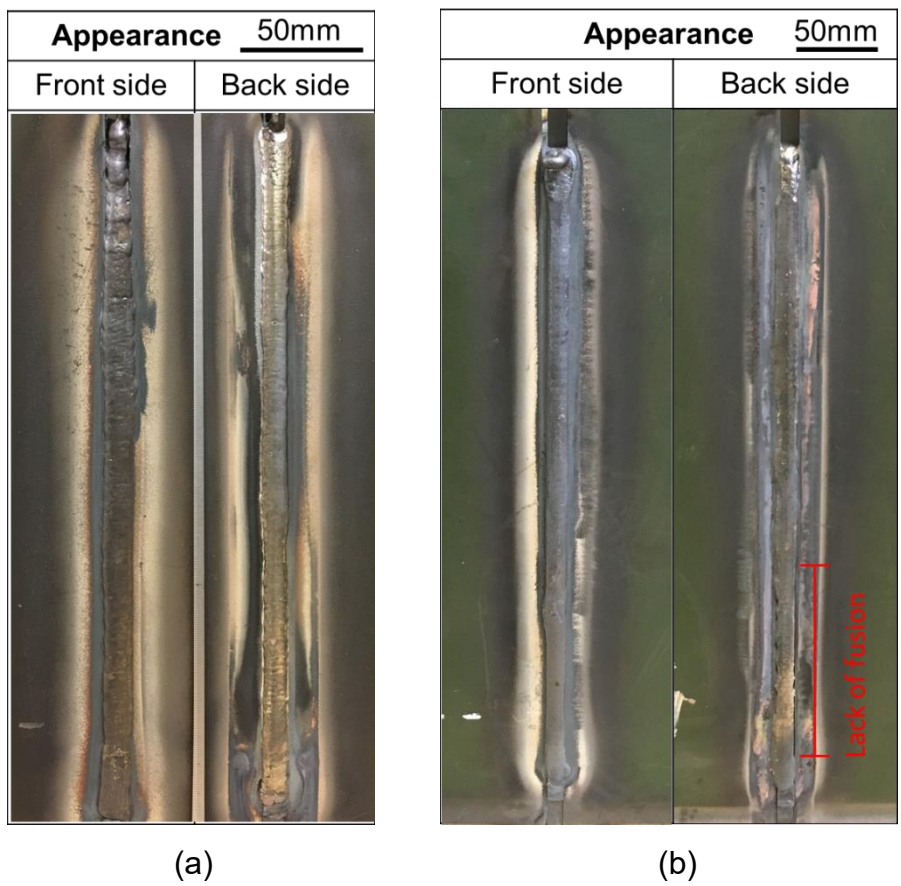Fig. 6.5 A photograph showing the experimental set up using the proposed process.

(a)

(b)

(c)

Fig. 6.6 Weld bead appearance of 7%Ni steel welded joints (a) 10 mm
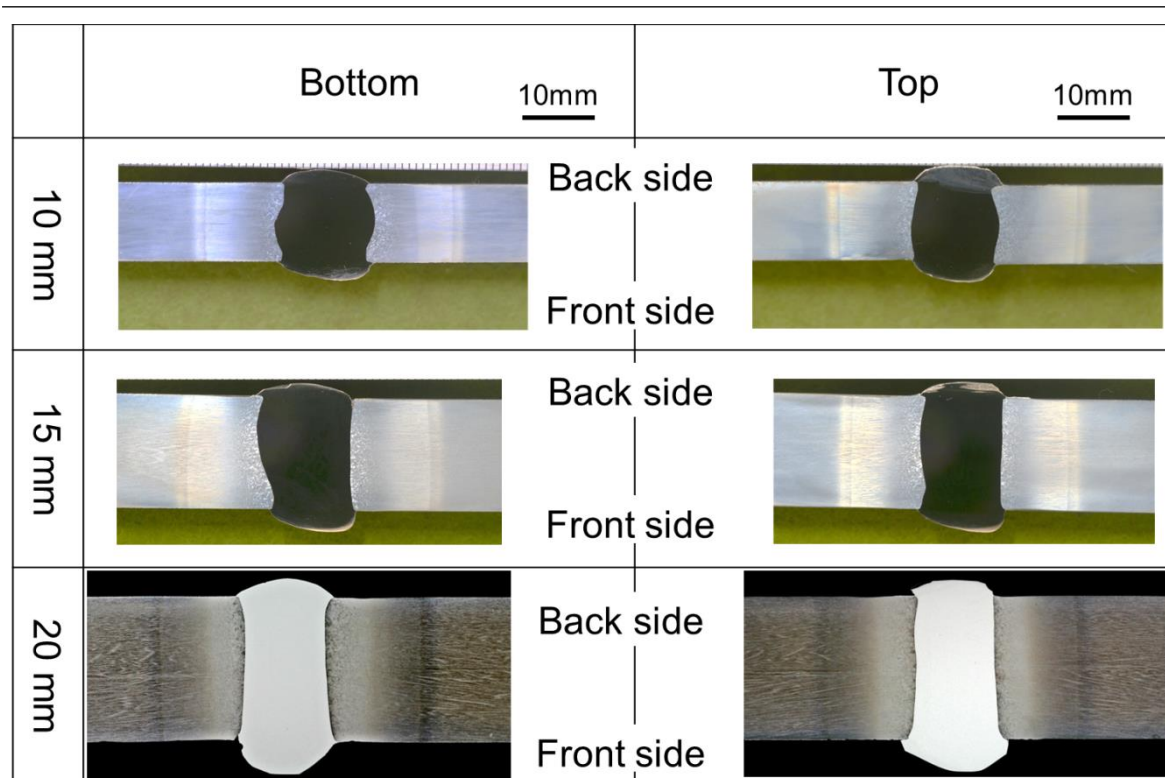(b) 15 mm (c) 20 mm.

Fig. 6.7 Marco cross-sections of 7%Ni steel welded joints.

Figure 6.6 shows the weld bead appearances of 7% Ni steel specimens performed by the proposed welding process with the large size jig. The long-welded joints with changing the thickness of the specimen were investigated. Fig. 6.6(a) shows the weld bead appearance of 10-mm thickness. The weld bead achieves full penetration of both sides without visible lack of fusion and the weld bead is smooth and sound, but in the top of the specimen it had a trouble of hot-wire feeding during welding. Fig. 6.6(b) shows the weld bead appearance of 15-mm thickness. The weld bead shows the obvious lack of fusion on the back side in the first period of welding start because unstable weld pool phenomena could occur when a hot-wire rod was fed into the molten pool of pre-irradiation in a weld groove, the molten pool flowed turbulently for a while thereafter the molten pool became stable. The weld bead is then smooth and sound. There is no visible lack of fusion and it obtains full-filled penetration. Fig. 6.6(c) shows the weld bead appearance of 20-mm thickness. The weld bead indicates the a little lack of fusion on the back side in the first period which is similar the problem to 15-mm specimen.

Figure 6.7 shows the macro cross-sections of 7%Ni steel welded joints using the proposed welding process. The cross-sections were cut from the bottom and top of each specimen. The top cross-section of specimens shows less dilution than the bottom cross-section due to the heat accumulation and heat distribution during welding. All cross-sections reveal sound joints without lack of fusion inside the welded joints. However, some cross-sections at the bottom of 15-mm and 20-mm specimens indicate small lack of fusion on the edge.

6.2.5 In-situ observation on the molten pool by a high-speed camera

Refer to the Chapter 3 and 4, a narrow rectangular beam with a weaving system could optimize the power density distribution and higher dilution was achieved in this beam than in a stable large rectangular beam. As shown in Fig. 6.8, the weaving motion of 5 Hz-exponential waveform is used. In one cycle, the weaving beam is held on each groove surface about 72.5 ms and moving time between each groove surface is about 27.5 ms, so the average energy density on near the groove surfaces is much higher than on the middle of the groove.
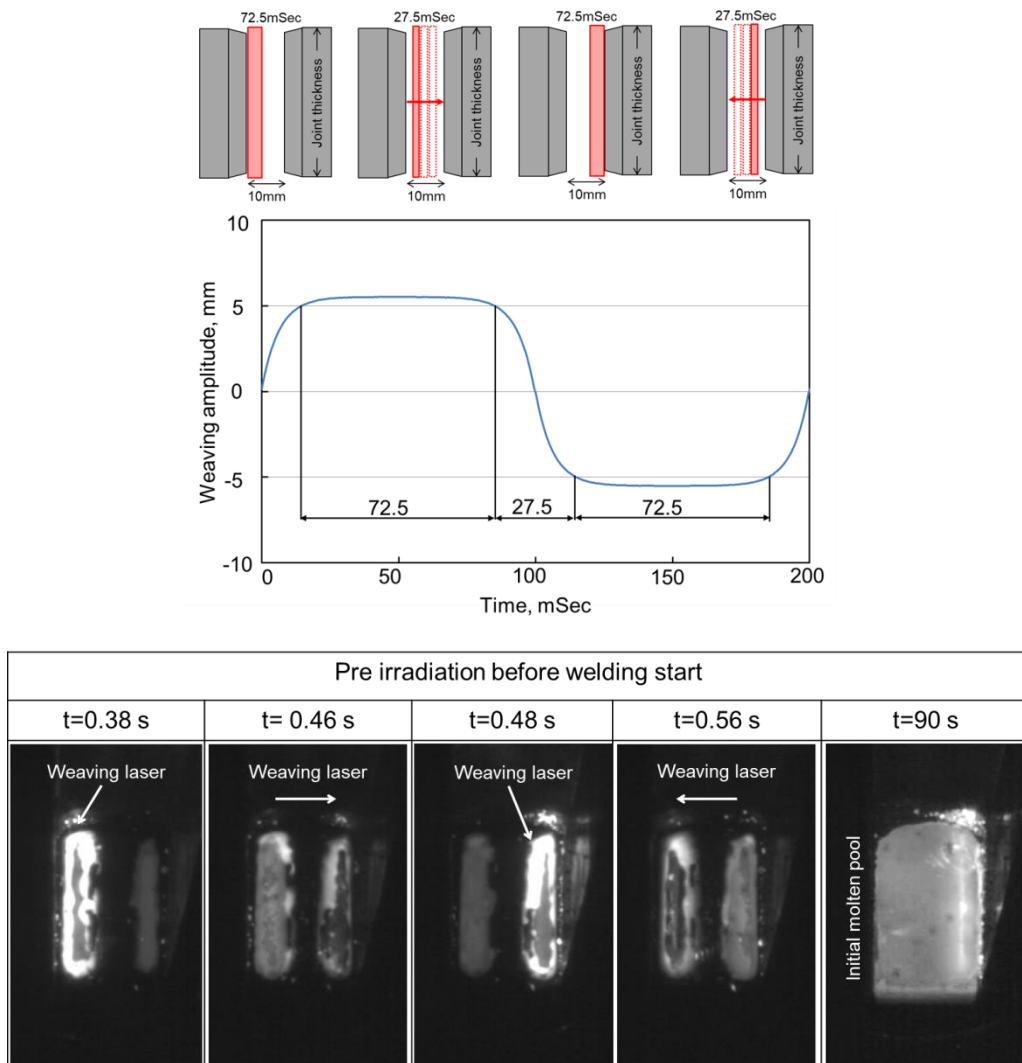
Fig. 6.8 Schematic layout of laser motion at 5 Hz exponential waveform and an example of high-speed images in pre-irradiation.

Before hot-wire feeding the weaving beam was irradiated into the groove area on a spacer surface to create an initial molten pool for 90 s because a large amount of the weld metal volume was deposited and the molten pool by pre-irradiation could help to melt and distribute the filler wire steadily. Figure 6.8 shows an example of

high-speed images in pre-irradiation. For instance, the 0.38 s image shows the weaving laser held on a groove surface. In the 0.46 s, the weaving laser is moving to the other side and then the 0.48 s image shows the weaving laser held on the other side. This laser spot motion repeats during welding. The 90 s image shows the stable molten pool by pre-irradiation before hot-wire feeding on the whole groove area.

Figure 6.9 shows a schematic layout and high-speed images of a weld pool during welding of 10-mm, 15-mm and 20-mm specimens. The hot wire was fed into the molten pool and moved vertically in the upward direction. The steady weld pool formation and wire feeding were observed continuously for the whole welding period in all of three welding conditions. The single hot-wire feeding could be deposited the weld metal sufficiently. As a result, the sufficient weld penetration could be achieved both on the back side and the wire feeding side.
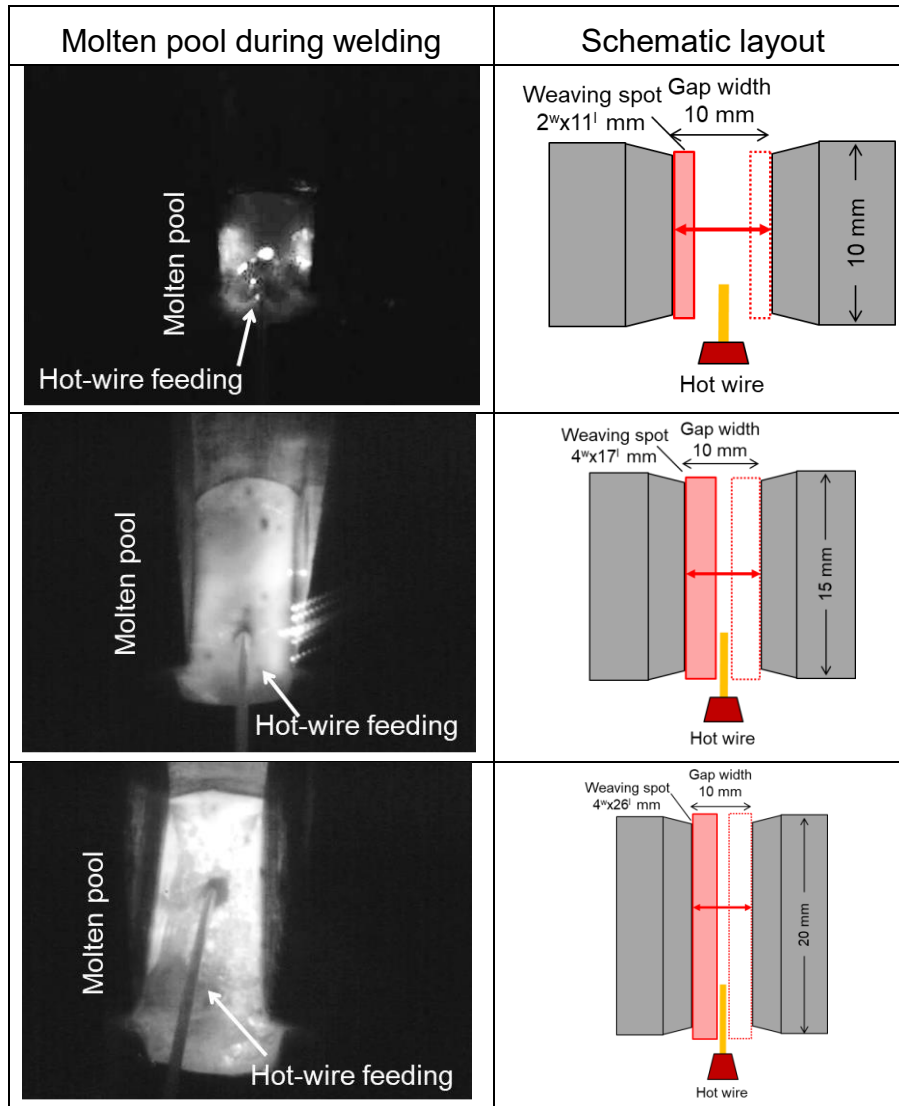

Fig. 6.9 Schematic layout and high-speed images of the proposed process during welding of 7%Ni steel specimens 10mm, 15mm, and 20mm thickness.

6.2.6 Evaluation of macrograph and heat input of welded joints

Figure 6.10 shows the macro cross-sections of 7% Ni steel welded joints of the proposed welding process. According to the top cross-section of each specimen in a stable welding period, the cross sections having different thicknesses such as 10 mm, 15 mm and 20 mm illustrate complete weld penetration which is achieved on both of wire feeding side and the opposite side. Any imperfections are not observed and low dilution is achieved in all welded joints as shown in Fig. 6.10. These joints could derive small distortion from low dilution even though a heat input of the proposed process is higher than that of the conventional TIG welding process due to using the single-pass welding joint in the proposed process.

The measured weld bead widths of three cross-sections from the wire feeding side to the back side are shown in Fig. 6.11. The gap of specimens was set with 10 mm. The results show that the penetration depth of both groove surfaces is rather small and not higher than 2 mm. The smallest width appeared to groove edges where the lack of power density occurs. Additionally, on the wire feeding side filler wire cut the laser beam above that causes the actual-low laser power density.

Then, the heat input of the proposed process is calculated simply by using only the heating from laser power as a heat source, not including a small effect of the hot-wire system. The equation hereby is (laser power (kW)/welding speed (cm/min))*60 and the heat input was calculated at the maximum value with the efficiency factor of 100%. The results are plotted in graph to show the relationship between an amount of heat input and thickness plate as shown in Fig. 6.12 as follows 40, 54 and 86 kJ/cm respectively. Regarding increasing thickness, the heat input is rise optimally in a linear relationship and the approximate value of the heat input per thickness of the proposed process is about 4 (kJ/cm.mm).
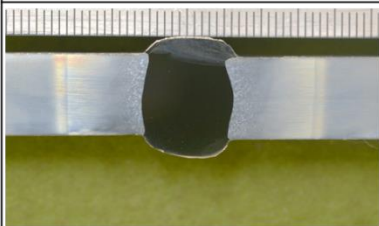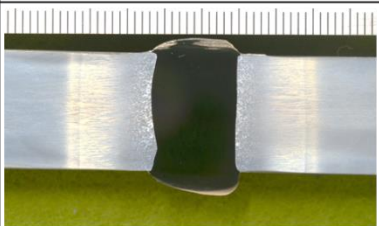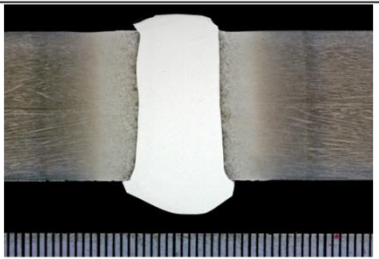
7% Ni, 10 mm	7% Ni, 15 mm	7% Ni, 20mm
Wire-feeding side	Wire-feeding side	Wire-feeding side
Lack of fusion ratio, %		
0	0	0
Dilution ratio, %		
10.3	10	7.6
HAZ width, mm		
13	12	14

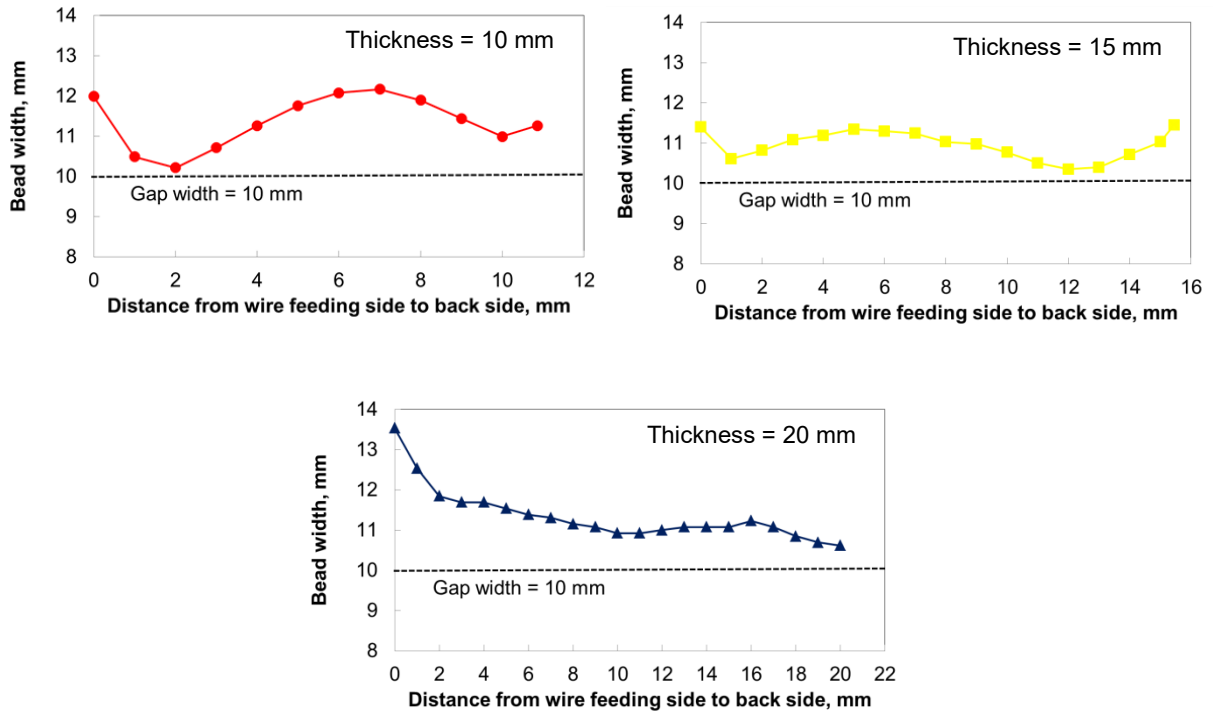Fig. 6.10 Top-side macro cross-section analysis of three specimens.

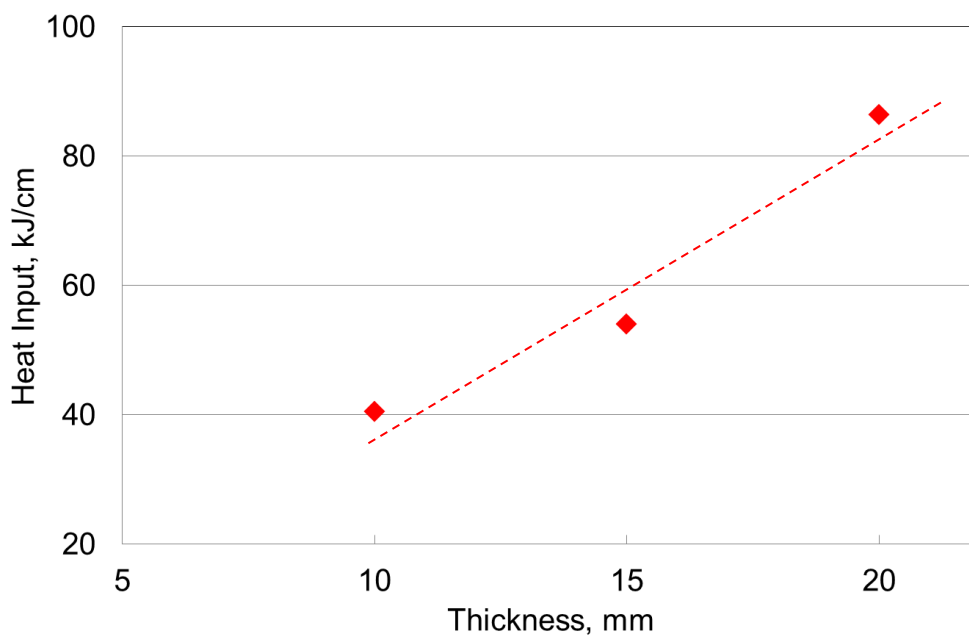Fig. 6.11 Measured bead width on the cross-sections of three specimens.

Fig. 6.12 A quantity of heat input of the proposed process on thicknesses

6.3 The properties of 7%Ni steel welded joints using the proposed process

This part presents the results of welded joint properties of 7% Ni steel plate using the proposed welding process. In the stable welding state of long-welded specimen, we obtained complete-full penetration without imperfections and then that was investigated in microstructure, hardness distribution, tensile test, and Charpy V-notch impact test.

6.3.1 Microstructure characteristics of the welded joints.

The cross-sections of 7%Ni steel welded joint with filer wire of 75% Ni-base alloy was polished firstly by various grit sizes of sandpaper number 100, 500, 1200, 2000 and 3000 in order and then secondly by diamond paste with a particle size of 6, 1 µm and magnesium oxide (MgO) powder. There are two etching procedures; first, it was etched by 3% Nital solution to reveal the microstructure of HAZ and second, according to 75% Ni of filler wire etched by electro-etching, 10V with 10% oxalic acid was employed to reveal the microstructure of weld metal observed by optical microscopic (1LM21 lasertec).

Figure 6.13 shows the weld metal microstructure of 7%Ni welded joint. According to the filler wire material of 75%Ni-20%Mo (YGT9Ni-2), its microstructure can indicate the weld metal solidification with columnar dendrite and find equiaxed dendrite.

Figure 6.14 shows the FL and HAZ microstructure of the 20-mm-thick welded joint and its chemical composition of 7% Ni steel is shown in Table 6.2. FL and FL+1 images of CGHAZ region, it consists of the coarsened microstructure of prior austenite grains and martensite laths. On the other hand, the FL+3 and FL+5 images indicated that the fine prior austenite gains and the martensite laths.
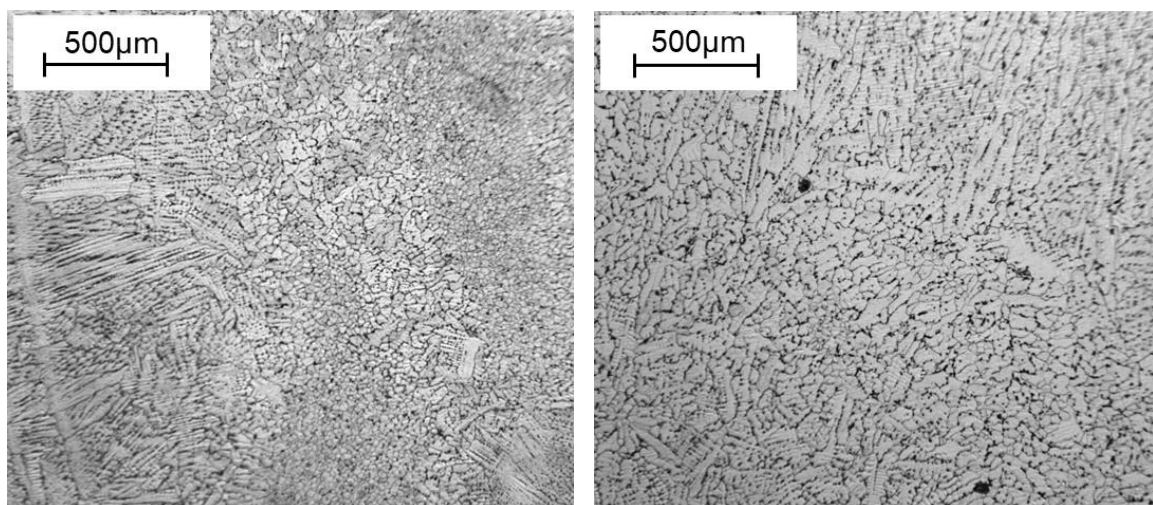
Fig. 6.13 Weld metal microstructure of the 7%Ni steel welded joint.
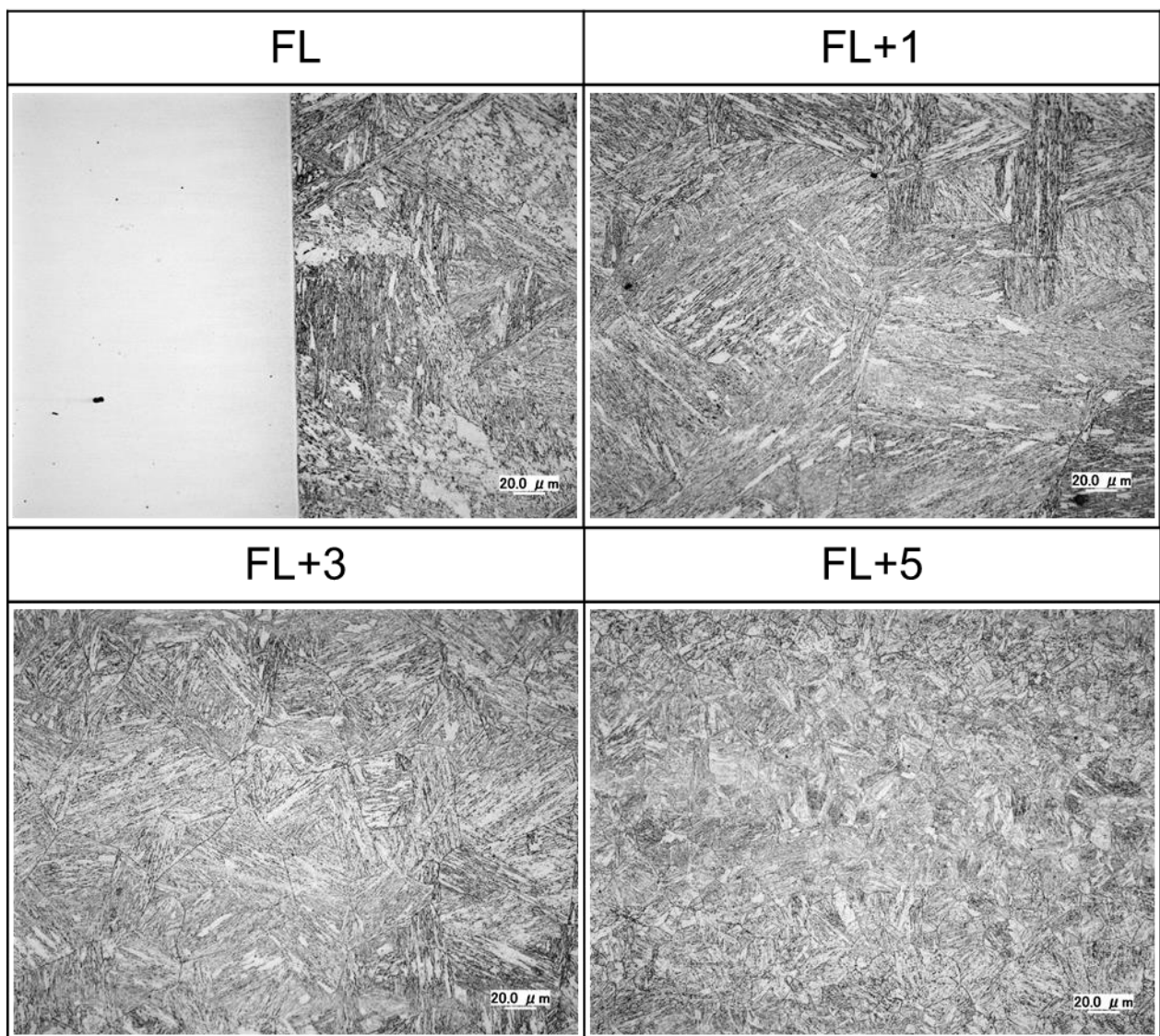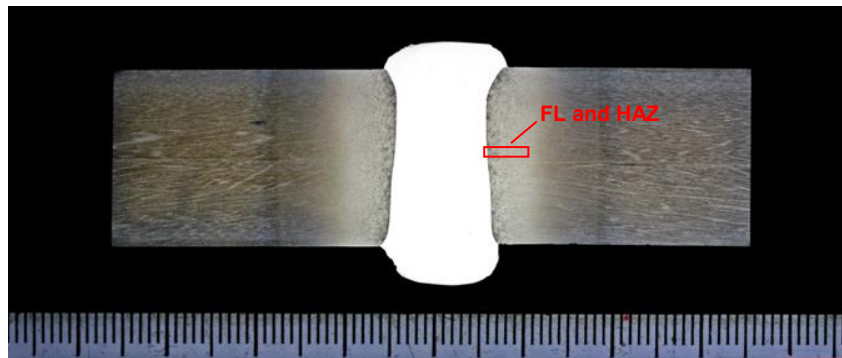
Fig. 6.14 Microstructure of fusion line and heat affected zone in the 20-mm thickness of the 7%Ni steel welded joint.

6.3.2 Hardness distribution of the welded joints

Micro Vickers hardness testing of the specimens follows the method in 4.4.1 and the hardness of weld metal, heat affected zone and base metal are measured in accordance with JIS Z 2244.

7% Ni steel welded joint	Hardness distribution
10 mm	
15 mm	
20 mm	
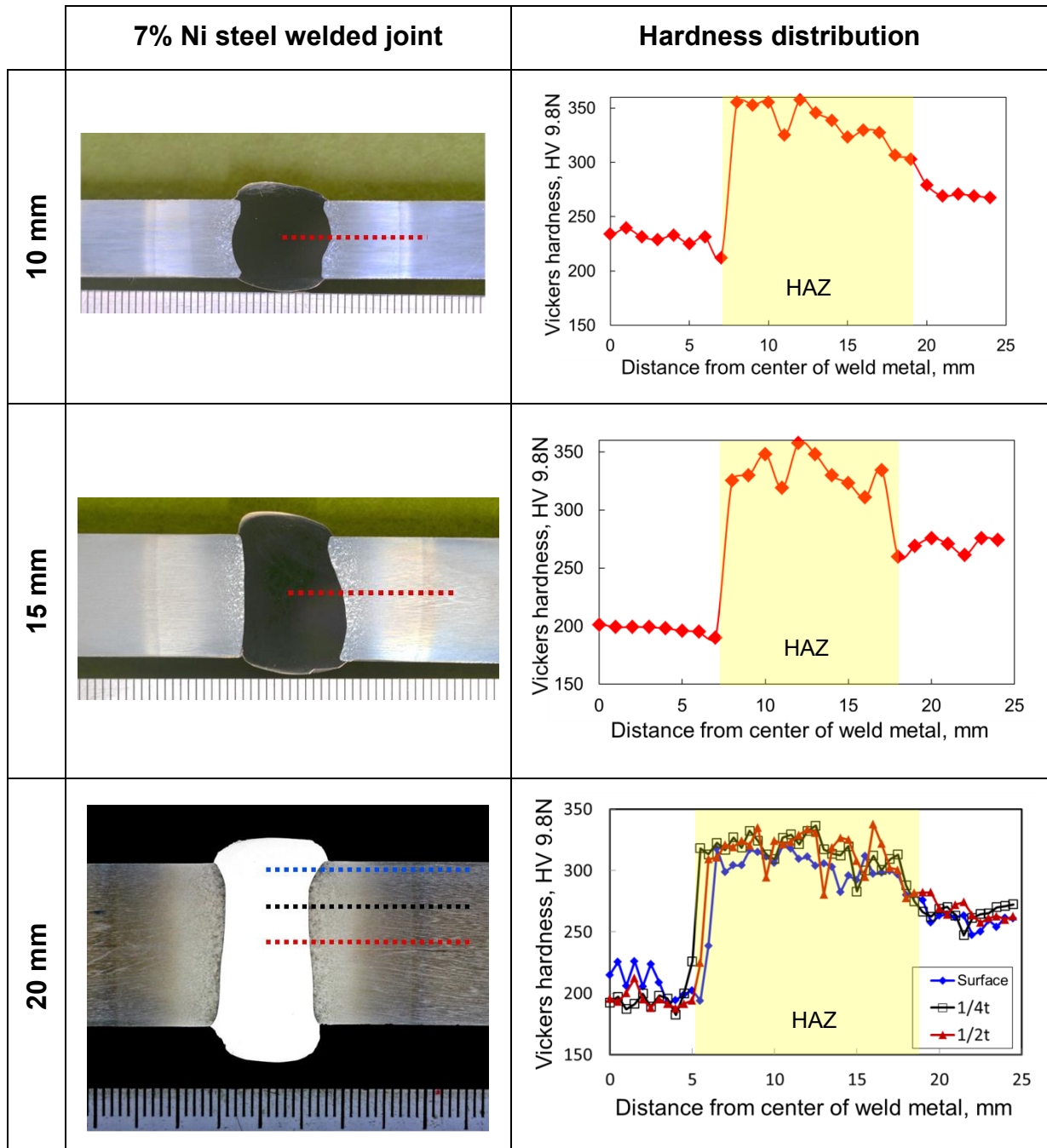
Fig. 6.15 Vickers hardness distribution of the 7%Ni steel welded joints.

Figure 6.15 shows the hardness distribution through the base metal, heat affected zone and weld metal of three specimens. The cross-sections of 10 mm and 15 mm were measured the hardness on the middle of thickness; however, the 20-mm cross-section was measured in three locations such as near a surface, a quarter of thickness and a half of thickness. The results show the same hardness distribution in all the welded joints based on their microstructures. The base metal of 7%Ni steel has the mean hardness of 270 HV and the mean weld metal hardness of 210 HV is softer than that of the base metal because the filler wire material strength is less than the base metal strength. The high hardness degree in the HAZ was 330 HV due to the martensite structure and the hardened widths of the HAZ are about 13, 12 and 14 mm respectively.

6.3.3 Tensile test of the welded joints

Figure 6.16 shows the tensile test specimen of three-thickness welded joints. Each thickness was prepared with 2 tensile test coupons. Figure 6.16 a) shows the tensile specimens of 10-mm welded joint. After machining, the actual thicknesses were 8.8 and 8.6 mm and their cross-sectional areas were 2.22×10^{-4} and 2.17×10^{-4} m^2 in order. Figure 6.16 b) shows the tensile specimens of 15-mm welded joint. The tensile test coupons had the actual thicknesses of 14.1 and 14.1 mm and their cross-sectional areas were 3.53×10^{-4} and 3.53×10^{-4} m^2 in order. Figure 6.16 c) shows the tensile specimens of 20-mm welded joint. The tensile test coupons had the actual thicknesses of 19.3 and 19.2 mm and the cross-sectional areas were 4.86×10^{-4} and 4.76×10^{-4} m^2 in order.

Specimen name	7%Ni_thk10mm_1	7%Ni_thk10mm_2
t, mm	8.8	8.6
h, mm	25.2	25.2
Cross-sectional area, m^2	2.22×10^{-4}	2.17×10^{-4}
Testing rate, mm/min	2	2
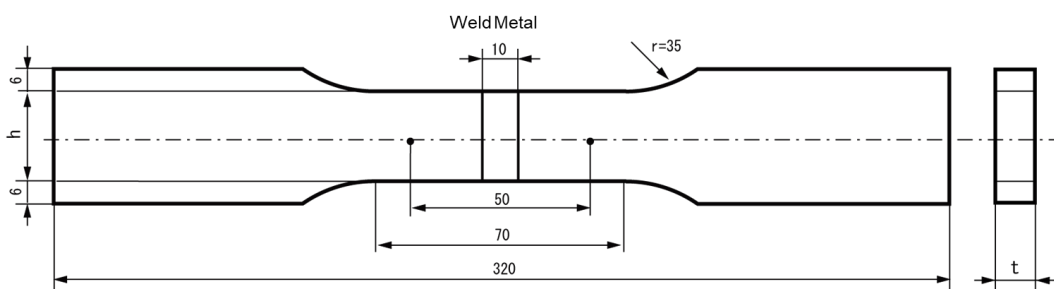
a) 10-mm specimen.

Fig. 6.16 Tensile test specimens of the 10, 15 and 20 mm welded joint.

Specimen name	7%Ni_thk15mm_1	7%Ni_thk15mm_2
t, mm	14.1	14.1
h, mm	25	25
Cross-sectional area, m^2	3.53x10^{-4}	3.53x10^{-4}
Testing rate, mm/min	2	2
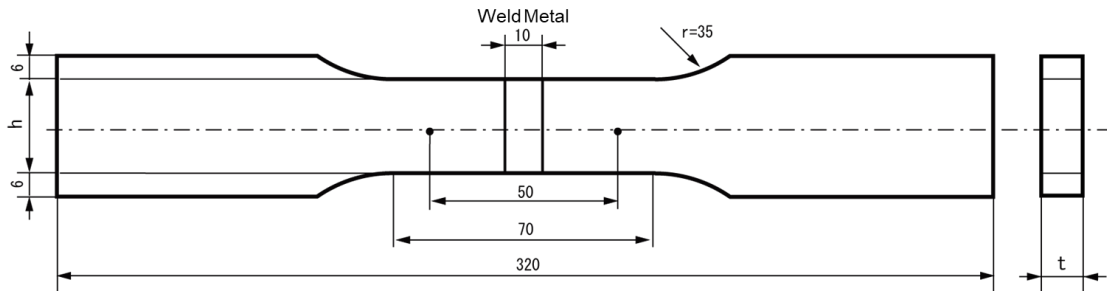
b) 15-mm specimen.

Specimen name	7%Ni_thk 20mm_1	7%Ni_thk 20mm_2
t, mm	19.3	19.2
h, mm	25.2	24.8
Cross-sectional area, m^2	4.86 x10^{-4}	4.76 x10^{-4}
Testing rate, mm/min	2	2
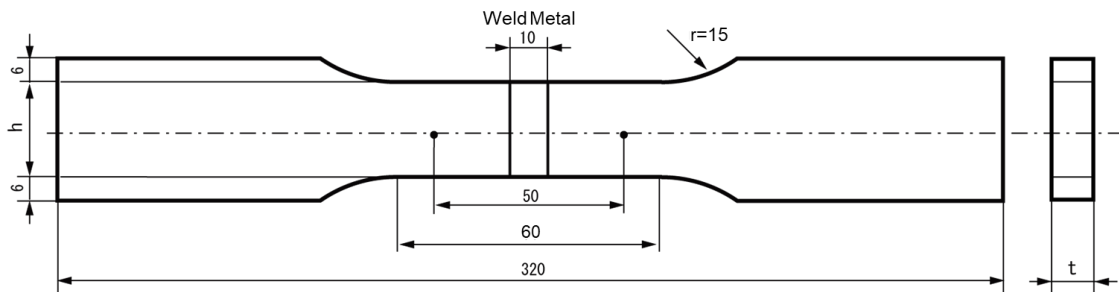
c) 20-mm specimen.

Fig. 6.16 Tensile test specimens of the 10, 15 and 20 mm welded joint (continued).

The tensile test results are shown in Table 6.6 and photographs and stress-strain curves are exhibited in Figure 6.17. There are 2 tensile specimens in each thickness. All specimens are broken at weld metal as the filler wire's strength is less than the base metal's strength. In the 10-mm welded joint, the tensile strength is 690, 691 MPa. In 15-mm welded joint, the tensile strength is 756, 737 MPa and the 20-mm welded joint have the tensile strength of 800, 794 MPa. Therefore, all of the test coupons meet the requirement having the tensile strength more than the specification of the filler wire material.

Regarding the breaking point in the weld metal where the material is softer. As shown in the photograph specimens, in the 10-mm and 15-mm specimens, the plastic deformation only occurs in the weld metal, so the elongation after fracture became low. Accordance to the tensile strength results, even though the entire welded joints are broken in the weld metal, 10-mm specimen obtains less tensile strength than that of 15-mm and 20-mm specimens and the tensile strength is less in the 15-mm specimen than in the 20-mm specimen. Soft/Hard ration in the weld metal could be studied because the welded joints have the same gap width as 10 mm, but different thicknesses. Soft/Hard ratio in weld metal can be defined in equation (6.1). A surface area of weld metal (soft) is divided by a cross-sectional area of base metal (hard). However, the joints are set with a square groove. The gap width divided by thickness can be applied in these joints and the result is shown in Table 6.7. The 10-mm specimen has the highest Soft/Hard ration of 1, the 15-mm specimen of 0.67 and the-20 mm specimen of 0.5 in order that results in the tensile strength of the welded joint. Consequently, in case the weld metal is softer than the base metal, the high Soft/Hard ratio would behave low tensile strength because that is able to have the weld metal easily plastically deformed.

Table 6.6 Tensile test results.

Specimen name	7%Ni_10 mm	7%Ni_15 mm	7%Ni_20 mm
Thickness, mm	8.8, 8.6	14.1 , 14.1	20, 19
Tensile strength, MPa	690, 691	756, 737	800, 794
Elongation after fracture, %	16, 14	12, 10	20, 19
Specification			
Base metal	A 841 G Cl9 (690 – 825 MPa)	A841 G Cl10 (750 – 885 MPa)	SL7N590 (690 – 830 MPa)
Filler wire	YGT9Ni-2 (660 min. MPa)		

$$\text{Soft/Hard ratio} = \frac{\text{Weld surface area (soft)}}{\text{Cross sectional area (hard)}} = \frac{\text{Gap x h}}{\text{t x h}} = \frac{\text{Gap}}{\text{Thickness}} \qquad (6.1)$$

Table 6.7 Soft/Hard ratio.

Specimen	Soft/Hard ratio
10 mm	1
15 mm	0.67
20 mm	0.5
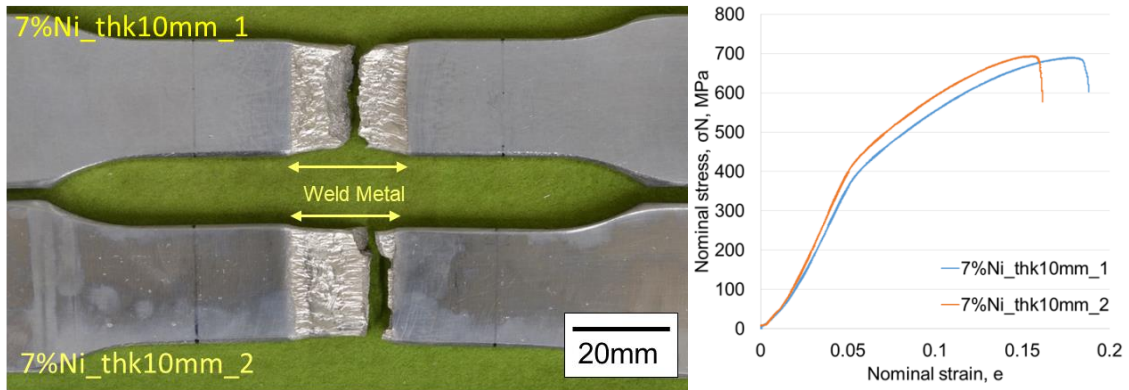
(a) 10-mm specimen.
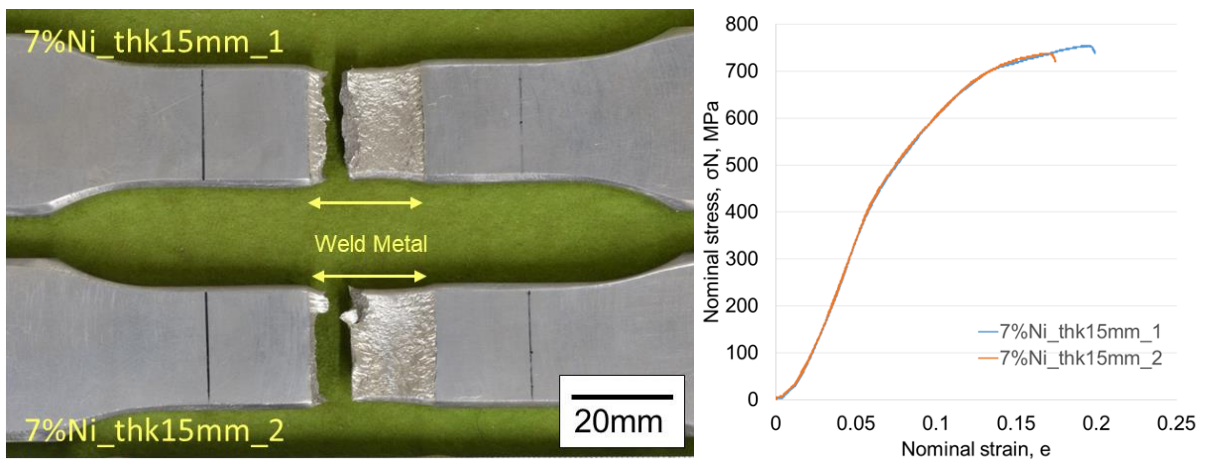
(b) 15-mm specimen.
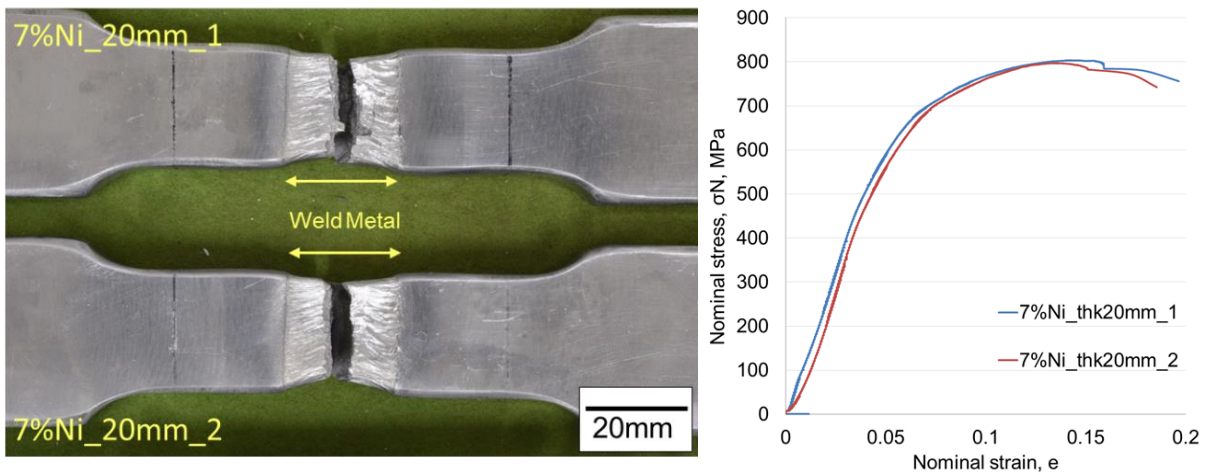
(b) 20-mm specimen.

Fig. 6.17 Photographs and stress-strain curves of tensile test results.
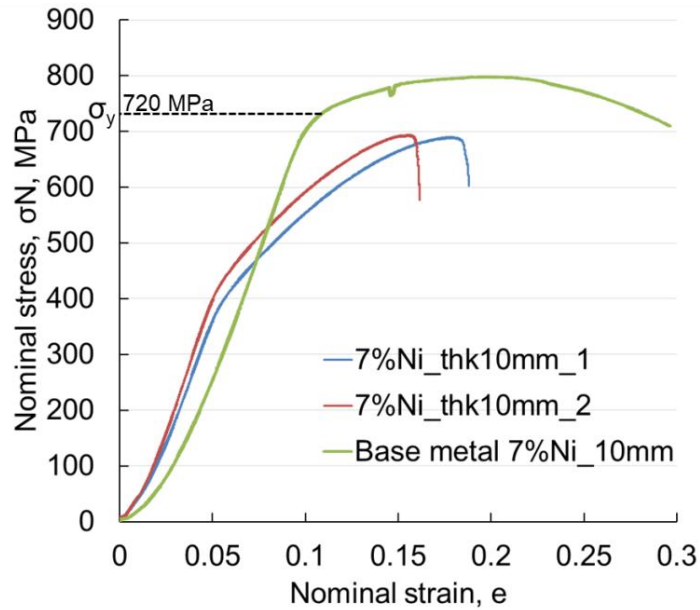
(a) 10-mm thickness.
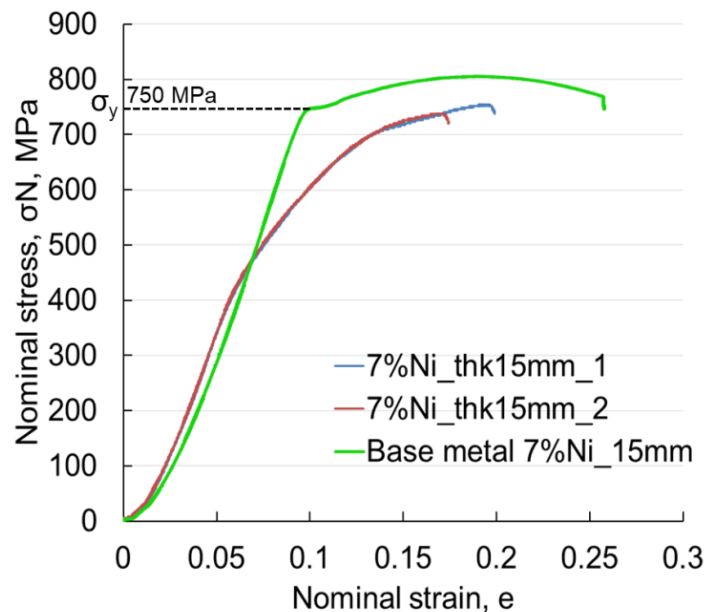
(a) 15-mm thickness.

Fig. 6.18 A relation between the tensile strength of base metal and welded joints.

The aforementioned photographs of 10 and 15 mm tensile specimens indicate that the plastic deformation only occurs in weld metal resulting in less elongation after rupture. Figure 6.18 (a), (b) shows the relationship between the tensile strength of base metal and welded joints in the specimen thickness of 10 and 15 mm in order. For 10-mm thickness, the yield strength of 720 MPa in base metal is higher than both the tensile test results of 690 MPa and 691 MPa in the welded joints, so only in

the weld metal did the plastic deformation appear. For 15-mm thickness, the base metal shows the yield strength of 750 MPa which is nearly the tensile strength of the welded joints, 756 and 737 MPa. As a result, the plastic deformation in the base metal of the welded joints could not be observed.

6.3.4 Charpy V-notch impact test of the welded joints

Figure 6.19 shows the test specimen and notch locations. The stand specimen size for Charpy impact test is 10mm x10mm x55mm according to JIS Z 2242 and the specimens are notched at weld metal, fusion line, fusion line+1 and fusion line+2. A test temperature is evaluated at -196^0C and the values shall exceed the minimum impact energy of 27 J specified in JIS 8285. In this test, the Charpy impact equipment has a heavy pendulum of 25.31kg and arm length of 0.7 m.

Figure 6.20 (a), (b) and (c) show the cutting plan and notch locations in each specimen, 10, 15 and 20 mm.
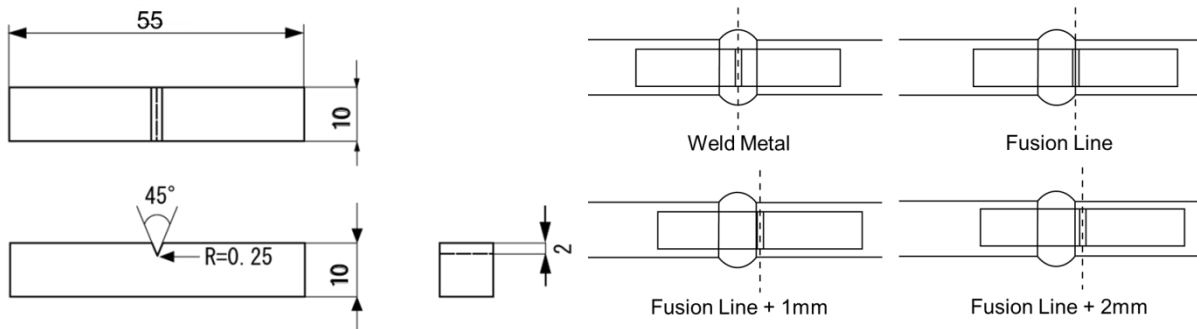
Fig. 6.19 Test specimen and notch locations.

(a) 10-mm specimen.

Fig. 6.20 Cutting plan.

Specimen Number

Notch Position

Specimen	Notch Position
108	FL
107	FL
106	FL+1
105	FL+1
104	FL
103	FL+2
102	FL+2
101	FL

Welding Direction

100

(b) 15 mm specimen.

Notch position

Welding Direction

42

FL

FL

FL

42

WM

WM

WM
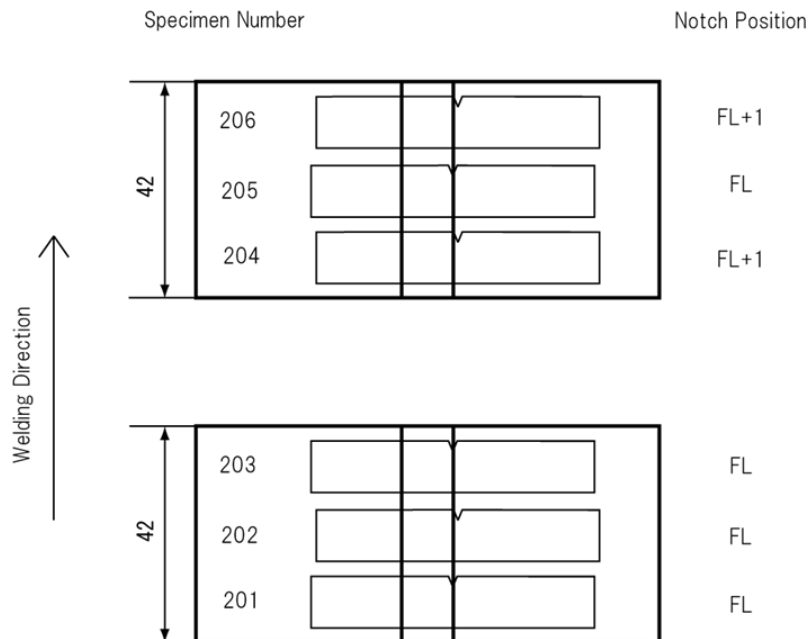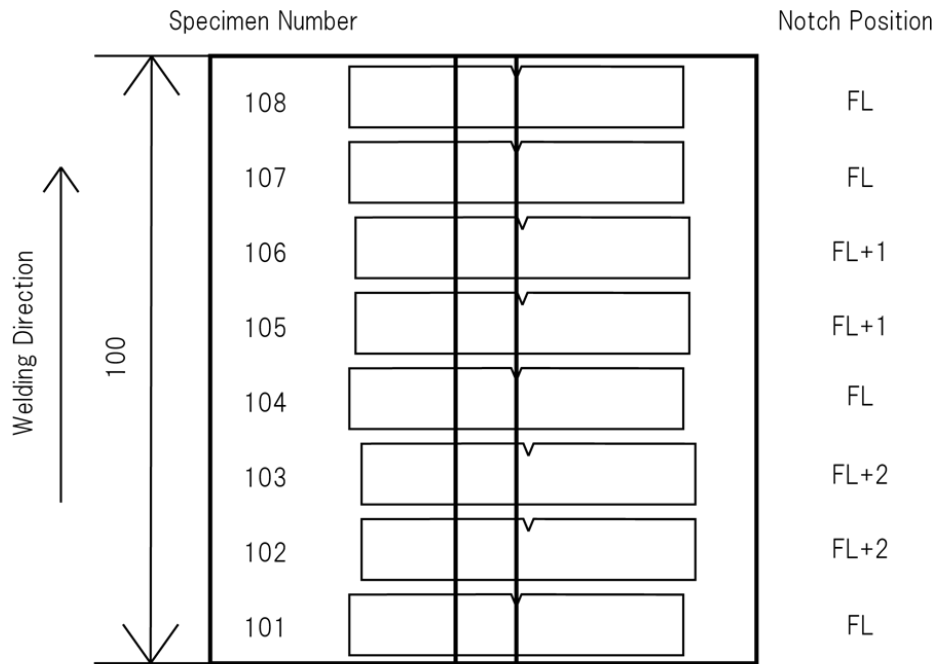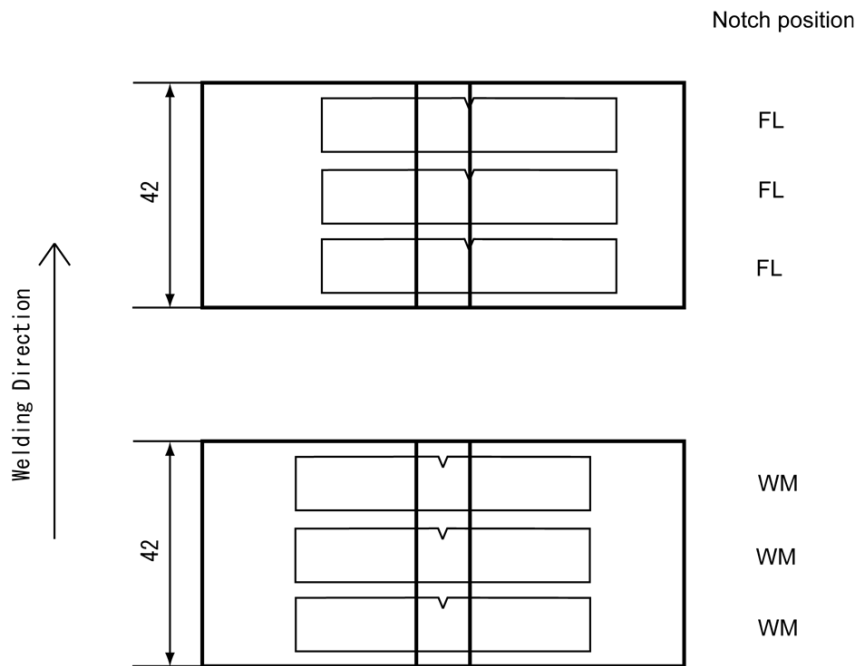
(C) 20 mm specimen.

Fig. 6.20 Cutting plan (continued).

Figure 6.21 shows the toughness values and fracture specimens of FL and FL+1 in the 10-mm-thick welded joint. The fusion line and fusion line+1 exhibit an extremely high absorbed energy when it is compared with the requirement of 27 J. The test pieces indicate a ductile fracture surface without imperfections. Therefore, this welded joint is satisfied for the toughness property.

Notch Position: Fusion Line	
No.F205: 138 J Crack Direction: Straight	No.F203: 147.7 J Crack Direction: Straight
No.F202: 200.6 J Crack Direction: Weld metal	No.F201: 170.4 J Crack Direction: Weld metal
Notch Position: Fusion Line+1	
No.F206: 176.9 J Crack Direction: Straight	No.F204: 217.5 J Crack Direction: Weld metal
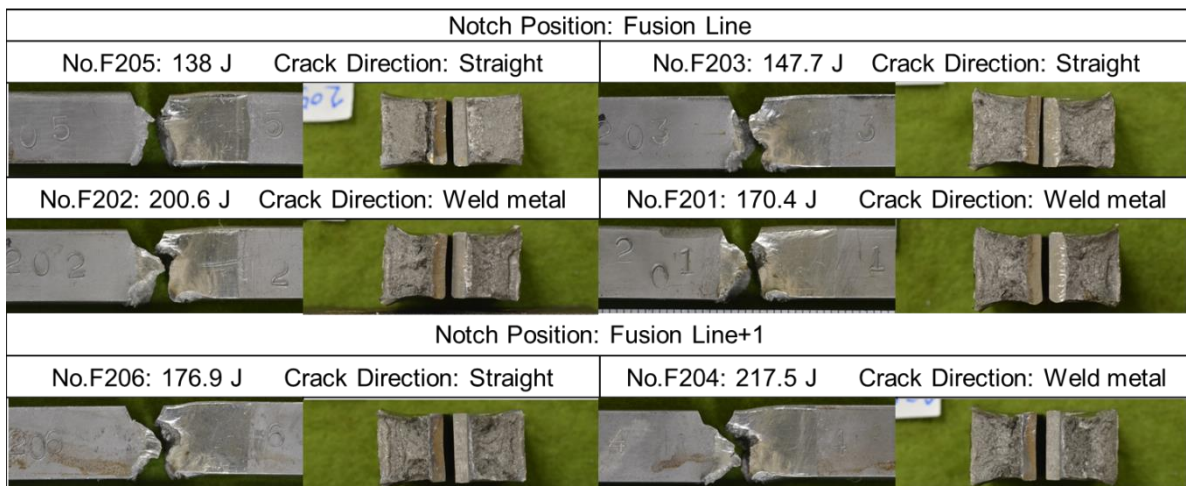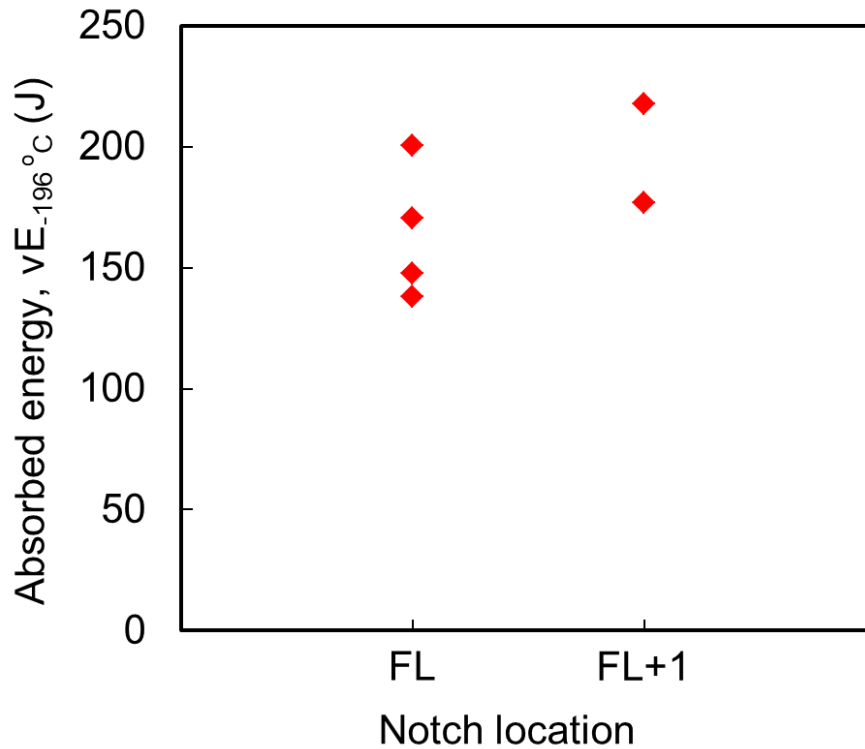
Fig. 6.21 Charpy impact test results of 10-mm-thick welded joint.

Figure 6.22 shows the Charpy impact test results and test pieces of FL, FL+1, and FL+2 in the 15-mm-thick welded joint. The very high toughness values are observed in all of the fusion line, fusion line+1 and fusion line+2 more than the specification of 27 J so it satisfies the standard requirement and specimens show a ductile fracture surface without imperfections.
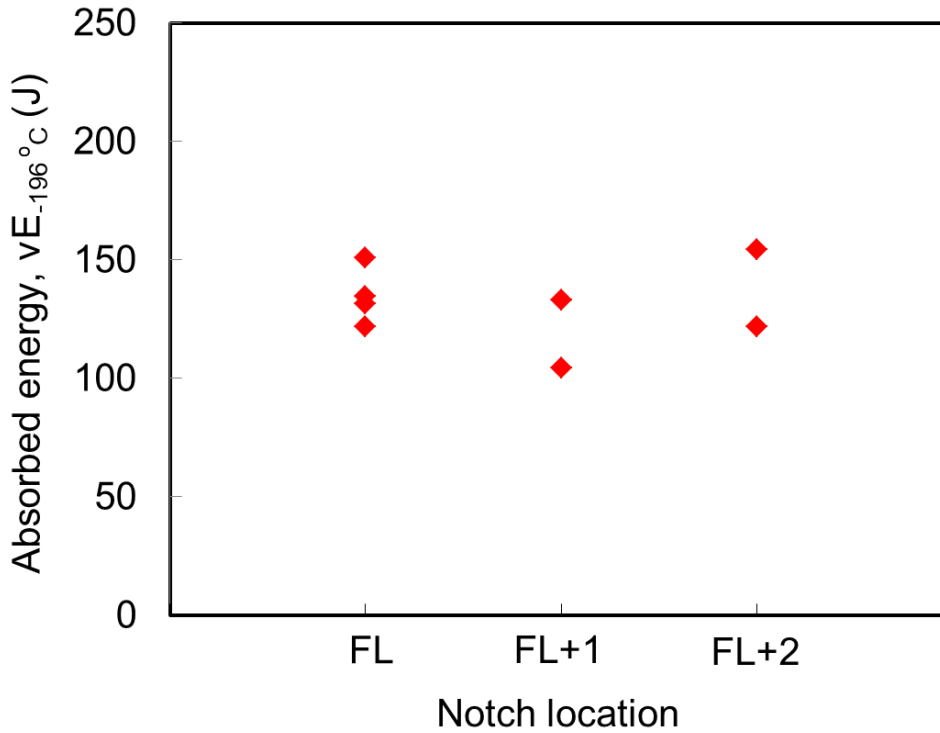
Notch Position: Fusion Line			
No.F108: 151 J Crack Direction: Straight		No.F107: 131.5 J Crack Direction: Straight	
No.F104: 134.7 J Crack Direction: Straight		No.F101: 121.8 J Crack Direction: Straight	
Notch Position: Fusion Line+1			
No.F106: 104.3 J Crack Direction: Straight		No.F105: 133.1 J Crack Direction: Straight	
Notch Position: Fusion Line+2			
No.F103: 121.8 J Crack Direction: Straight		No.F102: 154.2 J Crack Direction: Weld metal	

Fig. 6.22 Charpy impact test results of 15-mm-thick welded joint.

Figure 6.23 shows the Charpy impact test results and test pieces of WM, FL in the 20-mm-thick welded joint compared with the welded joint of GTAW in 32-mm thickness. The toughness values of weld metal and fusion line of the proposed process are high and much more than 27J. The welded joint satisfies the requirement, but the average toughness value has little lower in the HLW welded joint than in the GTAW welded joint.
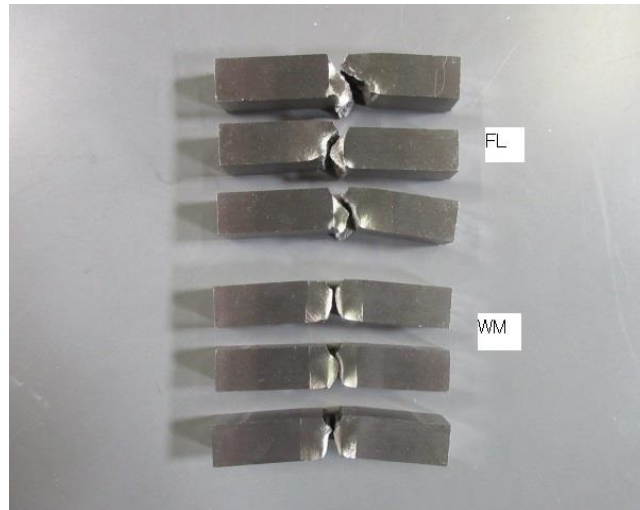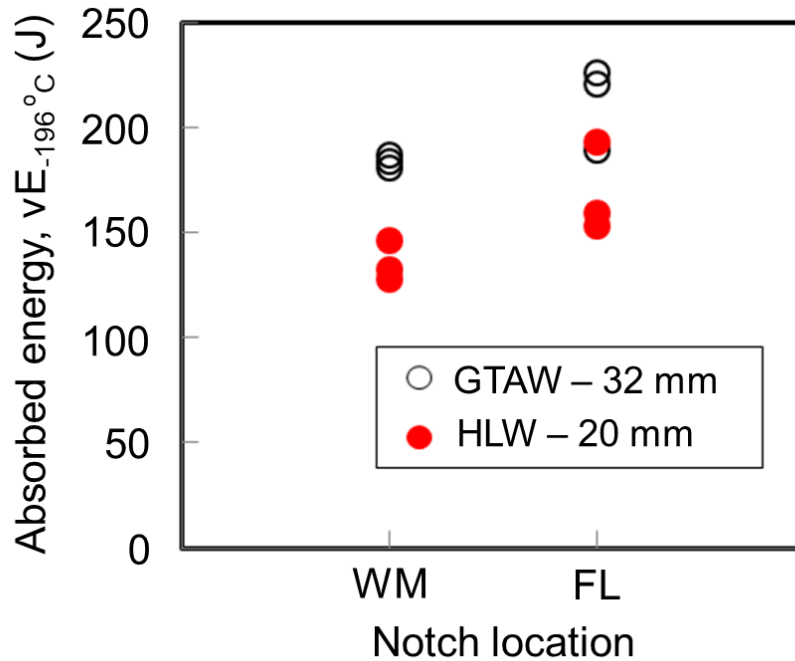
Fig. 6.23 Charpy impact test results of 20-mm-thick welded joint.

6.4 Summary

This chapter is to apply the single-pass vertical welding process using hot-wire laser for Ni steel plate. The proposed process is investigated to increase productivity and to reduce welding consumables compared with the conventional arc welding process. The summary results can be drawn as follows:

1) Ni steel plate range is from 6 to 50 mm usually used for LNG tanks in the field. This research applied the proposed process to 10, 15 and 20 mm thickness of 7% Ni steel plate in order to find the optimal welding conditions in different thicknesses. A controllable narrow and rectangular beam with a weaving system was used. Then the laser power and welding speed were optimized in each thickness to derive sufficient heat energy to continue the welding steadily, so the average heat input per thickness was about 4 (kJ/cm.mm).

2) The proposed process achieved a stable weld pool formation and steady hot-wire feeding during welding. However, some lack of fusion could be observed on the back side in the first period because the molten pool did not flow to an edge of the back side. Thereafter the complete penetration could be obtained and the cross-sections showed full penetration without any imperfections.

3) The joint properties of tensile test and Charpy impact test met the standard requirements. In case of the tensile strength, the breaking point was at the weld metal due to the softer material, and Soft/Hard ration also affected the tensile strength result. At the same gap width, the 10-mm specimen having higher Soft/Hard ration indicated the lesser tensile strength. In case of Charpy impact test, very high absorbed energy was found in all test pieces and the notch was located at WM, FL, FL+1, FL+2.

Chapter 7

Summary and future work

The aim of this research is to develop a novel welding process by using a diode laser and a hot-wire system. The hot-wire laser welding (HLW) was applied to a single-pass thick weld joint in a vertical direction so as to reduce the heat input and to replace the conventional welding process such as EGW of the large heat input process. The combination of a controllable rectangular beam as a heat source and hot-wire system was investigated. Adequate power distribution plays an important role to achieve a sound joint. The laser beam type and weaving system were optimized the power density distribution to reduce laser power at the most.

At first, the background statement, the objectives, and construction of the thesis were discussed and then recent researches on the vertical welding relevant to this study were summarized.

For the single-pass vertical welding, the principle ideas for optimizing power distribution are to keep the molten pool and melt the base metal. A controllable rectangular beam with a weaving system was studied. 2-mm and 4-mm beam widths with a 5-Hz exponential waveform having different power density were used. The 2-mm beam width showed high power density on the groove surfaces that could not keep heating on the middle of groove and some heat was lost by high reflecting laser on above the weld pool. In other words, the 4-mm beam width could keep the molten pool and melt the base metal better than the 2-mm beam width. In addition, the beam could concentrate more power on the beam edges by using a high-edged energy beam type made by a particular optic lens that could increase dilution and reduce lack of fusion on the groove edges. Consequently, the beam having the high-edged type and weaving system could optimal power distribution on the groove area.

Moreover, Oxygen additions in Ar shielding gas protecting the molten pool affected weld pool phenomena in a positive way that was able to increase dilution in the base metal. On the contrary, a high among of oxygen content could generate a thick oxide layer between the copper shoe and the weld bead. In the experiment, the optimal shielding gas provided better dilution by using 20%Oxygen-added Ar shielding gas than using pure Ar shielding gas.

The optimal welding conditions using a 6-kW rectangular beam were applied to a large size specimen and its thickness of 28.5 mm. The HLW joint with the long-welded specimen obtained low dilution and narrow heat affected zone as a result of the low heat input welding process and the heat input of the HLW joint had much lower than that of the EGW at the same thickness of base metal. Regarding the properties of the welded joint, the tensile strength met the requirement of the

specification and the V-notch Charpy impact test result of notch location at weld metal obtained high absorbed energy at -20^0C according to CTOD test results that exhibited the high resistance to brittle propagation at -10^0C. However, the fusion line showed the unstable absorbed energy because grain boundary ferrite could be observed in the fusion line.

As a limited diode power is 6 kW, twin diode lasers to increase a total of 12 kW were applied to a thicker plate of 50 mm. The large rectangular beam having high-edged energy was irradiated stably combined with either the narrow rectangular beam with the weaving system or the stable large rectangular beam. Based on adequate power laser and hot-wire system, the stable welding process could be observed during welding in three welding conditions. However, the cross-section of double stable laser beams showed very low dilution and narrow bead width and revealed the lack of fusion near the wire feeding side. Consequently, the stable beam with high-edged energy and the both weaving beams of 2-mm and 5-mm widths that achieved a sound joint could improve dilution on edges around plate surfaces and groove surfaces where the lack of fusion easily occurred.

Next, the novel single-pass vertical process was studied in Ni steel plate and EGW is not generally used for Ni steel as a result of large heat input that toughness property could deteriorate at a very low temperature of the used material and could generate severe distortion. Regarding Ni steel plate in the 6-50 mm range, it is usually used for LNG tanks in the field. This research applied the proposed process to 10, 15 and 20 mm of 7% Ni steel plate to find the optimal welding conditions in different thicknesses such as a laser spot shape, laser power, a welding speed, a joint configuration, etc. The HLW achieved a stable weld pool formation and steady hot-wire feeding during the whole welding period in all specimens. The complete penetration could be obtained in the steady state and the cross-sections showed full penetration without lack of fusion. The joint properties of tensile test and Charpy impact test met the standard requirements. In case of the tensile strength, the breaking point was located at the weld metal due to the softer material, and Soft/Hard ration also affected the tensile strength value. At the same gap width, the 10-mm specimen having higher Soft/Hard ration showed the low tensile strength value.

The heat input of the single-pass vertical weld joint between the convention arc process and HLW can be summarized in Fig. 7.1. SEGARC and VEGA processes used for EGW of the vertical joint are developed [41, 61, 91-92] to increase deposition rates and to reduce heat input. The heat input of HLW was calculated at the highest value using only laser power and welding speed with the efficiency factor of 100% because of the unknown absorption factor of the proposed process. Therefore, the actual heat input should be much lower than the calculation. The graph showed that the heat input of the developed EGW processes is lower than that of the conventional EGW, but it is higher than the heat input of HLW about 30% in 10-20 mm thickness. However, the heat input trend of the developed EGW exhibits vary high slope when the thickness is more than 30 mm. The HLW trend obtains low

slope and relatively straight line because the HLW could control the power density distribution precisely and efficiently for joining a heavy-thick joint.
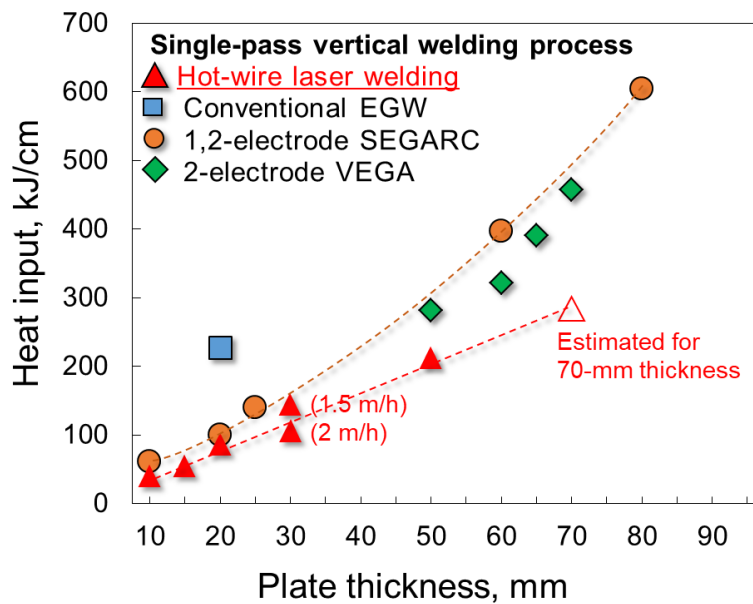
Fig. 7.1 Comparison of the heat input in a vertical joint between EGW and HLW.

For the shipbuilding industry, the novel vertical welding process achieved the optimal welding conditions such as power density distribution, the hot-wire system and so on. The 6-kW rectangular laser beam with the high-edged energy and weaving system could be applied to the large scale size in the thick steel plate, but its thickness was up to 28.5 mm. Consequently, the twin diode lasers with a total of 12 kW were investigated to a thicker plate of 50 mm and the optimal welding conditions were used in a small size jig. In future work, it is essential that the twin diode lasers should be developed to a large scale specimen like the field. A new jig has to be designed based on focal length and beam shape of both lasers, and thermal behaviors on the large-scale specimen would be realized during welding. Moreover, the weld joint property of Charpy impact test at fusion boundary should be studied in the chemical composition and solidification on fusion line to find more the cause of brittleness and be studied in changing groove from square groove to V groove.

For LNG tanks, since the steel plate is currently used in the high range thickness depending on tank capacity, the proposed process of the vertical joint was evaluated for the plate thicknesses of 10, 15 and 20 mm. In the future work, the thicker plate up to 50 mm should be studied and in case the plate is thinner than 10 mm, a narrower gap such as 8 mm should be studied so as to obtain high tensile strength.

Acknowledgements

Firstly, I would like to express my sincere gratitude to my advisor Prof. Motomichi Yamamoto for continuous support of my Ph.D study and my living in Japan, for his patience, motivation, and immense knowledge. His guidance helped me in all the time of research and writing of this thesis. I could not have imagined having a better advisor and mentor for my Ph.D study. Furthermore, I would like to thank Prof. Kenji Shinozaki. He gave me so much positive help and instructive discussion in my study, and I have learned so much from him, especially the great suggestion on research strategy and metallurgical perspective.

I would like to thank the rest of my thesis committee: Prof. Atsushi Sugata, Prof. Eiji Shintaku and Prof. Hino Ryuutarou for their insightful comments and encouragement, but also for the hard question which incented me to widen my research from various perspectives.

I would like to thank the past members of my research group: Mr. Masuda Kouhei, Mr. Shota Sekiguchi and Mr. Kodama Kazuki. I would also like to thank all the past and present members of the Materials Joining Science and Engineering Laboratory, in the Department of Mechanical Science and Engineering, Hiroshima University, for their enthusiastic help to both my life and study.

I would like thank my parents for their support and encouragement from my youth to my time as a doctoral student. Their teaching is gratefully appreciated and has been invaluable in my life.

Reference

1) 山口欣弥，北田博重，矢島浩，廣田一博，白木原浩：『超大型コンテナ船の開発 −新しい高強度極厚鋼板の実用−』日本船舶海洋工学会誌 第 3 号 (2005)，p.70-76.

2) 岡野重雄，大番屋嘉一，阿部研吾，細井宏一：『厚板需要業界の技術動向と当社の対応状況』神戸製鋼技報 Vol.58 No.1 (2008)，p.2-7.

3) 木治昇，豊田昌信：『船舶 −溶接技術による安全・環境性能向上−』溶接学会誌 No.3 (2012)，p.21-24.

4) 船津裕二：『船舶(材料編)』溶接学会誌 No.4 (2012)，p.41-47.

5) 中島善之，岡田哲男：『船舶(日本造船工業界)』溶接学会誌 No.1 (2013)，p.24-28.

6) 白幡浩幸，皆川昌紀，井上健裕，大谷潤，船津裕二：『超大型コンテナ船厚手高靭性 YP47 鋼の開発』まてりあ Vol.51 No.2 (2012)，p.76-78.

7) 一宮克行，角博幸，平井龍至：『「JFE EWEL®」技術を適用した大入熱溶接仕様 YP460 級 鋼板』JFE 技報 No. 18 (2007)，p.13-17.

8) 廣田一博，中川隆，武田信玄，橘吉美，多田益男：『世界初の船体用降伏応力 47kgf/mm^{2}級 高張力鋼板の開発と実船適用』三菱重工技報 Vol.44 No.3 (2007)，p.28-32.

9) 金子雅人，泉学，吉川直宏，阿部研吾：『超大型コンテナ船向け大入熱溶接用 YP460MPa 級 厚肉鋼板の開発』神戸製鋼技報 Vol.58 No.1 (2008), p.39-41.

10) 日本海事協会：『船舶の排ガス規制について』, 2015.

11) 日本海事協会：『低硫黄燃料油に関する規制と問題点，その対策について』, 2018.

12) 森俊美：『船舶における LNG 燃料利用』日本マリンエンジニアリング学会誌 第 47 巻　第 6 号(2012), p.19-23.

13) 永田良典，田ノ上聖，木田隆之，川合崇：『LNG 燃料船用 IHI-SPB タンク』IHI 技報 Vol.52 No.3 (2012), p.36-41.

14) T. Masanobu, K. Hiroki, W. Kazuo ： "Intrinsically Safe Cryogenic Cargo Containment System of IHI-SPB LNG Tank", IHI Engineering Review, Vol.47 No.2 (2015), p.27-33.

15) T. Akira, K. Takayuki, K. Takashi ： "IHI-SPB Tank for LNG-Fueled Ship", IHI Engineering Review, Vol.47 No.2 (2015), p.17-21.

16) 猪瀬幸太郎：『LNG タンクの構造と溶接』WE-COM マガジン　第 16 号 (2015).

17) 加賀谷孝之，古谷仁志，加茂孝浩ら：『新 LNG タンク用鋼板』新日鉄住金技報 第 400 号　(2014), p.38-44.

18) JIS3332:1999：『9%ニッケル鋼用ティグ溶加棒及びソリッドワイヤ』.

19) Electroslag and Electrogas Welding, AWS welding handbook, Vol.2 No.7 (1978), p.226-260.

20) H.C. Campbell : "Eletroslag, Electrogas and Related Welding Processes", WRC Bull., Vol.154 (1970).

21) Electroslag Electrogas Tips & Techniques, Bulletin of electrotherm corp., 1973.

22) B.Paton: Eletroslag welding, AWS, 1962.

23) 溶接学会誌 第 66 巻 第 4 号 (1997)，p.54-58.

24) K. Hirota, T. Nakagawa, S. Takeda, Y. Hashi, M. Tada : "World's development and application of HTSS (high tensile strength steel) with yield stress of 47 kgf/mm^2 to actual ship hull structure", Mitsubishi Heavy Industries, Ltd. Technical Review Vol.44 No.30 (2007), p.1-5.

25) Guidelines on the Application of YP47 Steel for Hull Structures of Large Container Carriers, ClassNK TECHNICAL BULLETIN, 2008, p.65-68.

26) O. Doerk, J Rörup : "Development of Toughness and Quality Requirement for YP47 Steel Weld Based on Fracture Mechanics", Proceedings of the Nineteenth International Offshore and Polar Engineering Conference, Osaka, Japan, 2009, p.386.

27) Y. Funatsu, J. Otani, K. Hirota, T. Matsumoto, H. Yajima : "Development of higher Toughness YP47 (460N/mm^2) Class Steel Plate for Large Container Ships", Proceedings of the Twentieth International Offshore and Polar Engineering Conference, Beijing, China, 2010, p.102.

28) K.K. Um, S.H. Kim, K.B. Kang, Y.H. Park, O. Kwon : "High Performance Steel Plates for Shipbuilding Applications", Proceedings of the Eigthteenth International Offshore and Polar Engineering Conference, Vancouver, BC, Canada, 2008, p.277.

29) W.G. Kim, K.K. Um, Y.H. An, C.S Lee : "Mechanical Properties of YS 460MPa TMCP Steel Plate for Large Container Ships" Proceedings of the Nineteenth International Offshore and Polar Engineering Conference, Osaka, Japan, 2009, p.381.

30) H. Sekine : 86th/87th Nishiyama Memorial Seminar, The Iron and Steel Institute of Japan, 1982, p.123.

31) H. Morikawa, T. Hasegawa : "Proc. Int. Symp. On Accelerated Cooling of Steel", TMS,1986.

32) K. Omata, H. Yoshimura, S. Yamamoto : "Leading High Performance Steel Plates with Advance Manufacturing Technologies", NKK technical review No.88 (2003), p.73-80.

33) Y. Onoe, M. Umeno, O. Mantani, Y. Sogo, K. Sakai, T. Iwanaga, H. Morikawa. Seitetsu Kenkyu, 309, 18 (1982).

34) A. Yoshie : "Visual Engineering Book on Iron and Steel", Sheets&Plates Vol.3, Nippon Steel, Nippon Jitsugyo Publishing, 2009, p.66.

35) A. Kojima, A. Kiyose, R. Uemori, M. Minagawa, M. Hoshino, T. Nakashima, et al : "Super High HAZ Toughness technology with Fine Microstructure Imparted by Fine Particles", Nippon steel technical report, No.90(2004), p.2-6.

36) G. Shigesato : "Progress of High Performance Steel Plates with Excellent HAZ Toughness", Nippon steel & Sumitomo metal technical report, No.119(2018), p.22-25.

37) S. Shinichi, I. Katsuyuki, A. Toshikasu : "High Tensile Strength Steel Plates with Excellent HAZ Toughness for Shipbuilding", JFE technical report, No.5(2005), p.24-29.

38) T. Kato, S. Sato, H. Ohta, T. Shiwaku : "Effects of Ca Addition on Formation Behavior of TiN Particles and HAZ Toughness in Large-Heat-Input Welding", KOBELCO technology review, No.30(2011), p.76-79.

39) N. Koichi, H. Kazukuni, E. Taiki : "Development of Shipbuilding Steel Plate with Superior Low Temperature Toughness for Large Heat Input Welding", JFE technical report, No.20(2015), p.8-13.

40) C. M. Kim, J. B. Lee, W. Y. Choo : "Characteristics of Single Pass Welds in 50kJ/mm of Heavy Thickness Shipbuilding Steel", Proceedings of the Thirteenth International Offshore and Polar Engineering Conference, Honolulu, Hawaii, USA, 2003, p.90-96.

41) M. Minagawa, K. Ishida, Y. Funatsu, S. Imai : "390 MPa Yield Strength Steel Plate for Large Heat-input Welding for Large Container Ships", Nippon steel technical report, No.90(2004), p.7-10.

42) I. Katsuyuki, S. Hiroyuki, H. Tatsushi : "460MPa-Yield-Strength-Class Steel Plate with JFE EWEL® Technology for Large-Heat-Input Welding", JFE technical report, No.11(2008), p.7-12.

43) W. Sun, G. Wang, J. Zhang, D. Xia, H. Sun : "Microstructure Characterization of High-heat-input Welding Joint of HSLA Steel Plate for Oil Storage Construction", J.Mater.Sci.Technol., Vol.25 No.6(2009), p.857-869.

44) O. Doerk, W. Fricke, H. V. Selle : "Validation of Different Fatigue Assessment Approaches for Thick Plate Structures Made of High Tensile Strength Steel YP47", Proceedings of the Twenty-second International Offshore and Polar Engineering Conference, Rhodes, Greece, 2012, p.52.

45) H. Kazukuni, H. Tsunehisa, E. Taika : "Development of YP460 N/mm^2 Class Heavy Thick Plate with Excellent Brittle Crack Arrestability for Mega Container Carriers", JFE technical report, No.20(2015), p.14-19.

46) ASME BPVC.II.A, SA-553, Specification for pressure vessel plates, alloy steel, quenched and tempered 7, 8 and 9% nickel, USA, 2017, p.951-954.

47) K. Hickmann, A. Kern, U. Schriever, and J. Stumfe : "Production and properties of high strength nickel alloy steel plates for low temperature applications", Germany, 2005.

48) J. I. Jang, J. B. Ju, B. W. Lee, D. Kwon, W. S. Kim : "Effects of microstructural change on fracture characteristics in coarse-grained heat-affected zones of QLT-processed 9% Ni steel", Mat.Sci. and Eng., A340(2003), p.68-79.

49) N. Saitoh, R. Yamaba, H. Muraoka, O. Saeki : "Development of Heavy 9% Nickel Steel Plates with Superior Low-Temperature Toughness for LNG Storage Tanks", Nippon steel technical report, No.58(1993), p.9-16.

50) M. Hoshino, N. Saitoh, H. Muraoka, O. Saeki : "Development of Super-9%Ni Steel Plates with Superior Low-Temperature Toughness for LNG Storage Tanks", Nippon steel technical report, No.90(2004), p.20-24.

51) Y. K. Yoon, J. H. Kim, K. T. Shim : "Mechanical characteristics of 9% Ni steel welded joint for LNG Storage Tank at Cryogenic", AMDP2011 International Journal of Modern Physics, Vol.6(2012), p.355-360.

52) S. Hany, B. Duponchel, C. Poupin, A. A. Kais, D. Dewael, J. B. Vogt, et al : "Microstructural and Mechanical Properties of 9%Ni Steels Used for the Construction of LNG storage tanks", Advance Material Research, Vol.936(2014), p. 1953-1957.

53) http://www.ivt.ntnu.no/ept/fag/tep4215/innhold/LNG%20Conferences/2007/fscommand/PO_20_Toussaint_s.pdf, 2007(cited 2019 June 21).

54) P. P. Poletskov, O. A. Nikitenko, D. M. Chukin, M. S. Gushchina, S. A. Fedoseev : " On Microstructure Formation Features of 9% Nickel Cold-Resistant Steel and Its Properties Brought about by Different Heating Treatment Procedures", Journal of Chemical Technology and Metallurgy, Vol.53 No.5(2018), p. 967-976.

55) https://www.nipponsteel.com/en/news/20140619_100.html, 2014 (cited 2019 June 21).

56) K. Naoshige, T. Masanori, Y. Maki, K. David, H. Hitoshi, S. Naokazu, et al : "Development of 7% Ni-TMCP Steel Plate for LNG Storage tanks", J.JWS, 28-1(2010), p.130-140.

57) H. Nishigami : "Development of 7%Ni-TMCP Steel plate for LNG storage tanks", International Gas Union Research Conference, 2011.

58) H. Nishigami, M. Kusagawa, M. Yamashita, T. Kawabata, T. Kamo, K. Onishi, et al "Development and realization of large scale LNG storage tank applying 7% Nickel plate", World Gas Conference, Kuala Lumpur, Malaysia, 2012, p.1-18.

59) T. Kagaya, H. Furuya, T. Kamo, Y. Takahashi, H. Wakamatsu, T. Nagao, K. Ohnishi : "New Steel Plate for LNG Storage Tank", Nippon Steel & Sumitomo metal technical report, No.110(2015), p.36-42.

60) ASME BPVC.II.A, SA-841 Grade G, Specification for steel plates for pressure vessels, produced by thermal-mechanical control process (TMCP), USA, 2017, p.1417-1426.

61) K. Sasaki, K. Suda, R. I. Motomatsu, Y. Hashiba, S. Ohkita, S. Imai : "Development of Two-electrode Electrogas Arc Welding Process", Nippon steel technical report, No.90(2014), p.67-74.

62) Y. Hashiba, K. Kojima, T. Kasuya, T. Kumagai : "Development of Welding Consumables and Welding Process for Newly Developed Steel Plates", Nippon steel technical report, No.110(2015), p.90-96.

63) J. Y. Park, J. M. Lee, M. H. Kim : "An investigation of the Mechanical Properties of a Weldment of 7%Nickel Alloy Steels", Metals, No.2(285), p.1-10.

64) K. Imamura, S. Nagumo, S. Watanabe, S. Tomidokoro, A. Tejima and N. Katayama : "Development of Remote Controlled Automated TIG Welding Equipment for LNG Storage Tank", IHI Engineering Review, Vol.29 No.4(1996), p.133-138.

65) K. Kobayashi, M. Yuki, A. Tejima, Y. Nishimura : "Development of High Efficiency TIG Welding Method (SEDAR-TIG)", IHI Engineering Review, Vol.35 No.4(2002), p.137-142.

66) S. Rie, K. Kazuyuki, I. Tooru, N. Yoshihito, M. Yutaka : "Development of Vertical Submerged Arc Welding Method for Aboveground LNG Storage Tank Construction", IHI Engineering Review, Vol. 43 No.2(2010), p.55-62.

67) S. Tsubota, T. Ishide, M. Nayama, Y. Shimokusu, S. Fukumoto : "Development of 10kW class YAG Laser Welding Technology", ICALEO 2000, p.219-229.

68) S. Katayama, A. Yohei, M. Mizutani, Y. Kawahito : "Development of Deep Penetration Welding Technology with High Brightness Laser under Vacuum", Physics Procedia, Vol.12(2011), p.75-80.

69) J. Frostevarg : "Factors affecting weld root morphology in laser keyhole welding", Optics and Lasers in Engineering, Vol.11(2018), p.89-98.

70) Y. Qi, G. Chen : "Root defects in full penetration laser welding of thick plates using steady electromagnetic force", Journal of Materials Processing Tech., Vol.260(2018), p.97-103.

71) M. Karhu, V. Kujanpaa, M. Pesari, B. Ievesy : "Comparison of laser welding methods in position welding edge joint of austenitic stainless steel", NOLAMP 14, Gothenburg, 2013, p.46-58.

72) B. Chang, Z. Yuan, H. Pu, H. Li, H. Cheng, D. Du, J. Shan : "A Comparative Study on the Laser Welding of Ti6Al4V Alloy Sheet in Flat and Horizontal Positions", Appl. Sci., Vol.7 No.376(2017), p.1-12.

73) B. Chang, Z. Yuan, H. Pu, H. Li, H. Cheng, D. Du, J. Shan : "Study of Gravity Effects on Titanium Laser Welding in the Vertical Position", Materials, Vol.10 No.1031(2017), p.1-12.

74) R. Phaonaim : "Evaluation and prediction method for solidification cracking during hot-wire laser welding with a narrow gap joint and GMAW process using computational simulation", Doctoral dissertation, Hiroshima University, 2014.

75) K. Shinozaki, M. Yamamoto, Y. Nagamitsu, T. Uchida, K. Mitsuhata, T. Nagashima, et al : "Melting Phenomena during Ultra-High-Speed GTA Welding Method using Pules-heated Hot-wire", Quarterly J. JWS, Vol.27 No.2(2009), p.22-26.

76) S. Ueguri, Y. Tabata, T. Shimizu, T. Mizuno : "A Study on Control of Deposition Rate in Hot-wire TIG welding", Quarterly J. JWS, Vol.4(1986), p.24-30.

77) K. Hori, H. Watanabe, T. Myoga, K. Kusano : "Development of hot wire TIG welding methods using pulsed current to heat filler wire", Welding International, Vol.18 No.6(2004), p.456-468.

78) M. Yamamoto, K. Shinozaki, K. Kadoi, D. Fujita, T. Inoue, M. Fukahori, et al : "Development of Hot-wire Laser Welding Method for Lap Joint of Steel Sheet with Wide Gap", Quarterly J. JWS, Vol.29 No.3(2011), p.58-61.

79) K. Kadoi, K. Shinozaki, M. Yamamoto, K. Owaki, K. Inose, D. Takayanagi : "Development of High-efficiency/High-quality Hot-wire Laser Fillet Welding Process", Quarterly J. JWS, Vol.29 No.3 p.62-65.

80) D. Okita, T. Kado, M. Yamamoto, K. Shinozaki, K. Kadoi : "Weld Defect Prevention for Fillet Welded Joints on Steel Plates Coated with Shop Primer using Hot-wire Laser Welding", Quarterly J. JWS, Vol.33 No.2, p.98-101.

81) R. Phaoniam, K. Shinozaki, M. Yamamoto, K. Kadoi, S. Tsuchiya, A. Nishijima : "Development of a highly efficient hot-wire laser hybrid process for narrow-gap welding-welding phenomena and their adequate conditions", Weld World, Vol.57(2013), p.607-613.

82) R. Phaoniam, M. Yamamoto, K. Shinozaki, M. Yamamoto, K, Kadoi : "Development of a Heat Source Model for Narrow-gap Hot-wire Laser Welding", Quarterly J. JWS, Vol.31 No.4(2013), p.82-85.

83) E. Warinsiriruk, K. Hashida, M. Yamamoto, K. Shinozaki, K. Kadoi, T. Tanino, et al. Welding phenomena during vertical welding on thick steel plate using hot-wire laser welding method, Quarterly J. JWS, Vol.33 No.2(2015), p. 143-147.

84) E. Warinsiriruk, K. Hashida, M. Yamamoto, K. Shinozaki, H. Yajima, T. Tanino, et al. Oblique laser irradiation technique for vertical welding of thick steel plates employing hot-wire laser welding , Quarterly J. JWS, Vol.33 No.4(2015), p. 326-331.

85) E. Warinsiriluk : "Development of vertical welding technology on thick steel plate using hot-wire laser welding method", Doctoral dissertation, Hiroshima University, 2015.

86) M. Kouhei : "Development of vertical welding process for thick steel plate using hot-wire laser welding method", Master thesis, Hiroshima University, 2016.

87) M. I. Ondoien, S. Liu, D. L. Olson : "Shielding gas oxygen equivalent in weld metal microstructure optimization", Welding research supplement, 1996, p.216-224.

88) T. Wegrzyn : "Proposal of welding methods in terms of the amount of oxygen", Archives of Materials Science and Engineering, Vol.47, No.1(2011), p.57-61.

89) S. Lu, H. Fuji, H. Sugiyama, M. Tanaka, K. Nogi : "Effects of oxygen additions to argon shielding gas on GTA weld shape" Vol.43(2003), p.1590-1595.

90) J. S. Seo, C. Lee, H. J. Kim : "Influence of Oxygen Content on Microstructure and Inclusion Characteristics of Bainitic Weld Metals", Vol.53(2013), p.279-285.

91) Kobelco welding today, Vol.11, No.2(2008), p.7.

92) Kobelco welding today, Vol.14, No.1(2011), p.5-6.

Published or Submitted Papers in Regard to This Thesis

1. **S. Charunetratsamee**, M. Yamamoto, K. Shinozaki, H. Yajima, N. Oda, H. Aono : "Development of Vertical Welding Process for Heavy-thick Steel Plate using Hot-wire Laser Welding", Proceedings of The 8th Asia-Pacific IIW International Congress, Thailand, 2019, p.45-48. (Chapter 5)

2. **S. Charunetratsamee**, E. Warinsiriruk, K. Shinozaki, M. Yamamoto : "Optimization of Laser-Irradiating Conditions for Vertical Welding on Thick Steel Plate using Hot-Wire Laser-Welding Method", Quarterly J. JWS, Vol. 37(4), 2019, p.187-192. (Chapter 3)

3. **S. Charunetratsamee**, E. Warinsiriruk, K. Shinozaki, M. Yamamoto : "Melting by Reflected Laser Beam during Vertical Welding via Hot-Wire Laser-Welding Method", Quaterly J. JWS, 2019. (Accepted) (Chapter 3)

Presentations

1. **S. Charunetratsamee**, M. Kohei, M. Yamamoto, K. Shinozaki, H. Yajima, T. Fukui, S. Nakayama, K. Kamita, S. Kodama, H. Aono : "Optimization of Vertical Welding Conditions for Thick Steel Plate using Hot-wire Laser Welding Method", National Conference of JWS, Japan, Vol.101(2017-9), p.424-425. (Chapter 3)

2. **S. Charunetratsamee**, S. Sekiguchi, M. Yamamoto, K. Shinozaki, H. Yajima, Y. Funatsu, S. Nakayama, K. Kamita, N. Oda, H. Aono : "Properties of Single-pass Vertical Welded Joint of Thick Steel Plate using Hot-wire Laser Welding", National Conference of JWS, Japan, Vol.103(2018-9), p.380-381. (Chapter 4)

3. **S. Charunetratsamee**, M. Yamamoto, K. Shinozaki, H. Yajima, N. Oda, H. Aono : "Development of Single-pass Vertical Welding on Heavy-thick Steel Plate using Hot-wire Laser Welding", The 8th International Congress on Laser Advanced Materials Processing, Japan, 2019, p.128. (Chapter 5)